

**Calorimetric and Dielectric Studies of Self-assembled Bio-
molecules in an Aqueous Environment**

by

Klaida Kashuri

A Dissertation

Submitted to the Faculty

of the

WORCESTER POLYTECHNIC INSTITUTE

In partial fulfillment of the requirements for the

Degree of Doctor of Philosophy

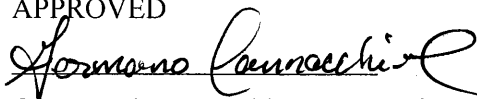
in

Physics


by

November 26, 2013

APPROVED



Germano S. Iannacchione, Head of Physics, WPI, PhD Advisor.



Izabela Stroe, Assistant Professor of Physics, WPI.



Georgi Georgiev, Professor, Department of Natural Sciences, Assumption College.

Abstract

Self-assembly and the induced orientation of microscopic biological systems is of great scientific interest, because it holds the promise of many pharmaceutical applications. This dissertation presents experimental studies done on proteins, short DNA fragments, and cholesterol structures self-assembled in an aqueous environment. The goal is to probe the thermo-physical properties of these systems, their phases and phase transitions, in order to better understand the principles behind their unique assemblies and function. It is accepted that in all these systems the solvent water plays an important role on the assembly folding, orientation, and activity of biopolymers. However, the abundance of water in typical samples presents many experimental challenges. It is indeed the case that changes in the properties of hydration in watery environments are responsible for the dynamics of protein and DNA biomolecules. We have explored in more detail the thermodynamics, the structural properties, and the dynamics near structural transitions of biomolecules in their native aqueous environment.

Calorimetry (AC and MDSC) studies as well as low-frequency (0.001 to 100 kHz) dielectric measurements have been performed on hen egg white lysozyme and short DNA hairpins dissolved in an aqueous buffer solution as a function of temperature, protein concentration and frequency. From the heat capacity profile of protein + buffer samples, the protein denaturing is found to be followed by gelation. Liquid crystal-like phase behavior of short DNA hairpins in solution was also observed. All calorimetry results are supported by dielectric spectroscopy results for both systems at room temperature, revealing low-frequency dynamic modes associated with large-scale self-assembled order.

Optical and calorimetric techniques are employed to study temperature and concentration dependence of three self-assembled microstructure types formed in Chemically Defined Lipid Concentrate (CDLC), considered a model system for cholesterol crystallization in gallbladder bile. Calorimetric studies (differential scanning and modulation) reveal thermal signatures that correspond to the optically observed structural evolution, which occurs throughout a large region of metastable chemical coexistence. These results suggest that a pseudo-phase diagram for the microstructures formed in CDLC may be developed to explain the observed behavior of the system.

TABLE OF CONTENTS

Chapter	Page
1. INTRODUCTION	1
1.1 Thermodynamics.....	1
1.2 Bio-thermodynamics and transitions of biological molecules.....	6
1.3 Using dielectric spectroscopy on biopolymers	7
1.4 The Effect of solvent water on bio-assemblies	12
1.5 Overview of proteins.....	15
1.5.1 The structural basis of protein function	15
1.5.2 Forces determining the protein structure	20
1.6 DNA structure and conformation.....	24
1.7 Cholesterol structures in CDLC (Chemically Defined Lipid Concentrate).....	27
1.8 References.....	29
2. EXPERIMENTAL METHODS	31
2.1 Review of AC-calorimetry.....	31
2.1.1 Introduction.....	31
2.1.2 Theory of operation	32
2.1.3 Calorimeter design and electronic circuitry	37
2.2 Modulated differential scanning calorimetry.....	42
2.3 Dielectric spectrometer design and operation.....	44

2.4	References.....	46
3.	LC-PHASE ORDERING OF SHORT DNA (sDNA) FRAGMENTS IN AQUEOUS SOLUTIONS	48
	Abstract	48
3.1	Introduction	49
3.2	Experimental	55
3.2.1	Materials and sample preparation	55
3.2.2	AC-Calorimetry	58
3.2.3	Modulated differential scanning calorimetry.....	59
3.2.4	AC-Capacitive dielectric spectrometry.....	60
3.3	Results	61
3.4	Discussion and conclusions	71
3.5	References.....	75
4.	UNDERSTANDING THE PROTEIN CONFORMATION IN AQUEOUS SOLUTIONS BY STUDYING LOW FREQUENCY DIELECTRIC SPEC- TRA AND THERMAL UNFOLDING OF LYSOZYME	77
	Abstract	77
4.1	Introduction	78
4.2	Experimental	82
4.2.1	Materials and sample preparation.....	82
4.2.2	Results.....	84
4.3	Discussion and conclusions	94

4.4 References.....	97
5. PSEUDO-PHASE DIAGRAM OF MICROSTRUCTURES IN CHEMICALLY-DEFINED LIPID CONCENTRATES BY OPTICAL MICROSCOPY AND HIGH-RESOLUTION CALORIMETRY.....	99
Abstract.....	99
5.1 Introduction	100
5.2 Experimental	105
5.2.1 Sample preparation and optical microscopy.....	105
5.2.2 Calorimetry	106
5.3 Results.....	108
5.3.1 Optical microscopy	108
5.3.2 Calorimetry	111
5.4 Discussion and conclusion	116
5.5 References.....	122
6. CONCLUSIONS.....	126
7. APPENDIX.....	129
Publications.....	129
Presentations/Abstracts published... ..	130

LIST OF FIGURES

Figure	Page
1.1 Mechanisms of electric polarization.	8
1.2 The effect of polarization in the dielectric media.	9
1.3 Frequency dependence of $\epsilon'(\omega)$ and $\epsilon''(\omega)$ for a relaxation process.	10
1.4 The hydration shell of myoglobin (Mb). Diagram of myoglobin (blue surface) with water molecules (CPK model). The water molecules here form a shell $\approx 5 \text{ \AA}$ thick around the protein.	14
1.5 Amino acid structure.	16
1.6 Primary Structure (peptide chain)	16
1.7 The repeated dihedral $\{\phi, \psi\}$ angles and the peptide planes	17
1.8 Protein Secondary structure: α -helix and the hydrogen bonds (black dotted lines).	18
1.9 Protein Secondary structure: β -sheet and the hydrogen bonds (red dotted lines).	19
1.10 The van der Waals potential energy function. Both, value of energy at	

the minimum E^* and the optimal separation of atoms r^* (which is roughly equal to the sum of Van der Waals radii of the atoms) depend on chemical type of these atoms.....	23
1.11 A nucleotide, the repeat unit of DNA	25
1.12 Base-pairing in DNA. Purine bases pair with pyrimidine bases, pink-dotted lines indicate hydrogen bonds.....	26
1.13 Typical helical structures in CDLC system. (a) Low pitch helical ribbon with a pitch angle $\psi = 11 \pm 2^\circ$. (b) High pitch helical ribbons with a pitch angle $\psi = 54 \pm 2^\circ$. (c) Intermediate pitch helical ribbons with a pitch angle $\psi = 40.8 \pm 3.8^\circ$	28
2.1 Schematic diagram of the one-lump thermal model (AC-Calorimetry)..	35
2.2 AC-calorimeter block diagram is showing the bath content and all the connections to the instruments.....	39
2.3 Schematic of an AC-capacitance bridge dielectric spectrometer.....	45
3.1 DNA liquid crystal phase evolution as a function of structure concentration.	53
3.2 Sketch of the self-assembly process leading to the LC alignment of well-paired short DNA duplexes. (a) Complementary and partially complemen-	

tary sequences pair into helices. (b) Units orientationally and positionally ordered into LC phases (c), chiral nematic N* and hexagonal columnar COL. (d) Upon cooling a mixture of single-stranded molecules..... 54

3.3 Possible structure/base pair combinations of the nucleotide sequence studied. Bases are held together by H-bonds (red dot), where a) is the hairpin structure and b) – a) are possible configurations. 57

3.4 Wide-temperature scans at ± 0.017 K/min of the heat capacity amplitude on heating (circles) and cooling (triangles) of a fresh DNA sample ($\varphi_w = 0.3$), show a reproducible heat/cool thermal behavior at an oscillation frequency with 40 mHz and an estimated $T_{AC} \cong 0.08$ K..... 62

3.5 Top panel – Real excess specific heat. Bottom panel – Imaginary specific heat. Temperature scan using AC-calorimetry of 60 wt% ($\varphi_w = 0.6$) DNA at 0.017 K/min over the temperature range 320 to 370 K. Structural mesophases and disassociations of the base pairs are probed on the 325 – 355 K range. The most evident feature is the small peak at 349 K. 64

3.6 Reversible (real) heat capacity as a function of temperature for different concentration (DNA+IDTE) at +1 K/min using the MDSC. Blue triangles are results for the $\varphi_w = 0.21$ sample and red circles for the $\varphi_w = 0.48$ sample. These small changes of reversible heat capacity values represent the evolution of the energetics of the DNA structural transition mainly for temperatures less than 335 K, before the “melting” (strand separation) takes place. The DNA “melting temperature” (the peak maximum) is shifted ~ 5 K

toward the highest temperatures for high ϕ_w 65

3.7 Reversible (real) heat capacity as a function of temperature for different temperature scan rates on the same (DNA+IDTE) concentration, $\phi_w = 0.3$. Blue triangles show the MDSC profile for 1 K/min, green circles for 2 K/min and red squares for 0.22 K/min (a small step, clear evidence of some energy release is present only for this heating rate). The vertical dashed arrow indicates the “melting” of the DNA structure at about 335 K. 67

3.8 Dielectric constant by AC-capacitive bridge technique. Frequency scans of DNA+IDTE for different DNA concentrations $\phi = 0.6$ (green squares), $\phi = 0.6$ (blue triangles) and buffer (red filled circles). Top panel – Real part and Bottom panel – Imaginary part. Here, the relaxation frequency increases while the strength (peak height of ϵ'') decreases as ϕ_w increases. In addition to the first mode, for $\phi_w = 0.3$, another mode with different character is shown at frequencies greater than 3.16 kHz. 69

3.9 Cole-Cole plots of imaginary part $\epsilon''(\omega)$ versus real part $\epsilon'(\omega)$ for different DNA concentrations, $\phi_w = 0.3$ (blue filled triangles) and $\phi_w = 0.6$ (red filled circles). Note that the direction of increasing frequency is toward the 0 of $\epsilon'(\omega)$ axis. The dash-dot line indicates the expected Cole-Cole behavior for one of the modes. 70

3.10 Phase diagram of structure evolution as a function of temperature in highly packed DNA environment showing both the main structural groups

(hairpins and double strands) through intermediate phases between 300 and 335 K. The structures may form crystal like phases below 300 K, but for high temperatures, greater than the melting temperature T_m , only the disassociated nucleotide strands can still exist.73

4.1 Primary structure of lysozyme. Peptide chain made out of 129 aminoacids and disulfite bridges, connected by covalent bonds (red lines)..... 83

4.2 Real part of the specific heat, Rev C_p (open circles) and dielectric storage, ϵ' (filled circles) at 100 kHz on powder lysozyme, as function of temperature (heating rate +0.22 K/min). A glass transition is evident at ~120 °C on both graphs.....85

4.3 Imaginary part of the specific heat, NonRev C_p (open circles) and dielectric loss ϵ'' (filled circles) at 100 kHz on powder lysozyme, as a function of temperature (heating rate +0.22 K/min). A glass transition is evident at ~120 °C on both graphs.....86

4.4 AC-calorimetry on diluted lysozyme. Effective heat capacity C^* and phase shift Φ as a function of temperature at +0.017 K/min on lysozyme concentration $\varphi = 0.30$. The dash-dot lines indicate the transition temperatures respectively. The first two (at 51 and 55 °C) may belong to untangling of α -helixes, β -sheets ($\alpha\beta$ -intermediate) and to further straightening of β -sheets (α -intermediate).87

4.5 Thermal cycling on diluted lysozyme $\phi_w = 0.32$ showing the excess specific heat ΔC_p , as a function of temperature at ± 0.22 K/min. Both heating profiles (red triangles-first heat and red stars-second heat) show the thermal signatures at 67 and 84 °C. The 84 °C peak is not present on cooling (blue circles) that was intermediate between the two heating scans.....89

4.6 Concentration effect on the excess specific heat ΔC_p over a wide temperature range on Lysozyme+PBS at a fixed heating rate +0.22 K/min. For the highest concentration $\phi \approx 0.32$ (green circles), two peaks are shown compared to other thermal profiles for $\phi \approx 0.19$ (red triangles) and $\phi \approx 0.07$ (black stars), where only one peak is present. The 84 °C peak for $\phi \approx 0.32$ present the protein gelation peak. The blue circles are an illustration of the native molecule structures that will unfold and tangle (arcs) for high temperatures.....90

4.7 Temperature scan rate effect on lysozyme+PBS for the same concentration ($\phi_w \approx 0.07$) on the excess specific heat. Real part of specific heat $\text{Re} C_p$ as a function of temperature T shows the dependence of the unfolding peak displaced by ~ 5 K toward higher temperatures as the scanning rate increases from 0.10 K/min (black filled squares) to 4 K/min (blue opened circles). The small figure inside shows the dependence of the peak maximum temperature T_{max} as a function of scan rate. Error bars come from reproducibility, not just instrumentation.....91

4.8 Cole-Cole plots of imaginary part $\epsilon''(\omega)$ versus real part $\epsilon'(\omega)$ for different protein concentrations and at a constant voltage $V = 5$ V. Note that the direction of increasing frequency is toward the 0 of $\epsilon'(\omega)$ axis. The first mode is not evident on all the graphs because of the noise present due to loss of sensitivity of the instruments. The second mode appears on two different frequencies for different protein solutions ($f = 7.5$ Hz) and buffer ($f = 8$ Hz).....92

4.9 Folding/unfolding schematic of lysozyme. The α -helices are in red and blue, β -sheets are in yellow and blue.....95

5.1 CDLC microstructures. Phase contrast optical microscopy of a CDLC sample at room temperature illustrating the typical coexisting microstructures present. The micrograph width represents $20 \mu\text{m}$ 105

5.2 Temporal evolution of structures as a function of temperature and concentration. Left panel shows phase-contrast micrographs of microstructures at 1:10 CDLC concentration (stock:additional water) at 31°C (column A1) and 60°C (column A2). Right panel shows phase contrast micrographs of microstructures at 1:1 CDLC concentration at 31°C (column B1) and 60°C (column B2). Each micrograph width represents $14 \mu\text{m}$. For the 1:10 sample at 31°C (low temperature, low concentration, A1), the coexisting structures generally exhibit straightening, elongation, and alignment over time. For the 1:1 sample at 31°C (low temperature, high concentration, B1), the structures progress through straightening, elongation, and clustering. For the 1:10 sample at 60°C (high temperature, low concentration, A2), the structures exhibit

straightening, thickening, and alignment over time. For the 1:1 sample at 60 °C (high temperature, high concentration, B2), the structures progress through straightening, thickening, and clustering. 110

5.3 Heat capacity and phase by modulation calorimetry. Wide-temperature scans at ± 0.01 K/min of the heat capacity amplitude C (top panel) and phase shift ϕ (bottom panel) on heating (open circles) and cooling (solid circles) of a fresh 1:1 concentration CDLC sample. Note that the decreasing baseline in the top panel reflects the slow evaporation of water from the cell 112

5.4 Heat capacity by modulation calorimetry. The heat capacity C (open circles) and phase shift ϕ (solid circles) of a hermetically sealed cell containing a 1:1 concentration CDLC sample on heating at $+0.017$ K/min. The cell catastrophically ruptures at about 74 °C. 114

5.5 Excess specific heat by DSC. Extracted excess specific heat ΔC_p on heating at $+1$ K/min scan rate of a 1:1 concentration CDLC sample. The initial rapid decrease of ΔC_p from 23 to ~ 28 °C is due to the typical transient at the start of the DSC heating scan..... 115

5.6 Microstructure evolution cartoon depicting the temporal evolution of microstructures through a free-energy landscape towards full crystallization into cholesterol monohydrate (ChM). The free-energy gradient, which is proportional to the rate of evolution kinetics, increases with increasing temperature. Generally, for a) low CDLC concentration, the structures progress from straightening to elongation or thickening to alignment. For b) high CDLC

concentration, the structures progress from straightening to elongation or thickening to clustering. The points A1, A2 in a) and B1, B2 in b) correspond to the panels in Figure 5.2. The temperature T_m refers to the melting temperature of ChM..... 118

5.7 Temperature-concentration pseudo-phase diagram for CDLC. Proposed phase diagram for the CDLC system combining the optically observed structures with the temperature of features observed by calorimetry..... 120

Acknowledgment

I would like to express my deep gratitude to my thesis advisor, Prof. Germano Iannacchione, it was with great pleasure that I worked under his supervision. Prof. Iannacchione, taught me a lot about experimental physics, presentation techniques and technical writing. His expertise, understanding, and patience, added considerably to my graduate experience.

I wish to thank both Professors Izabela Stroe and Georgi Georgiev, for serving on my thesis committee.

A very special thanks goes out to all other members of the WPI Physics Department for their kind help throughout my career in WPI. I recognize that this research would not have been possible without the financial assistance of the Physics Department through Teaching Assistantship.

I also want to thank Dr. Alexander Roshi for his suggestion and help in my application for the PhD program here at WPI and Prof. Yevgeniya Zastavker for her collaborative contribution.

Lastly, I would like to thank my family for their love and support they always provided me.

CHAPTER 1

INTRODUCTION

1.1 Thermodynamics

Thermodynamics help us to understand how the heat is transformed into mechanical work. The experimental work done in this dissertation involves thermal parameters such as the free energy, latent heat, enthalpy, heat capacity, etc. The basics of thermodynamics can be summarized by two ideas:

1. Energy is conserved (First law)
2. Entropy increases (Second law)

The energy and entropy are two abstract concepts that are not easily defined. Thermodynamics describes the properties of macroscopic systems without taking on consideration the atomic constitution of the matter. The first step in applying thermodynamics is to select the system of interest. The system is a separated part of the universe from the surroundings defined by a fixed

boundary. The boundary may be real or imaginary and may or may not be fixed in shape or size. The surroundings are the rest of the universe that can in any significant way affect or be affected by the system. An open system can exchange matter with its surroundings, but a closed system cannot.

To describe a process in terms of thermodynamics, the system must be in thermodynamic equilibrium. It is in equilibrium if its properties can be consistently described by the laws of thermodynamics. A system is not in equilibrium if its measurable macroscopic properties (such as temperature, pressure and density) change with time. The state of the system can be described in terms of thermodynamic coordinates such as, pressure P , volume V and temperature T .

A system is called thermally isolated if it is enclosed by insulating walls. There is no energy (E) transferred to or from the system by temperature differences. The work done on such a system equals the change in E from state 1 to state 2 given as:

$$W = E_2 - E_1 = \Delta E. \quad (\text{adiabatic process}). \quad (1.1)$$

The energy E characterizes the state of a microscopic system and it is independent of the path reaching that state. If the system is allowed to interact with surroundings, we can find that $\Delta E \neq W$. The energy of the system is a state function [1].

If there are a fixed number of particles N , the change of the energy for the closed system is:

$$\Delta E = W + Q \quad (\text{The first law of thermodynamics}), \quad (1.2)$$

The quantity Q is the change in the system's energy due to heating ($Q > 0$) or cooling ($Q < 0$), W is the external work done on the system and may be replaced by PV . The first law is a statement of the conservation of energy.

The internal energy of the system can be identified with the sum of the kinetic and the potential energies of the particles. Another important property of the system that should be considered, called the entropy, S , is another state function and it cannot be measured directly. This new state function is used to determine the reversibility of processes.

The second law of thermodynamics can be written as:

$$dS \leq \frac{dQ}{T}, \text{ where } \left\{ \begin{array}{ll} dS > 0 & \text{irreversible} \\ dS = 0 & \text{reversible (never negative)} \end{array} \right\}$$

or

$$dQ = TdS \quad (\text{only for adiabatic processes}). \quad (1.3)$$

If we use Equation (1.3) for an infinitesimal quasistatic change in the energy along with an infinitesimal change in volume, then Equation (1.2) becomes

$$dE = TdS - PdV. \quad (1.4)$$

Another equation of interest in thermodynamics is the Legendre transformation of E by P, V variables giving:

$$H = E + PV, \quad (1.5)$$

where the enthalpy H is another state function. It defines the amount of work

that a system can do in an adiabatic, isobaric process.

Derivatives of one thermodynamic parameter with respect to another under specific conditions on the remaining variables are called thermodynamic response functions. If due to an energy transfer Q , the body temperature changes from T_1 to T_2 then the ratio $Q/(T_2 - T_1)$ is called the average heat capacity and depends on the imposed constraints. The heat capacity is a thermodynamic response function and at constant volume is given by:

$$C_V = \left(\frac{\partial E}{\partial T} \right)_V . \quad (1.6)$$

Using Equation (1.5) we can define the heat capacity at constant pressure by:

$$C_P = \left(\frac{\partial H}{\partial T} \right)_P . \quad (1.7)$$

There are still two more thermodynamic state functions to be introduced, the Helmholtz F and Gibbs free energy G , defined as a Legendre Transform of the internal energy and entropy given by:

$$F = E - TS \quad (1.8)$$

and

$$G = E - TS + PV. \quad (1.9)$$

In a reversible process, a small change in the Helmholtz free energy allows Equation (1.8) to be written as:

$$dF = dE - d(TS) = -SdT - dW . \quad (1.10)$$

At constant temperature

$$dF = -dW . \quad (1.11)$$

Based on Equation (1.11), we can use the Helmholtz free energy to measure the amount of work a system can do in an isothermal reversible process.

The Gibbs potential measures the amount of work a system can do at constant pressure and temperature [2]. After all the heat capacity at constant pressure is given as well by:

$$C_P = T \left(\frac{\partial S}{\partial T} \right)_P = -T \left(\frac{\partial^2 G}{\partial T^2} \right)_P . \quad (1.12)$$

In an adiabatic process, the energy can change due to a change in volume or temperature and referring to Equation (1.2) we can write:

$$dE = dW = -PdV, \quad (1.13)$$

$$dE = \left(\frac{\partial E}{\partial T} \right)_V dT + \left(\frac{\partial H}{\partial T} \right)_P dV . \quad (1.14)$$

Helmholtz free energy is the thermodynamic potential found in a system of constant parameters (temperature and volume), so it is found easier (by exper-

imentalists) to “play” with Gibb’s potential, since most of the experiments involve temperature changes.

1.2 Bio-Thermodynamics and Transitions of Biological Molecules

Today equilibrium thermodynamics is well established. The direction of chemical or physical changes can be quantified by a change in entropy S of the system and surroundings. The role of calorimetry is to give a numerical value for each thermodynamic variable with an appropriate unit through measurement [3]. Most of the calorimetric data are based on the measurements of heat Q and temperature T . This needs high accuracy measurement and precision for a well-characterized sample. Equation (1.15) holds for any first order phase transition that is caused by crossing off the Gibbs energies G of two phases at a particular temperature T_c with different slopes $(\partial G/\partial T)_P$,

$$(\Delta P/\Delta T) = (\Delta S/\Delta V). \quad (1.15)$$

The work presented here is related to physical changes such as, structural transitions, monomer arrangements, interactions, and molecular orientations of biological systems. All of these processes are exothermic or endothermic. Using calorimetric methods, the heat capacity will be measured and the physical system will not be destroyed or affected. As we probe the heat

capacity profiles, the transition peaks will show features similar to first order phase transition.

The most common characteristic of all the systems studied here, is that, they are all stable (native structure not affected) in aqueous solutions at room temperature. Proteins, sugars, DNA (double stranded or hairpins), lipids, nucleic acids, cholesterol structures are important components of biological systems. It has been demonstrated [4, 12] that in order for the above components to function properly, they should maintain their native structure (proteins, DNA) or the ordered molecular arrangement (nucleic acids, lipids). Measuring the heat capacity will gain insight to the energetics of molecular structure for all the systems studied.

1.3 Using Dielectric Spectroscopy on Biopolymers

Dielectric spectroscopy can provide information about the mobility of a polymer by probing its dielectric properties. If an external field is applied across the plate capacitor, the alternating electric field interacts with the electric dipole moments of the polymer. Equation (1.16) is the relation between the polymer polarization P and the applied electric field E , where χ_e is the electric susceptibility of the material.

$$\vec{P} = \chi_e \vec{E} \quad (1.16)$$

There are four different dielectric mechanisms involved: space charge polarization, orientation or dipolar, atomic and electronic polarization (**Figure 1.1**).

Each of these mechanisms is related to its characteristic relaxation frequency as we increase the applied frequency, the slower mechanisms drop off [5]. The induced moments for electronic and atomic polarization are dependent on the polarizability of the atoms or molecules. The external electric field

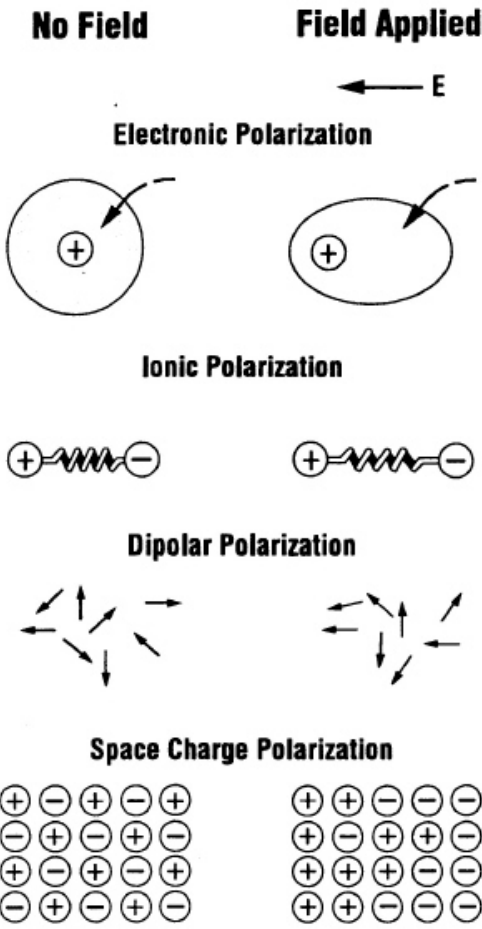


Figure 1.1. Mechanisms of electric polarization [23].

will rotate these random oriented dipoles and a net polarization will be present. This polarization of the medium will produce an electric field that will oppose the external one (**Figure 1.2**) and it can be written as,

$$E_{effective} = E - E_{polarization} . \tag{1.17}$$

The ionic conductivity in a medium contributes on ionic polarization of it. At low frequencies, ionic conduction is the most prevalent mechanism and introduces only losses to the system.

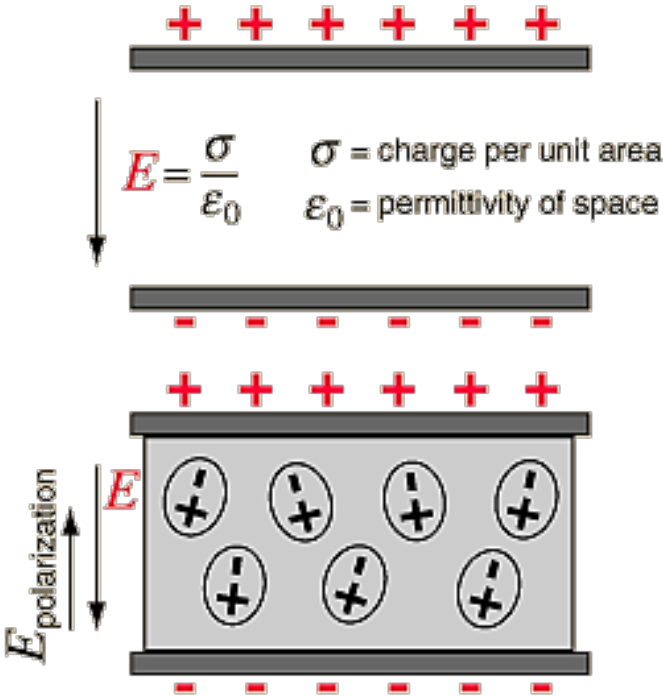


Figure 1.2. The effect of polarization in the dielectric media [22].

The electronic transition or molecular vibrations have frequencies above 10^{12} Hz. If the changing electric field is in the frequency range of $10^2 - 10^{10}$ Hz then the movement of dipoles or electric charges will result on dielectric relaxation spectra of the polymer (**Figure 1.3**).

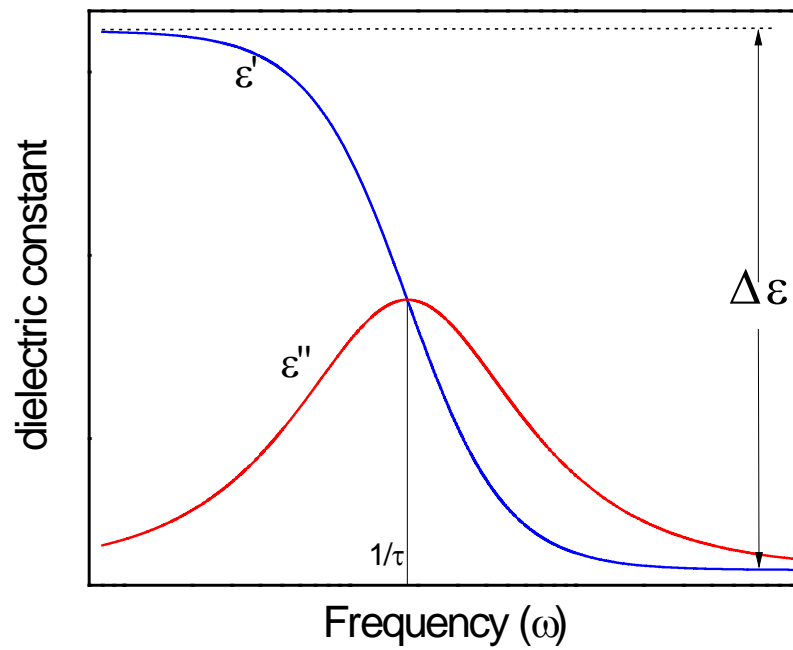


Figure 1.3. Frequency dependence of $\epsilon'(\omega)$ and $\epsilon''(\omega)$ for a relaxation process [24].

It is shown [6] that under an alternating electric field, the real and the imaginary components of the dielectric constant are given respectively as,

$$\varepsilon' = \varepsilon_{\infty} + \left[\frac{\Delta\varepsilon}{1+(\omega\tau)^2} \right] \quad (1.18)$$

and

$$\varepsilon'' = \left[\frac{\Delta\varepsilon}{1+(\omega\tau)^2} \right] (\omega\tau), \quad (1.19)$$

where $\Delta\varepsilon = \varepsilon_0 - \varepsilon_{\infty}$ is called the dielectric relaxation strength for a single relaxation process, τ is called the relaxation time, ω is the sweeping frequency, ε_{∞} is the dielectric constant at infinite frequency, ε_0 the static dielectric constant.

Since the dielectric constant of a dielectric material is a complex number, it can be expressed as,

$$\varepsilon^*(\omega) = \varepsilon' - i\varepsilon''. \quad (1.20)$$

The real part of the dielectric constant $\varepsilon'(\omega)$ is associated with the storage of the electric field energy while the imaginary part $\varepsilon''(\omega)$ corresponds to the loss of energy through a relaxation process.

The dielectric constant, also can be given by the equation

$$\varepsilon^*(\omega) - \varepsilon_{\infty} = \frac{\varepsilon_0 - \varepsilon_{\infty}}{1+(i\omega\tau)^{1-\alpha}} \quad (1.21)$$

Where the exponent parameter α , which takes a value between 0 and 1, allows to describe different spectral shapes. Equation (1.21) is known as Cole–Cole equation that is often used as a model to describe dielectric relaxation in polymers [5, 6].

1.4 The Effect of Solvent Water on Bio-assemblies

Water participates in the majority of the biological processes such as the metabolism of nutrients catalyzed by enzymes, which need to be suspended in an appropriate solvent to adopt their active 3D structure and be effective. Through water, our cells can communicate and bring the oxygen and nutrients to our tissues and as well allow the elimination of cellular metabolic residues. Water is very important since mobility, structure, stability and function of biomolecules (proteins, nucleic acids) and biological assemblies (membranes) are dependent on the aqueous environment. Water’s polarity, high dielectric constant and small molecular size makes it an excellent solvent for polar and ionic compounds.

The hydrophobic effect is important in biological systems because it is involved in folding/unfolding of proteins and other macromolecules. Many of the physical properties of water (high melting point, high viscosity and surface tension) are due to hydrogen bonds between adjacent water molecules. One water molecule can participate in four hydrogen bonds which results in a network formation.

Furthermore of great importance is the understanding of how the water dynamics affect the biomolecular surfaces. The orientation of the confined water molecules depends on the chemical nature of the surface. **Figure 1.4** illustrates how water molecules (gray hydrogen and red oxygen atoms) surround the protein β -sheets (green) and the residues (yellow).

The changes in the properties of hydrated environment are responsible for some of the changes in the dynamics of the protein and DNA biomolecules and other structures found in this environment [8]. Dry proteins show no biological function. The protein function starts when the hydration level is around 0.2 g water per protein volume. As the hydration is increased, the dynamics and the function are increased.

There will be different hydration layers depending on the interactions with surrounding molecules and the distance to the biomolecule [9, 10, 11, 12]. The motion of the water molecules on the hydration shell makes possible the proton diffusion between the hydration layer and the protein motion itself. Translational motion of the surrounding water molecules is necessary for the protein function, which is dependent on the protein structural changes.

Protein functions often involve conformational changes, which in some way are promoted by the solvent. That is why is so important to know the properties of the solvent. In order to avoid the so-called water anomalies [7, 8] most of the systems shown in this work, have been studied from 300 to 360 K.

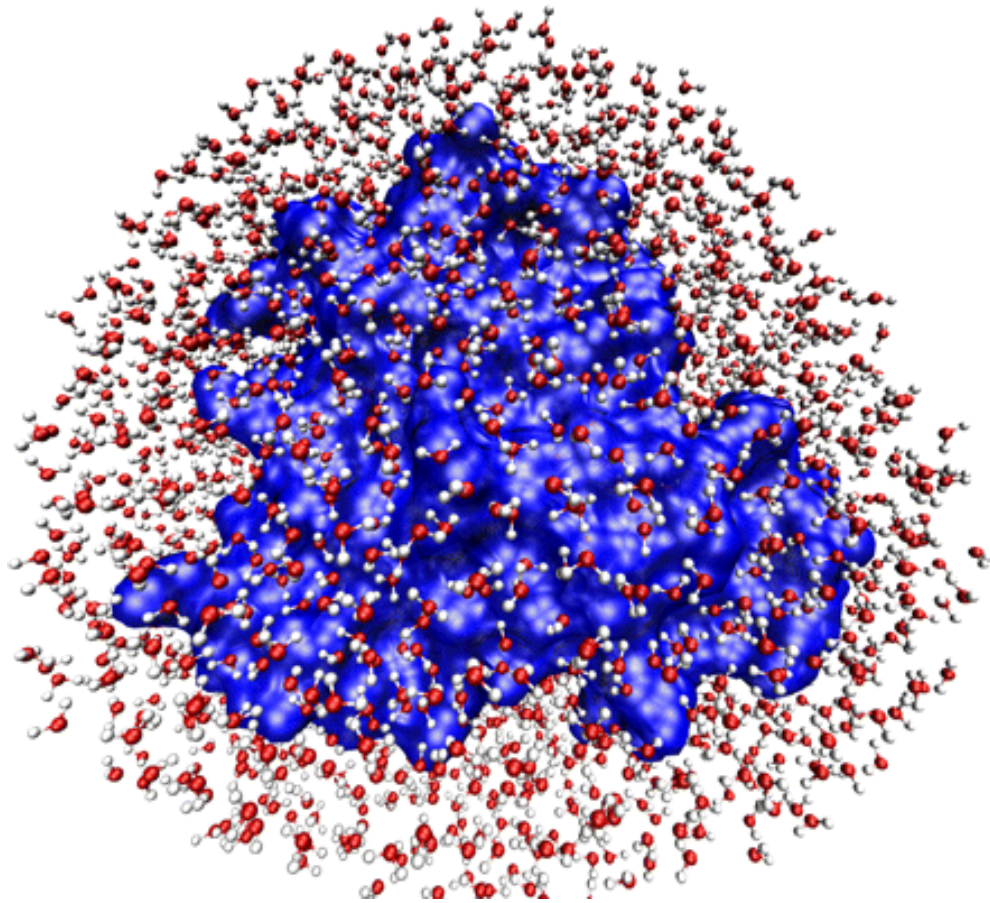


Figure 1.4. *The hydration shell of myoglobin (Mb). Diagram of myoglobin (blue surface) with water molecules (CPK model). The water molecules here form a shell $\approx 5 \text{ \AA}$ thick around the protein [25].*

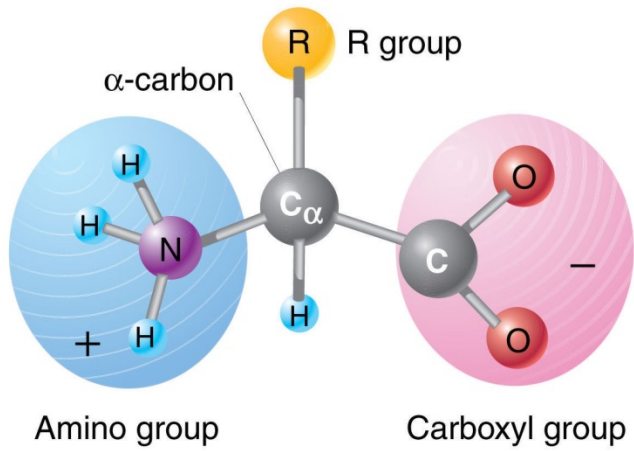
1.5 Overview of Proteins

1.5.1 The structural basis of protein function

Since the dynamics and the kinetics of a protein is related to its structure, we first provide an introduction of the main structural elements of the protein.

Each protein consists of a polypeptide chain that is made up of amino acids linked together by peptide bonds. The polypeptide chain backbone, is composed of repeating units that are identical, except for the terminal part. Proteins vary widely from 1000 to 10000 or so atoms. Approximately half of the atoms are hydrogen, but the proteins are described based on the position of the other atoms, C, N, O and S. Also the proteins are distinguished based on the sequence of amino acids in the polypeptide chain (**Figure 1.5**). There are found 20 amino acids and they differ in their side chains. The sequence of the amino acids determines the primary structure of the protein (**Figure 1.6**). This native conformation, under certain physiological conditions, stays stable. It is possible to denature (unfold) many proteins in solutions by lowering the pH or increasing the temperature. Some of the proteins can recover the native structure by returning the solution to normal values of temperature or pH [13].

The folding of the polypeptide chain has certain regularities that create the secondary structure. The most important structural elements of it, are α -helix and β -pleated sheets. Some proteins do not have the secondary structure but they still have some regularity on their amino acid packing. The backbone of these regularly repeated structures is made of hydrogen bonds. These bonds stabilize peptide amide and carbonyl groups.



© 2010 Pearson Education, Inc.

Figure 1.5 *Amino acid Structure* [26].

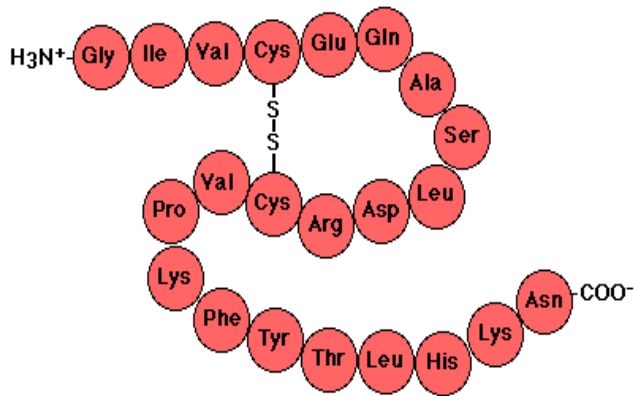


Figure1.6. *Primary Structure (Peptide Chain)* [19].

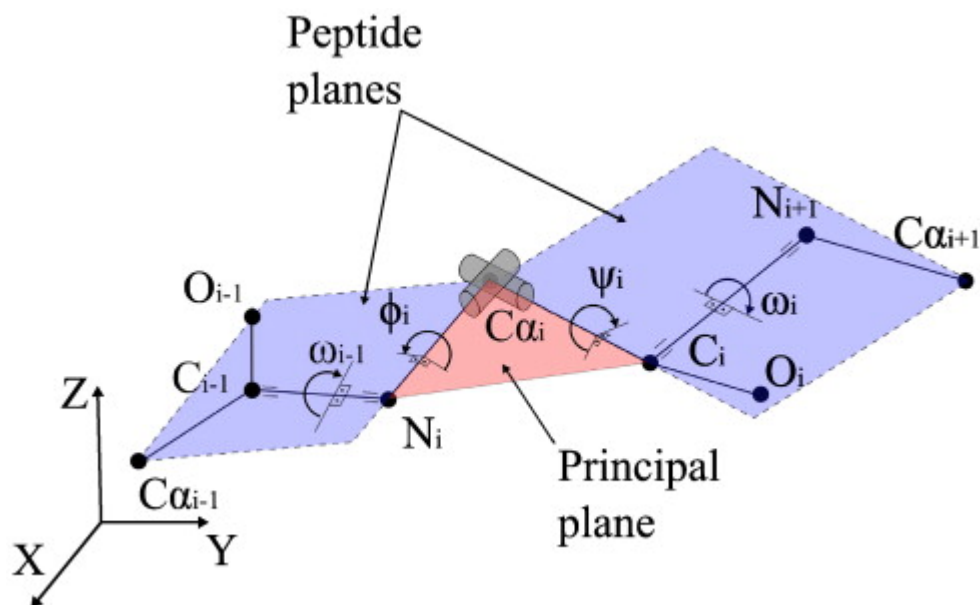


Figure 1.7: *The repeated dihedral $\{\phi, \psi\}$ angles and the peptide planes [27].*

If the backbone of the polypeptide chain forms a linear group (the dihedral $\{\phi, \psi\}$ angles are repeated), then this group is a helix (**Figure 1.7**). Each helix has a polarity, because the peptide unit is polar. A pair of dihedral angles describes each regular helix.

Some polypeptide chains can associate by hydrogen bonding to form sheet-like structures. Pauling and Corey postulated the (planar) parallel, anti-parallel β -pleated sheets and suitable hydrogen-bonded structures for polypeptide chains. However most observed sheets are nonplanar with a left handed or right-twist [14].

At a higher level of complexity are found aggregates of so-called super secondary structures. These aggregates are favored during the folding

process and/or are found in the folded protein for energetic reasons. The most common super secondary structures are: the coiled-coil α -helix (occurs

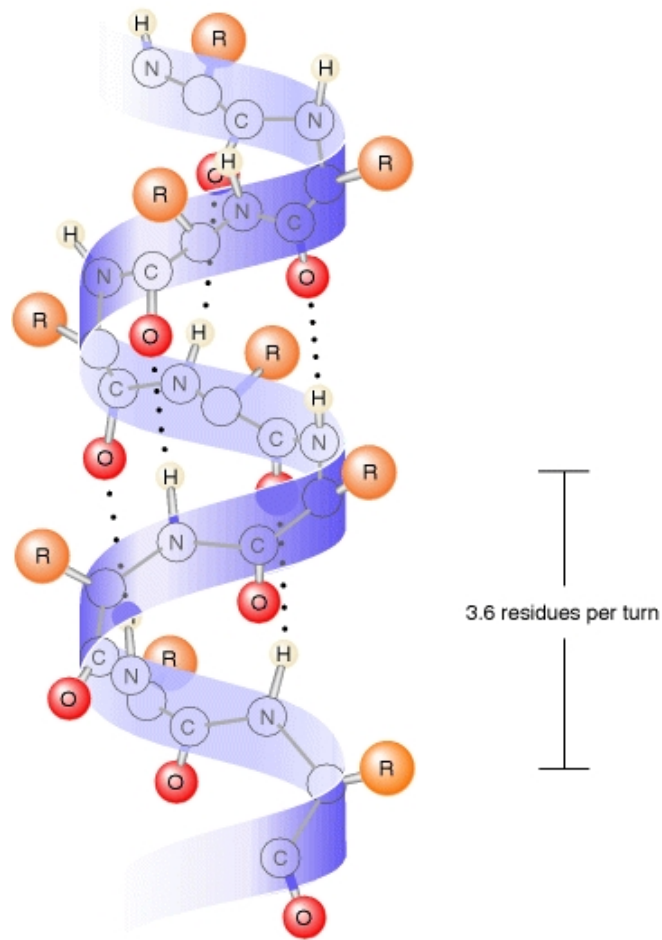


Figure 1.8. *Protein Secondary structure: α -helix and the hydrogen bonds (black dotted lines) [19].*

in fibrous proteins), $\beta\xi\beta$ -unit (two parallel strands of a β -sheet with a connection ξ in between) observed in globular proteins. In addition, interesting combinations of $\beta\alpha\beta$ unit have been found in a number of proteins (**Figure 1. 8 and 1. 9**).

The overall arrangements of the amino acid residues in proteins are referred, as the tertiary structure. Oligomeric proteins are composed of several unconnected polypeptide chains (subunits) that usually, but not always, fold up independently and assemble to complete the protein.

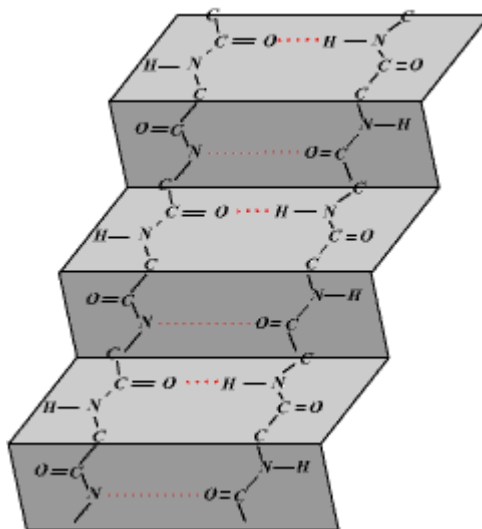


Figure 1.9 *Protein Secondary structure: β -sheet and the hydrogen bonds (red dotted lines) [19].*

This arrangement of the subunits is referred as the quaternary structure. A well-studied oligomeric protein is hemoglobin ($\alpha_2\beta_2$) where α , β refer to different types of subunits.

In general, proteins are tightly packed systems. Nonpolar side chains of the amino acids tend to be in the interior of the protein forming a stabilizing core. Polar residues as well as the carbonyl and amide groups of the polypeptide chain, tend to be more uniformly distributed. There are located all hydrogen-bond donors and acceptors so they form bonds either with other parts of the protein or with the surrounding solvent [13].

1.5.2 Forces determining the protein structure

In the previous paragraph, we discussed the most common structure combinations found in proteins. It is very important as well, to understand the nature of the forces that hold these structures together in a folded state. The formation of stable tertiary folds relies on interactions that differ in their relative strengths in proteins.

I. Noncovalent forces

Noncovalent forces are very important for biological organisms. They drive the folding of polypeptide chains, nucleic acids, formation of membranes, etc. They are difficult to measure and calculate. Van der Waals potentials comprise Dispersion Forces, Electron Shell Repulsion and electrostatic interactions.

Dispersion Forces and Electron Shell Repulsion

Each atom can be approximated to an oscillating dipole generated by electrons moving in relation to the nucleus. Each dipole will polarize its neighbor atom creating coupled oscillators. The dispersion forces are attractive and relative to the orientation of the molecular groups. They are very small and neglected. These attractive forces are counter-balanced by repulsion of the electronic shells between non-bounded atoms.

Electrostatic Interaction

The atoms that carry partial charges stay covalently bonded to each other creating an asymmetric bond electron distribution. Most of the atoms in a molecule carry partial charges. Still the molecule itself is neutral since does not have a net charge. Electrostatic forces (Coulomb's law) govern the dipole interactions within the molecule. The interaction energy depends on the dielectric constant ϵ of the surrounding medium. It is difficult to calculate the exact value of ϵ for microscopic dimensions. In proteins, electrostatic interactions are of a local nature [15]. If the dipoles themselves can be aligned, there can be weak long-range interactions. In β -sheets adjacent dipoles are antiparallel so that their fields cancel each other. The dipole lines, formed in α -helices, cancel each other except for the charges at both ends. However, this energy contribution is very small compared to the binding energy between α -helices.

Van der Waals Interactions

Van der Waals forces between atoms are very important in protein folding. These can be attractive or repulsive and are the interactions that occur between non-bonded atoms due to fluctuating charge densities within atoms. The energy of interaction varies as the inverse sixth power of the interatomic separation distance (r) and is dependent of the polarizability of the molecules and the temperature. When atoms approach very closely, the repulsion arises and becomes the dominant interaction by r^{-12} distance dependency. The Van der Waals potential E_{vdw} is the sum of all interactions over all atoms and is described mathematically by the difference between the attractive and repulsive terms where, ϵ is the depth of the potential well and

$$E_{vdw} = \sum \epsilon [(R_m / r)^{-12} - 2(R_m / r)^6] , \quad (1.21)$$

R_m is the minimum energy interaction distance. The most common illustration of the Van der Waals interactions is described by the plots of the potential energy as a function of interatomic separation distance. (**Figure 1.10**). The Van der Waals forces are extremely weak, but their large number arranged close together in protein make these interactions significant to the maintenance of tertiary structure.

Hydrogen Bonds

The resulting interaction energy is intermediate between the energies of Van der Waals contacts and covalent bonds. These are linear bonds. The covalently bound neighbors (H-donor and the covalent neighbor of H-acceptor) carry opposite charges. The positively charged H-atom is located between two negatively charged atoms. The lowest potential energy is when the three charges are aligned [16]. Energies of hydrogen bonds are found to be about 3 kcal/mole between amide and carbonyl groups, which occur frequently between main chain atoms in polypeptides.

II. Covalent bonds

Disulfide Bridges

Covalent links between cysteine side chains in the primary sequence are called disulfide bridges (**Figure 1.6**) and cannot be formed between consecutive cysteine residues. The reduction of the disulfide bonds caused mainly by high temperatures or acidic pH will decrease the protein stability [14, 16].

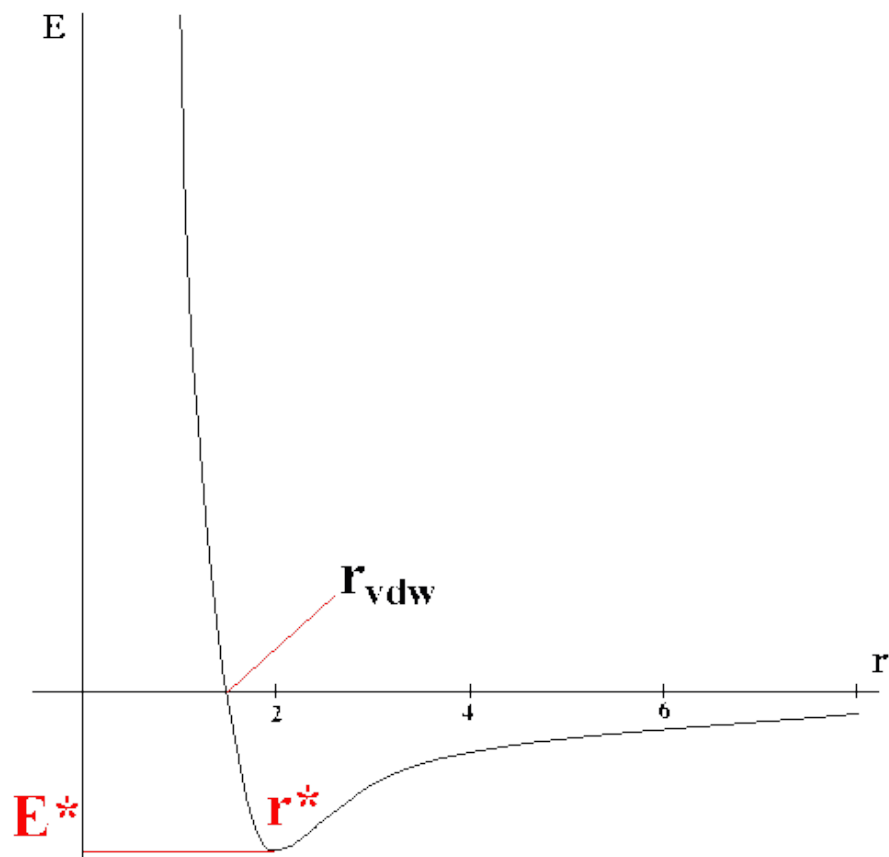


Figure 1.10. *The van der Waals potential energy function. Both, value of energy at the minimum E^* and the optimal separation of atoms r^* (which is roughly equal to the sum of Van der Waals radii of the atoms) depend on chemical type of these atoms. [20].*

1.6 DNA Structure and Conformation

DNA is a molecule, made of repeated units, nucleotides. A nucleotide consists of three components: a sugar, phosphate and one of four heterocyclic bases. There are two purine bases, adenine and guanine, and two pyrimidine, thymine and cytosine. The structures of these components are shown in **Figure 1.11** and **1.12**. This polynucleotide chain constitutes the primary structure of DNA. The specific pairing of the bases by hydrogen bonding creates the double-stranded DNA. The strands are antiparallel (two strands run in opposite direction). The strands are coiled around each other in a right-handed fashion. The interior is hydrophobic and the sugar-phosphate backbone on the outside is hydrophilic. The width of the double helix is approximately 2 nm and the bases are perpendicular to the helix axis. The distance between each repeated turn is 3.4 nm [16]. This is known as Watson-Crick Model and there are 10 base pairs (bp) for every turn of the helix. There are other models, but in real DNA the conformation of the molecule is determined by the hydrophobicity of the bases, the bond angles in the sugar-phosphate, the base-pairing between the two strands and the solution conditions. The DNA double helix is relatively stable structure, although conditions such as high temperature or extremes of pH cause disruption of the helix into its single-strand components. The hydrogen bond donor and acceptor groups of the DNA bases become exposed [17]. This chemical process is known as denaturation or melting of DNA. It involves breaking of two hydrogen bonds in adenine-thymine base pair and breaking of three hydrogen bonds in every guanine-cytosine base pair. The disruption and formation of base pairs in aqueous environ-

ment is essential for biological functions of nucleic acids in processes such as transcription and duplication of genes. Further on this work, it is shown that the thermodynamics of DNA short fragments is dependent on various factors such as sample concentration, temperature scan rate, etc. Experimental work has revealed great structural diversity in DNA, in terms of different double-helical forms and other conformational states.

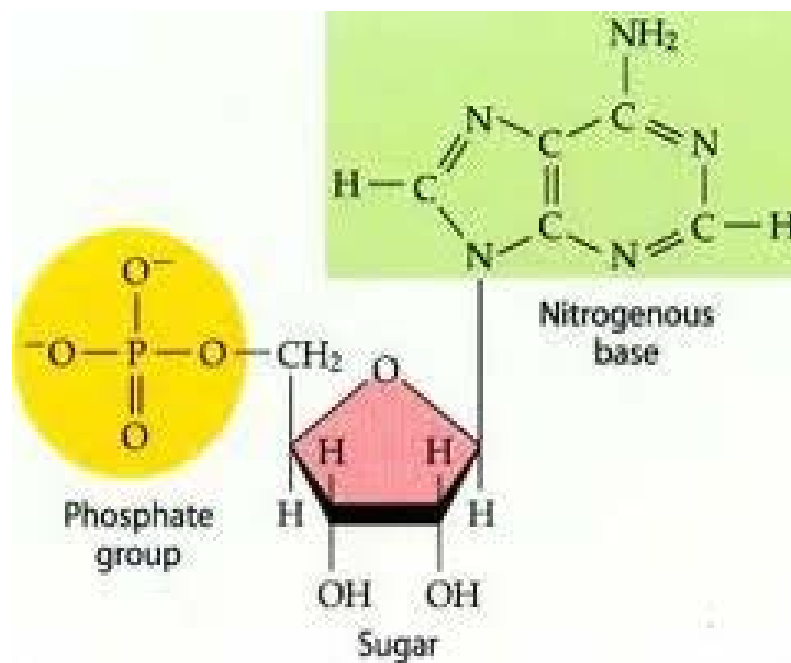


Figure 1.11. A nucleotide, the repeat unit of DNA [21].

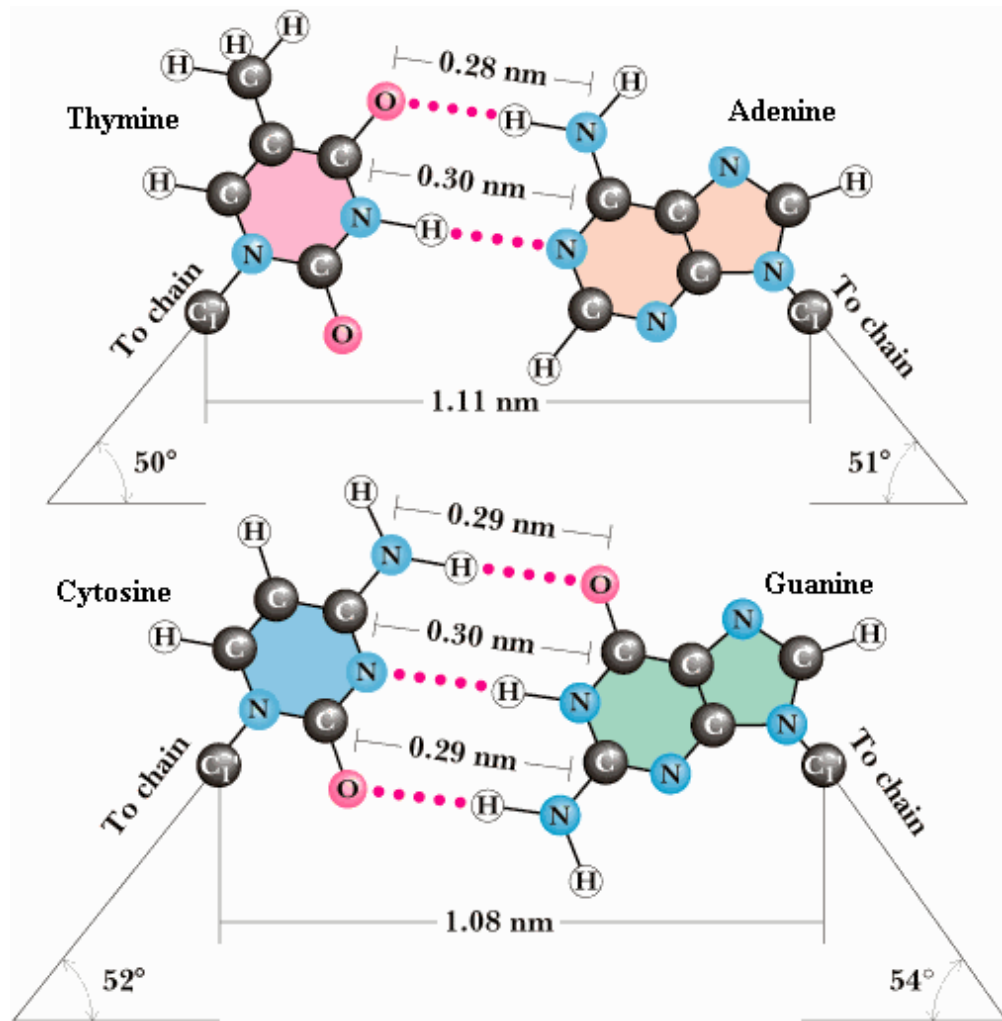


Figure 1.12. Base-pairing in DNA. Purine bases pair with pyrimidine bases, pink dotted lines indicate hydrogen bonds [21].

One of the interesting forms is the hairpin DNA. Hairpins provide a model system for studying DNA unzipping and are important for their role in gene transcription and regulation. These structures consist of single strands that loop back on themselves to form a duplex. This structural element is present in DNA and RNA molecules in vivo as well as in vitro. The aim of our research is to understand some of the factors that affect the stability and the self-assembling of short DNA hairpins in aqueous environment. One of the ways is to study the kinetics and the energetics of unfolding. Another interesting part is also to understand the dynamics involved on molecular orientation of macromolecules.

An interesting way is, to look at them as, highly cooperative “islands” swimming on the environment. By applying low frequency electric field and probing the dielectric constant, we can understand the orientation of this “islands”.

1.7 Cholesterol Structures in CDLC (Chemically Defined Lipid Concentrate)

Originally micro-scale filaments, helical ribbons, and tubules discovered in gallbladder bile (a quaternary solution of cholesterol, surfactants, and lipids) from the saturating of cholesterol and later found in many other solutions comprised of cholesterol analogs (sterols), surfactants, and phospholipids. The self-assembly of helical ribbons in this complex fluid have a wide geometric variety but nearly all have either 11° or 54° pitch angles. This unique

feature has yet to be understood. More of the physical characteristics are given elsewhere [18].

A model complex fluid that has provided a useful physical system for the study of such microstructures (**Figure 1.13**) is a Chemically Defined Lipid Concentrate (CDLC). CDLC is a quaternary sterol system consisting of a cholesterol, bilayer-forming amphiphiles, micelle-forming amphiphiles, and water. This system exhibits a wide-range of micro-structure formation from filaments to helical ribbons to tubules to crystals. Understanding the physics of these self-assemblies, their evolution and properties, may lead to engineering these micro-structures for a range of useful technical applications, i.e. micro-scale force transducers.

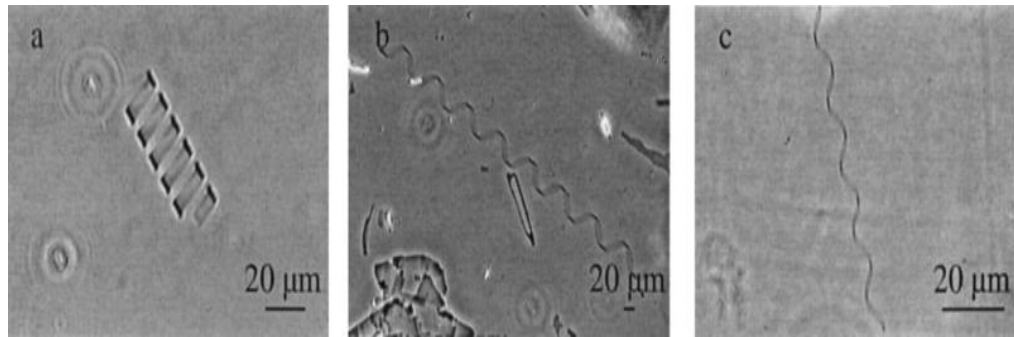


Figure 1.13. Typical helical structures in CDLC system. (a) Low pitch helical ribbon with a pitch angle $\psi = 11 \pm 2^\circ$. (b) High pitch helical ribbons with a pitch angle $\psi = 54 \pm 2^\circ$. (c) Intermediate pitch helical ribbons with a pitch angle $\psi = 40.8 \pm 3.8^\circ$ [18].

1.8 References

- [1] H. Gould and J. Tobochnik, *Princeton Review*, **3**, 32 (2005).
- [2] S. Singh, *Physics Reports*, **324**, 107 (2000).
- [3] Y. Tajima, T. Matsuo and H. Suga, *Nature*, **299**, 810 (1972).
- [4] P. Westh, C.A. Haynes, Y. Koga, *J. Phys. Chem. B*, **102**, 4982 (1998).
- [5] G.G. Raju, *Dielectrics in Electric Fields*, Dekker, New York, (2003).
- [6] A.R. Blythe, *Electrical Properties of Polymers*, Cambridge University Press (1979).
- [7] S.H. Chen, L.Liu, and A. Faraone, *Phys. Rev. Lett.*, **97**, 189803 (2006).
- [8] A.B. de Oliviera, G. Franzese, P.A. Netz and M.C. Barbosa, *J. Chem. Phys.*, **128**, 064901 (2008).
- [9] N. Nandi and B. Bagchi, *J. Phys. Chem. B*, **101**, 10954 (1997).
- [10] P. Wernet, D. Nordlund, U. Bergmann, M. Cavalleri, M. Odelius, H. Ogasawara, L.A. Nslund, T.K. Hirsch, L. Ojamae, P. Glatzel, L.G.M. Pettersson, and A. Nilsson, *Science*, **304**, 995 (2004).
- [11] P.W. Fenimore, H. Frauenfelder, B.H. McMahon, and R.D. Young, *Proc. Natl. Acad. Sci. USA*, **101**, 14408 (2004).
- [12] D. Vikup, D. Ringe, G.A. Petsko, and M. Karplus, *Nature Structural Biology*, **7**, 34 (2000).
- [13] J.A. Pople, B.T. Luke, M.J. Frisch, and J.S. Binkley, *J. Phys. Chem.*, **89**, 2198 (1985).
- [14] A.M. Lesk, *Introduction to protein architecture*, Oxford University Press (2001).
- [15] G. Von Jagow, H. Schaegger and C. Hunte, *Membrane Protein Purification and Crystallization*, Academic Press (2003).

- [16] C.A. Davey, D.F. Sargent, K. Luger, A.W. Maeder, and T.J. Richmond, *J. Mol. Biology*, **319**, 1097 (2002).
- [17] J. Widom, *Annu. Rev. Biophys. Biomol. Struct.*, **27**, 285 (1998).
- [18] Y.V. Zastavker, N. Asherie, A. Lomakin, J. Pande, J. M. Donovan, J.M. Schnur, and G.B. Benedek, *Proc. Natl. Acad. Sci. USA*, **96**, 7883 (1999).
- [19] <https://confluence.crbs.ucsd.edu/display/CS/Protein+Structure>, accessed 01/28/2013.
- [20] http://www.ch.embnet.org/MD_tutorial/pages/MD.Part2.html, accessed 01/28/2013.
- [21] R. H. Garrett and M. C. Grisham, *Biochemistry, Saunders College* (1995).
- [22] <http://hyperphysics.phy-astr.gsu.edu/hbase/electric/dielec.html>, accessed 01/28/2013.
- [23] <http://electrochem.cwru.edu/encycl/art-d01-dielectrics.htm>, accessed 10/05/2013.
- [24] R. Basu, *Ph.D. dissertation*, WPI, 2010.
- [25] H. Frauenfelder, G. Chen, J. Berendzen, P.W. Fenimore, H. Jansson, Izabela R. Stroe, B. H. McMahon, J. Swenson, I. R. Stroe and R. D. Young, *Proc. Natl. Acad. Sci. USA*, **106**, 5129 (2009).
- [26] P. J. Rusell, *iGenetics: A Molecular Aproach, Pearson Education* (2010).
- [27] M. Diez, V. Petuya, L. A. Martínez-Cruz, and A. Hernández, *ELSEVIER*, **46**, 1854 (2011).

CHAPTER 2

EXPERIMENTAL METHODS

2.1 Review of AC – Calorimetry

2.1.1 Introduction

AC-calorimetry is a well-established and very reliable technique. It has been used in many existing studies on several different systems, such as liquid crystal [1], low temperature properties of superfluid helium films adsorbed in porous glass [2], superconducting films [3], etc. AC-calorimetry has the following distinct features:

1. Heat capacity measurements are made in quasi-equilibrium condition. This is very important since most of thermodynamic theories of phase transition are based on equilibrium considerations.
2. Perfect thermal isolation of the sample from the surrounding is not required.

3. Only a small amount of sample is needed for high-resolution measurement. It is helpful for ensuring the thermal equilibrium as well as when large amount of a batch of a sample is not available.
4. Extremely high relative caloric sensitivity. Results better than 0.001% at low temperatures are typical.
5. It can measure thermal conductivity and dynamic heat capacity $C_p(\omega)$.
6. Very high temperature resolution (in the μK range) and very wide temperature range, from 50 mK to above 3000 K.

Although the relative accuracy is very high, the absolute accuracy of the measured heat capacity is about 1 – 10%, due to the sensitivity to the internal and external thermal relaxation times.

2.1.2 Theory of operation

Heating a sample by periodically modulated sinusoidal power and monitoring the resulting temperature oscillation is the basic principle of the AC-calorimetry technique. The basic equation of AC-calorimetry can be roughly calculated using the definition of heat capacity as,

$$C_p = \left| \frac{dQ}{dT} \right| = \left| \frac{dQ/dt}{dT/dt} \right| \cong \frac{P_0}{\omega T_{ac}}, \quad (2.1)$$

where, P_0 is the amplitude of the power oscillation, ω the power frequency, and T_{ac} the amplitude of the temperature oscillation. The heating power is applied through the heater and the oscillating temperature is obtained by the thermistor (heater and thermistor) is attached on the surfaces of the cell. Sullivan and Siedel [4] were the first introducing and analyzing a thermal model

shown in **Figure 2.1**, which is called *One-lump thermal model*. The model considers a heater (H) of heat capacity C_H and of temperature T_H , a sample (s) with heat capacity C_s and of temperature T_s , and a thermometer (θ) of heat capacity C_θ and of temperature T_θ interconnected by thermal conductances K_H and K_θ . The cell+sample+heater+thermistor system is connected to a thermal bath (b) of heat capacity C_b and temperature T_b via a thermal link of conductance K_b . The model assumes the zero thermal resistance between the sample and the cell. The heat-balance equations for the system are: $T = \partial T / \partial t$, [11]

$$C_h T'_H = P_0^{ei\omega t} - K_H(T_H - T_s), \quad (2.2a)$$

$$C_s T'_s = K_H(T_H - T_s) - K_b(T_s - T_b) - K_\theta(T_s - T_\theta), \quad (2.2b)$$

$$C_\theta T'_\theta = K_\theta(T_s - T_\theta). \quad (2.2c)$$

The steady-state solution for these equations will be:

$$T_\theta = T_b + T_{dc} + T_{ac} e^{i(\omega t + \Phi)}, \quad (2.3)$$

where, $T_{dc} = P_0/K_b$ is the rms temperature raise, Φ is the absolute phase difference between the applied power and temperature oscillations, and ω is the modulation frequency.

If we make the assumptions:

- (i) The heat capacities of the heater and of the thermometer are much smaller than that of the sample

(ii) The sample, the heater, and the thermometer come into equilibrium in a time (τ_i – internal time constant or relaxation time) much shorter than the modulation period i.e. $\omega \ll 1/\tau_i$

(iii) The modulation period is much shorter than the sample-to-bath relaxation time (τ_e – external time constant) i.e. $\omega \gg 1/\tau_e$

then the amplitude of the temperature oscillation can be written as:

$$T_{ac} = \frac{P_0}{\omega C} \left(1 + \frac{1}{\omega^2 \tau_e^2} + \omega^2 \tau_{ii}^2 + \frac{2K_b}{3K_s} \right)^{-\frac{1}{2}} \quad (2.4)$$

The phase difference between the temperature and power oscillations is given as:

$$\Phi = -\frac{\pi}{2} + \arctan \left(\frac{1}{\omega \tau_e} - \omega \tau_i \right) \quad (2.5)$$

The thermal time constants (relaxation times) for each of the system elements are :

$$\tau_H = \frac{C_H}{K_H}; \quad \tau_S = \frac{C_S}{K_S}; \quad \tau_\theta = \frac{C_\theta}{K_\theta}; \quad \tau_e = \frac{C}{K_b}; \quad \tau_{ii}^2 = \tau_H^2 + \tau_S^2 + \tau_\theta^2 \quad (2.6)$$

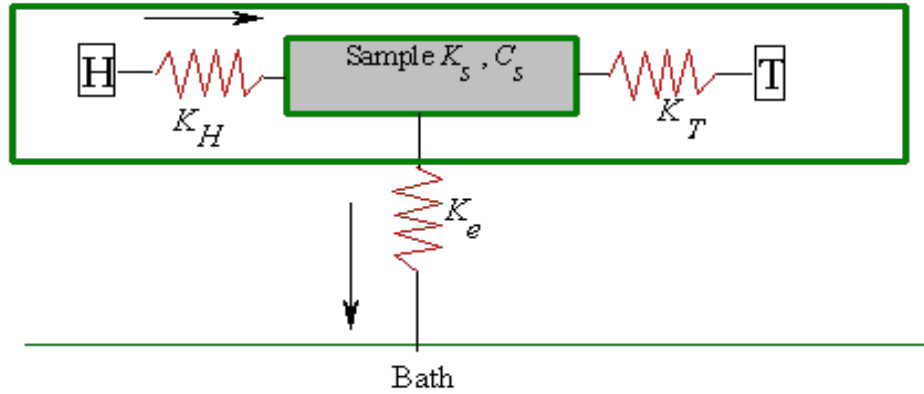


Figure 2.1 Schematic diagram of the one lump thermal model (AC- Calorimetry).

Based on the condition: $\frac{1}{\tau_e} \ll \omega \ll \frac{1}{\tau_i}$, (2.7)

the total heat capacity C will be: $C = \frac{P_0}{\omega T_{ac}} \cong C^*$. (2.8)

For further calculations we will introduce a relative phase shift φ , where,

$$\varphi = \Phi + \frac{\pi}{2} .$$

The fact that the heat capacity is frequency dependent, gives us the option to treat that as a complex number by having a combination of the real, $C'(\omega)$, and imaginary, $C''(\omega)$, parts :

$$C(\omega) = C'(\omega) + iC''(\omega). \quad (2.9)$$

Solving equation (2.4) and taking on consideration that $\tan\varphi = \frac{1}{\omega\tau_e} - \omega\tau_i$, we get:

$$C'(\omega) = \frac{P_0}{\omega T_{ac}} \cos\varphi * f(\omega), \quad (2.10a)$$

$$C''(\omega) = \frac{P_0}{\omega T_{ac}} \sin\varphi * g(\omega) - \frac{K_b}{\omega}, \quad (2.10b)$$

with

$$f(\omega) = \left[1 + \cos^2\varphi \left(\frac{2K_b}{3K_s} + \frac{2\tau_i}{\tau_e} - 2\tau_s\tau_c\omega^2 \right) \right]^{-\frac{1}{2}}, \quad (2.11a)$$

$$g(\omega) = f(\omega) \left[1 + \frac{\omega\tau_i}{\tan\varphi} \right], \quad (2.11b)$$

where, τ_c is the internal thermal relaxation time for the cell, τ_i and τ_e are given from Equations (2.6). If $\tau_i \ll \tau_e$, almost zero internal thermal resistance, both $g(\omega)$ and $f(\omega)$ approach one for all ω . The value of the external thermal resistance ($R_e = 1/K_b$) is typically the same for all samples,

Re \sim 200 K/W. The specific heat capacity C_p is defined as:

$$C_p = \frac{C'(\omega) - C_{empty}}{m_s} = \frac{C^* \cos\varphi f(\omega) - C_{empty}}{m_s}, \quad (2.12)$$

where, m_s is the mass in grams of the sample and C_{empty} is the heat capacity

of the empty cell.

$$C''(\omega) = C^* \sin\phi g(\omega) - \frac{1}{\omega R_e} . \quad (2.13)$$

We measure at the beginning of each experiment the amplitude of the dissipated power, P_0 . Also, experimentally are defined the amplitude of the temperature oscillation T_{ac} and the relative phase shift ϕ . The phase shift contains information about the heat capacity and the internal time constant, which is directly related to the sample's thermal conductivity.

The inequalities in Equation (2.7) help to solve Equations (2.2). Experimentally, a frequency scan determines the frequency range where the heat capacity data are frequency independent. A frequency scan is done by changing the frequency, maintaining the same voltage amplitude of the applied power oscillation to the heater, keeping the bath temperature constant, and measuring the sample temperature oscillation for each frequency. A log-log plot of ωT_{ac} vs. ω gives a frequency independent 'plateau' in some range of frequencies which provides the range of working frequency for the calorimeter. In this range, the heat capacity is frequency independent; neither of the thermal relaxation times play a major role and can be neglected. A typical frequency scan profile and how we fulfill experimentally the requirements of Equations (2.7) is shown elsewhere [20].

2.1.3 Calorimeter design and electronic circuitry

The sample and cell should be thermally isolated from the surroundings and in a temperature-controlled environment. For this purpose, these are placed

inside of a copper block. The temperature of the copper block is controlled by a Lakeshore, model 340 temperature controller. By adjusting Lakeshore's parameters, we can achieve very slow and linear scanning rates varying from 10 mK/hour to 5 K/hour and with noise better than 100 μ K .

The bath's heater bought from Omega Engineering has the dimensions closely matched to that of the bath and it is glued to the outside surface of the copper cylinder. There are two platinum thermometers arranged and placed, one close to the bath's heater (referred to, as the *control PRT*) and the other close to the cell's heater (referred as the *center PRT*). It is placed very close to the cell and the center of the bath cavity, therefore can measure the bath temperature, T_B , next to the cell, with very good accuracy. A copper lid, with a long stainless steel tube in the middle, is mounted on top of the bath. All the wires coming out from the bath go through the copper tube and connect the bath with the other parts of the circuit.

The cell has its own heater attached using GE varnish. A carbon resistor bead (thermistor) is attached on the opposite side of the cell. The leads of heater and thermistor are soldered to posts. The posts themselves are placed at the very end of the stainless steel tube. One side of the posts has the heater's and thermistor's wires soldered permanently and connected to Keithly DMM 2002. A schematic of this design is given elsewhere [19], but the block diagram of the electronic system is given on **Figure 2.1**.

The whole experiment is controlled via a PC and the program that controls the data acquisition and preliminary analysis was written in C++ and compiled under Borland C++. The communication with the instruments is done through a PCI-GPIB interface card from National Instruments, Inc. [6]. The data acquisition program makes possible the splitting of the temperature

control procedure from the data collection one. There is a file that is used to fix the experimental parameters as needed (ini file).

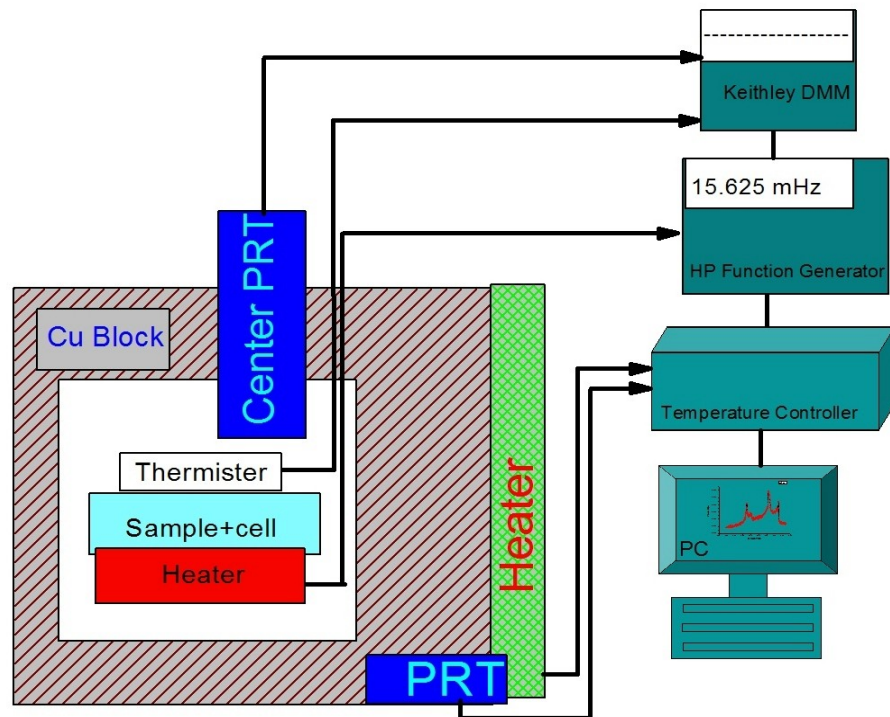


Figure 2.2. AC-calorimeter Block diagram is showing the bath content and all the connections to the instruments [19].

The sample is heated by sending a sinusoidal power through the heater from a Hewlett Packard Function Generator HP 33120 [7]. For more accurate measurements there is another standard resistor, of resistance R_{std} , con-

nected in series with the strain gauge heater and $I_h = I_{std}$. The power dissipated at the heater, P_0 is measured by “digitizing” the voltage across the standard resistor and the heater [8] where,

$$P_0 = I_h V_h = I_{std} V_h = \frac{V_{std}}{R_{std}} V_h, \quad (2.14)$$

The temperature controlling thread starts after the power measurement is over. The data collection starts after the main thread is signaled.

The PRT-s and the carbon flake thermistor work based on the principle that the resistance changes as a function of temperature. That is why the change in their resistance is measured first and then using calibration functions the resistance values are converted into the temperature. The temperature dependence of resistance for PRT can be expressed as,

$$R = R_0(1 + \alpha T + \beta T^2), \quad (2.15)$$

where, R_0 is the resistance at 0°C and α, β are the calibration constants. The bath temperature is calculated as,

$$T_{prt} = \frac{T_b^{prt} + T_a^{prt}}{2}, \quad (2.16)$$

There is a nonlinear relation between the temperature and the resistance of the carbon flake thermistor as,

$$\frac{1}{T} = a_0 + a_1 \log \left(\frac{R}{R_0} \right) + a_2 \left[\log \left(\frac{R}{R_0} \right) \right]^2, \quad (2.17)$$

where, a_0 , a_1 , a_2 are constants and $R_0 = 10^5 \Omega$ for all calculations. Experimentally the resistance wave oscillations are fitted with the function:

$$X = a + bt + ct^2 + A_\omega \sin \omega t + A'_\omega \cos \omega t + A_{2\omega} \sin \omega t + A'_{2\omega} \sin \omega t, \quad (2.18)$$

where, the quadratic part is the background term and the others represent the oscillating term with the voltage frequency ω and the power frequency 2ω . After the fitting the amplitude ΔR and phase φ are found as,

$$\Delta R_\omega = \sqrt{A_\omega^2 + (A'_\omega)^2}, \quad \varphi_\omega = \tan^{-1} \left(\frac{A_\omega}{A'_\omega} \right), \quad (2.19)$$

$$\Delta R_{2\omega} = \sqrt{A_{2\omega}^2 + (A'_{2\omega})^2}, \quad \varphi_{2\omega} = \tan^{-1} \left(\frac{A_{2\omega}}{A'_{2\omega}} \right). \quad (2.20)$$

Based on the above equations and since the amplitude of the oscillations is very small we can find

$$T_{ac} \approx \left| \frac{dT}{dR} \right| \Delta R, \quad (2.21)$$

so, T_{ac} is calculated by

$$T_{ac} = T_{th}^2 \frac{\Delta R}{R_{th}} \left[a_1 + 2a_2 \log \left(\frac{R_{th}}{R_0} \right) \right]. \quad (2.22)$$

2.2 Modulated Differential Scanning Calorimetry

Differential scanning calorimetry (DSC) is a calorimetric method which measure the total heat flow as the sample undergoes a physical transformation such as phase transitions. During the experimental procedure heat will flow to the sample and to the reference, but they both maintain the same temperature. This method does not separate the reversible and nonreversible part.

On the other side Modulated differential scanning calorimetry (MDSC) allows for the simultaneous measurement of both heat flow and heat capacity. MDSC is more complex as a method because a heating ramp is accompanied by a sinusoidal temperature modulation as well. As such, MDSC can simultaneously determine the non-reversible and the reversible heat capacity components. A detailed description of the MDSC method can be found elsewhere [9-15].

MDSC experiments were performed using a Model Q200 from TA Instruments, USA. Temperature calibration was done with a sapphire disc. A temperature oscillation is described as,

$$T = T_0 + q_0 t + A_T \sin \omega t, \quad (2.23)$$

where, T is the temperature at time t , T_0 is the initial temperature at time

$t = 0$, A_T is the temperature amplitude, q_0 is the scan rate and ω ($\omega = 2\pi f$) is the angular frequency of the temperature modulation.

Since, the applied heating rate, q , in MDSC, consists of two components, linear and periodic, the heat flow is also separated. The response to the periodic heating rate is given on Equation (2.25),

$$q = \frac{dT}{dt} = q_0 + A_q \cos(\omega t), \quad (2.24)$$

$$HF_{periodic} = A_{HF} \cos(\omega t - \varphi), \quad (2.25)$$

where, φ is the phase shift between heat flow and heating rate. The data were analyzed correcting φ and the details of the procedure and other estimations are given elsewhere [16]. As a result of all these, the equations of complex specific heat, C_p^* , real C_p' , and imaginary, C_p'' are given respectively as,

$$|C_p^*| = \frac{A_{HF}}{mA_q}, \quad C_p' = |C_p^*| \cos\phi, \quad C_p'' = |C_p^*| \sin\phi, \quad (2.26)$$

where, m is the mass of a sample and ϕ the corrected phase angle. Further experimental details are given on each upcoming chapter, where MDSC has been applied.

2.3 Dielectric Spectrometer Design and Operation

In the first chapter, a general description of dielectric spectroscopy was given and its application for biomaterials. This paragraph shows in a more specific way, how the dielectric spectrometer works and provides the design of the one used to collect the data. Using the dielectric spectrometer, the schematic of which is shown on **Figure 2.3**, we can determine the real $\varepsilon'(\omega)$ and the imaginary $\varepsilon''(\omega)$ part of the complex dielectric constant ε^* .

Our experimental data show the profile of the dielectric constant as a function of temperature for a constant frequency and voltage amplitude. In some of our measurements it is needed the sample's frequency spectra sample. In this case the dielectric constant is measured as the frequency is changed, while the temperature and the voltage applied across the capacitive cell are held constant. The capacitive cell consists of a parallel-plate configuration, placed in a temperature-controlled bath.

The experiment begins by balancing the ac-bridge at a starting frequency. The needed (temperature, frequency) scan is performed from this point. A digital lock-in amplifier can detect the off-balance in phase and out of phase signals [18]. A multiplicative conversion factor will convert the off-balance signal to the equivalent change in capacitance. The dielectric constant can be defined as the filled cell's capacitance divided by the empty's one. The specific parameters used during our experimental work are given in Chapters 2 and 3.

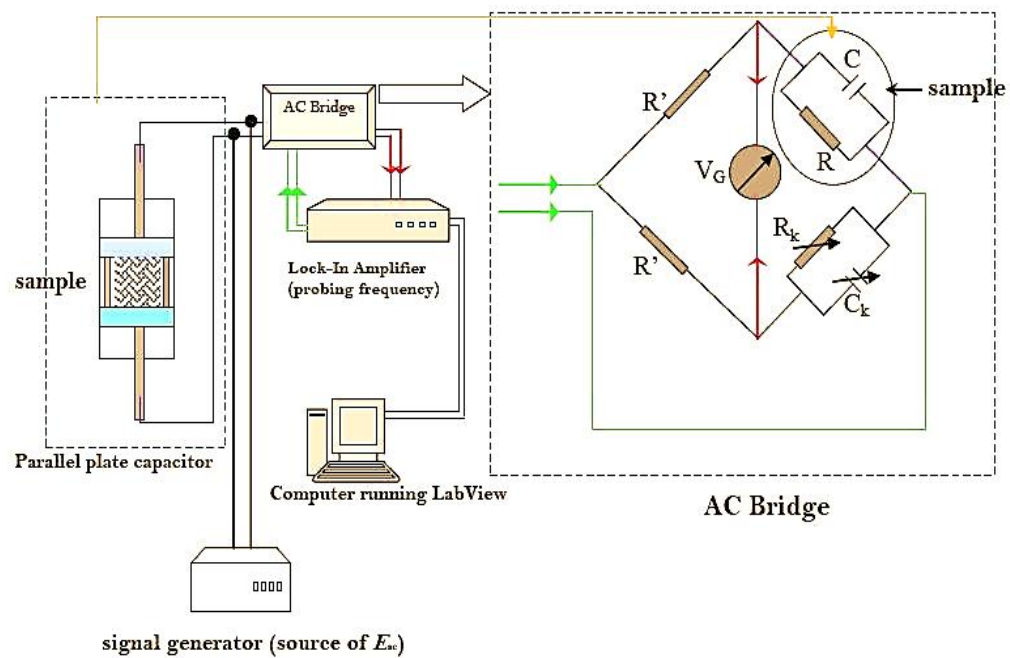


Figure 2.3. Schematic of an AC-capacitance bridge dielectric spectrometer [17].

References

- [1] J. Thoen, H. Marynissen, and G. M. Mochel, *Phys. Rev. A*, **26**, 2886 (1982).
- [2] Y.P. Feng, A. Jin, D. Finotello, K. Gillis, and M. Chan, *Phys. Rev. B*, **38**, 7041 (1998).
- [3] T. Kenny and P.L. Richard, *Rev. Sci. Instrum.*, **61**, 822 (1990).
- [4] P. F. Sullivan and G. Seidel, *Phys. Rev.*, **173**, 679 (1968).
- [6] R. Saito, M.S. Dresselhaus, and G. Dresselhaus, *Physical properties of carbon nanotubes. Imperial College Press, London*, (1998).
- [7] Agilent Technologies, Inc., <http://www.agilent.com>.
- [8] The DMM is set to do a specified number of measurements at equally spaced time intervals. For each measurement the time elapsed and the measured value get stored in the internal memory. After the specified number of measurements is carried out, the data are then downloaded at the computer. The digitizing gets triggered by the TTL trigger of the HP, which happens at every zero crossing of the voltage.
- [9] J.E.K. Schawe, *Thermochim. Acta*, **271**, 127 (1996).
- [10] N. J. Coleman and D.Q.M. Craig, *Int. J. Pharmaceu.*, **135**, 13 (1996).
- [11] J.E.K. Schawe, *Thermochim. Acta*, **261**, 183(1995).
- [12] J.M. Hutchinson and S. Montserrat, *J. Therm. Anal.*, **47**, 103 (1996).
- [13] A. Hensel, J. Dobbertin, A. Boller and J.E.K. Schawe, *J. Therm. Anal.*, **46**, 935 (1996).
- [14] B. Wunderlich, *J. Therm. Anal.*, **48**, 207 (1997).

- [15] S.R. Aubuchon and P.S. Gill, *J. Therm. Anal.*, **49**, 103 (1997).
- [16] S. Weyer, A. Hensel, and C. Schick, *Thermochim. Acta*, **304/305**, 267 (1997).
- [17] R. Basu, *Ph.D. dissertation*, WPI, 2010.
- [18] Standford Research Systems, <http://www.thinksrs.com>.
- [19] K.P. Sigdel, *Ph.D. dissertation*, WPI, 2011.
- [20] A. Roshi, *Ph.D. dissertation*, WPI, 2005.

CHAPTER 3

LC-PHASE ORDERING OF SHORT DNA FRAGMENTS IN AQUEOUS SOLUTION

Abstract

DNA found in an aqueous environment represents an interesting biological system of study. Dilution effect has been considered an important form of disorder since it can weaken macromolecular interactions responsible for phase ordering. We believe that the experimental work presented in this chapter helps in understanding the intermolecular interactions and the self-orienting of DNA short fragments (less than 13-base pairs). High resolution AC-calorimetry used here makes possible to observe very small energy excitations of the system and probe more transition features not present in literature so far. MDSC method shows simultaneously the effect of temperature and concentration on T_m , which goes toward higher temperatures for high concentration. There is no such an effect, as the modulation frequency is increased. The dielectric spectra for the low frequency regime (0.1-100 kHz)

show two well-defined modes as an evidence of elongated structural dipole orientation (first mode) and of the induced dipoles within the multiple DNA structural self-oriented layers (second mode). The new proposed phase diagram concludes all structural evolution under the effect of physical factors described here.

3.1 Introduction

One of the most challenging goals of science is to account for the wonderful complexity and variety of the biological world in terms of general and simple laws. Referring to notions from statistical and soft-matter physics has provided remarkable successes in understanding biological mechanisms. Disordered systems, such as biological systems, often display complex and rich phenomena, being the generalization of the ideal systems. Disorder can dramatically alter the physical properties of multi-component systems. An interesting system of study is diluted deoxyribonucleic acid (DNA) in an aqueous environment. Dilution effects present an important form of disorder, which imposes instead the random breaking or weakening of intermolecular bonds or interactions responsible for phase ordering [1].

Studying the dilution effects in a controlled manner on good model physical systems, such as dilute DNA solutions, offers a unique probe. An exciting challenge is thus to find self-assembly properties that drive the spontaneous ordering of biological macromolecules, and to control mimic natural assembly for materials design. Examples of such molecular ordering range from folded proteins to cellular organization. Such complexity can be

reduced to the relative simplicity of self-assembled structures, driven by packing constraints and enforced by van der Waals, hydrophobic and, electrostatic interactions (see Chapter 1).

In 1949, Onsager explored theoretically different ways of inducing orientational alignment of elongated particles in solution [2]. Spontaneous, entropy-driven mechanisms such as orientational and positional order, well characterized in colloids, liquid crystals and polymers, are being increasingly recognized as also playing an important role in many biological systems.

One of the major challenges in biophysics is understanding how the physical properties of macromolecules affect their interactions and their self-ordering. Since most of the biological molecules are chiral, it is crucial to know how the molecular chirality effects the steps from single molecule to supramolecular assemblies, such as ordered phases or aggregation [3, 4]. Molecular crowding of cellular interior is known to play role in the spontaneous organization of biological macromolecules. Several biochemical and physiological processes are found to be influenced by strong packing. Also, complex ordered arrangements such as liquid – crystalline mesophases, have been shown to arise from highly packed biomolecules. Of particular interest is the ordering of highly concentrated DNA (aqueous solution with over 60% of DNA content), which can lead to a variety of mesophases *in vivo* [5].

DNA, one of the most interesting and important polymer, self-organizes into compact structures under certain physical and chemical conditions. This condensation process *in vivo* is common inside the cell nuclei. The condensed states of DNA are not inactive states and experiments have shown that condensation of DNA increases its activity in replication, recombination and transcription [6, 7]. The early studies of DNA liquid crys-

talline phases played a crucial role in deciphering its structure and also enabling alignment of the DNA chains [8].

In 1993, Leforestier studied aqueous solutions of 146-base pair DNA fragments using polarizing and electron microscopy. Here, these two experimental methods complemented each other and provided information about the local and long-range ordering. The results show that DNA behave as a liquid crystal viscous solution in which molecules are ordered, while keeping their ability to slide with respect to each other [9].

At low concentration (dilute solutions less than 1 $\mu\text{g/ml}$), the DNA molecules are randomly oriented and the solution is a classical isotropic liquid [31]. As the concentration increases, molecules order in the liquid that transforms into a liquid crystal of the "cholesteric" type and turns itself into a "columnar hexagonal" phase for higher concentrations. The cholesteric phase is observed at room temperature in the concentration range of 160 to about 290 mg/ml [9, 10]. It may coexist with the isotropic phase or with the more concentrated columnar hexagonal phase depending on DNA concentration and the supporting electrolyte solution. In the cholesteric phase, molecules are aligned in parallel, and their orientation rotates continuously along a direction which is called the cholesteric axis.

Similar organizations can be found in vivo: a cholesteric organization of DNA was described in dinoflagellate chromosomes and in certain bacterial nucleoides, and a hexagonal packing of DNA molecules was found in bacteriophages [10].

Different optical, x-ray and magnetic resonance methods have mainly studied the self-assembly of long duplexes B-form DNA arranging from mega-base pair (bp) down to 100 bp (~50 nm in length). These studies have

revealed an isotropic phase (I); chiral nematic (N), uniaxial columnar (CU), and higher-ordered columnar (C2) liquid crystal phases and crystal (X) phases, with increasing DNA concentration (**Figure 3.1**) [11, 12, 13, 14]. Nakata in 2007, was surprised to find nematic LC ordering formed by 6-20 bp DNA oligomers. Their structural studies found that short B-form DNA oligomers exhibit nematic and columnar liquid crystal phases and these phases are produced by the end-to-end adhesion and consequent stacking of the duplex oligomers into polydisperse anisotropic rod-shaped aggregates, which can then order as liquid crystals. The observation of the nematic and columnar LC phases provides clear evidence for end-to-end stacking of the sDNA into rod-shaped aggregates (**Figure 3.2**).

Nano-length B-DNA duplexes have been idealized as hydrophilic cylinders with hydrophobic ends capable of end-to-end adhesion and stacking into units sufficiently anisotropic to orientationally and positionally order into LC phases. The textures of the sDNA observed under polarizing microscope show that the N phase is formed at lower concentration and the Cu phase at higher concentration. These phases are observed for temperatures less than melting temperature ($T_{LC} < T_m$). This sort of assembly is typical in crystalline sDNA and in sDNA/protein complexes [15, 16, 17, 18].

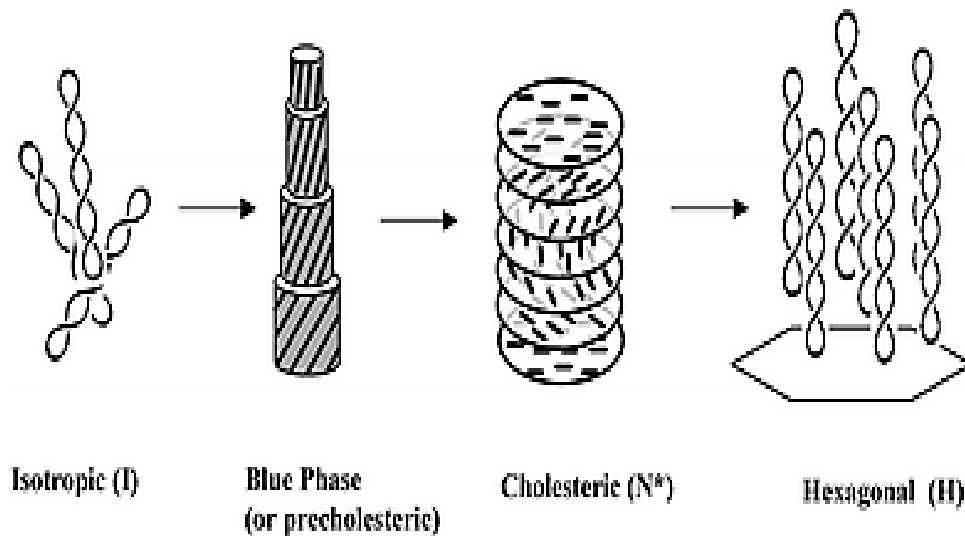


Figure 3.1. *DNA liquid crystal phase evolution as a function of structure concentration [30].*

Further investigation [19, 20] of these DNA condensate phases have shown that this end-to-end stacking of short DNA strands is facilitated by base stacking of hydrophobic ends, suggesting a biological origin for these forces. Small angle x-ray scattering (SAXS) experiments have also revealed that the end-to-end interaction is an attractive short range force and weakly dependent on the ion concentration. Repulsion forces have been reported when short (20 bp) dumb-bell DNA solutions were analyzed. The attraction

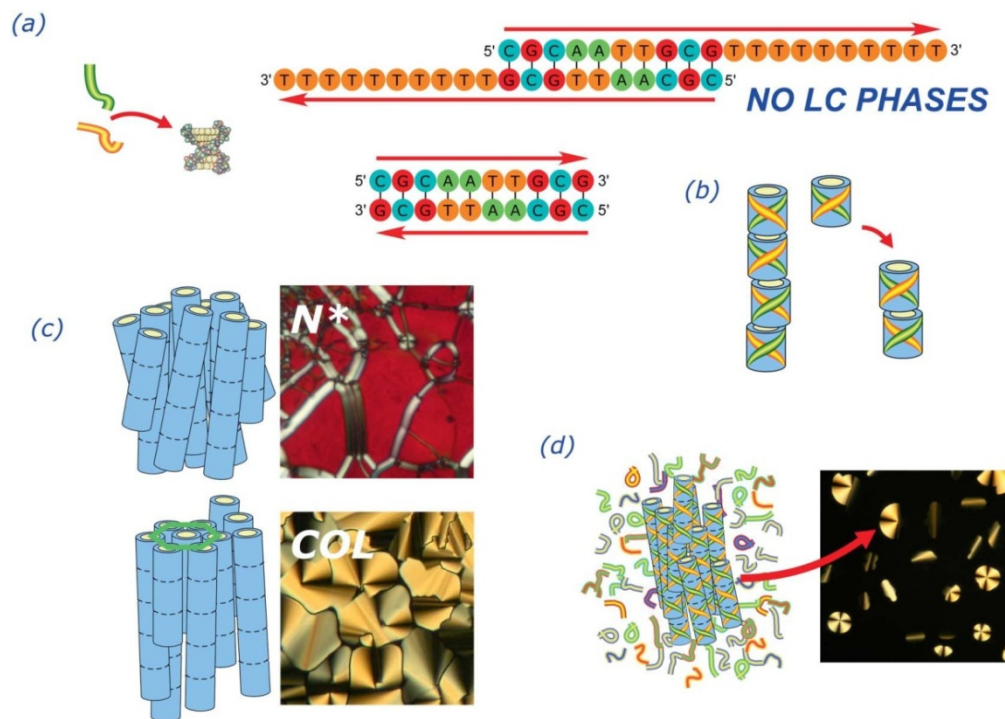


Figure 3.2. Sketch of the self-assembly process leading to the LC alignment of well-paired short DNA duplexes. (a) Complementary and partially complementary sequences pair into helices. (b) Units orientationally and positionally ordered into LC phases (c), chiral nematic N^* and hexagonal columnar COL. (d) Upon cooling a mixture of single-stranded molecules [29].

between dsDNA molecules is stronger than that between semi-dumb-bell (hairpin) DNA molecules under the same ionic conditions. This is maybe an indicator that the stacking effect is suppressed by the loops capping both ends of DNA.

Here, we report the structural and self-organizing effects driven by physical changes (i.e, temperature and applied electric field) on diluted short

double strands (dsDNA), hairpin DNA, and single-strand (ssDNA) mixtures. Calorimetry (both AC and MDSC), as well as low-frequency (0.1 to 100 kHz) isothermal dielectric measurements have been performed on solutions of DNA fragments as a function of concentration. Custom DNA structures were obtained with 13-base unit length and samples made in solution at various concentration. Results show a reproducible heat capacity C_p signature on heating and cooling scans. The AC C_p peak vanishes and new features are revealed as the temperature scan rate is lowered to 0.017 K/min. The observed real, ϵ' , and imaginary, ϵ'' , permittivity of the suspended DNA show features indicating low-frequency dynamics that in turn suggests large-scale ordering or agglomeration of the DNA short fragments. Based on our observations and in order to summarize our results, we propose a phase diagram, that shows the evolution of DNA structures associated with liquid crystal like transition phases.

3.2 Experimental

3.2.1 Materials and sample preparation

The DNA used for this experiment was purchased from IDT (Integration DNA Technologies) in powder form and was kept that way in the freezer at (-20 °C). The sequence of the ordered DNA was (5'- CGCGAATTCGCGT -3') and suspended in IDTE buffer solution (pH = 8.0) at room temperature (27 °C). The target amount of DNA and IDTE buffer solution were mixed in

a vial. The mixture was then mechanically mixed further in a touch mixture for about two minutes. In general, the prepared solution (DNA+buffer) will contain over 50% double strands, while the rest of the base associations will be hairpins and single strands, which can randomly associate (**Figure 3.3**). We are not able to provide any further detail about the distribution of each possible combination found in our samples.

Different samples having weight fractions ϕ_w ranging from 0.10 to 0.70 were prepared using the same procedure were,

$$\phi_w = m_{DNA} / (m_{DNA} + m_{IDTE})$$

is the weight fraction of DNA and m_{DNA} and m_{IDTE} are the weight of DNA and buffer solution, respectively. After the sample was prepared, it was introduced into a cup + lid type silver cell of volume $V_1 = \pi r^2 l \approx \pi \times 7^2 \times 1.5$ and $V_2 \approx \pi \times 3^2 \times 2 \text{ mm}^3$, for the AC-Calorimetry and MDSC methods respectively.

The DNA solution samples were prepared in the same way for the dielectric spectroscopic studies. The mixture was filled into an Instec (homogeneous alignment) LC cell ($5 \times 5 \text{ mm}^2$ indium tin oxide (ITO) coated area and having $20 \text{ }\mu\text{m}$ spacing) and contained $\sim 1 \text{ mg}$ of sample. Other cell details are given on Chapter 2. The Instec cell was mounted through soldered wires into the AC-Capacitive Bridge. To avoid water evaporation of the sample, the experiment was performed immediately after the sample was introduced into the cell and it lasted for no more than 15 minutes at room temperature. There were done about 5 scans for each concentration and all of them have shown reproducibility. Baseline dielectric values taken repeatedly throughout the experiment indicate that the measurements were stable and reproducible.

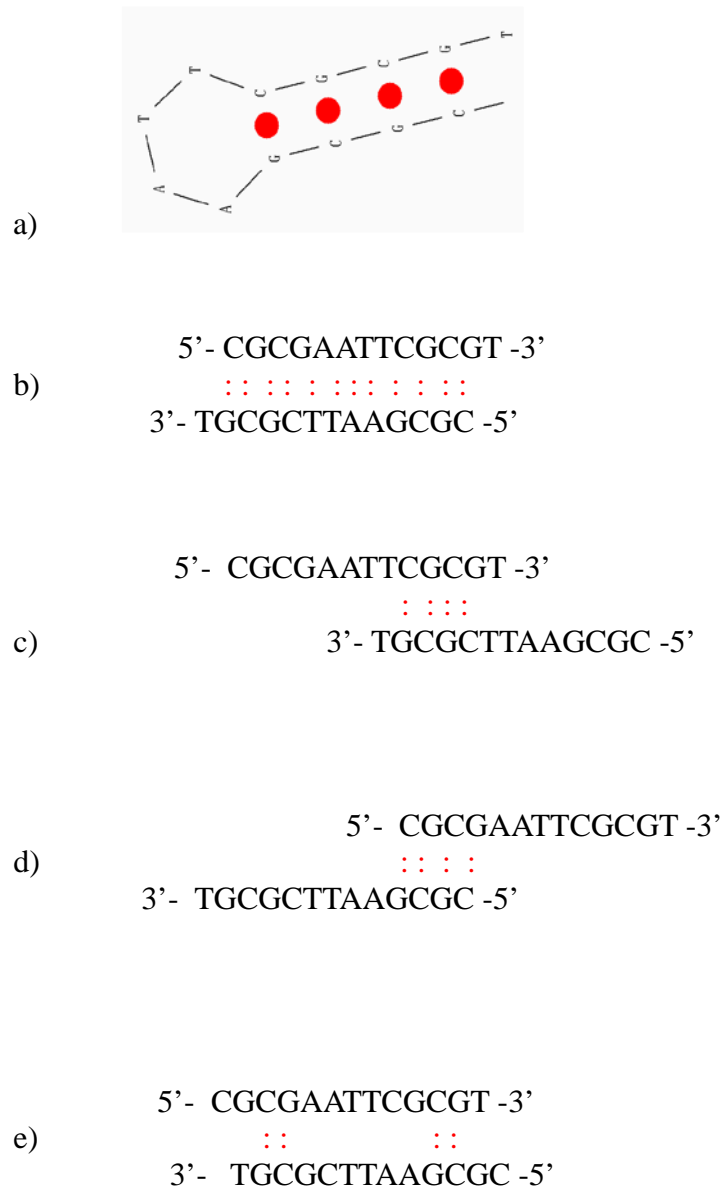


Figure 3.3. Possible structures/base pair combinations of the nucleotide sequence studied. Bases are held together by H-bonds (red dot), where a) is the hairpin structure and b) – a) are possible configurations.

3.2.2 AC- calorimetry

High-resolution AC-Calorimetry measurements were carried out on a home-made calorimeter in the Order-Disorder Phenomena Lab at WPI. The oscillating voltage applied to the cell + sample through the heater (a 120 Ω strain gauge heater attached to the bottom of the cell) will result in temperature oscillations of the sample with amplitude T_{ac} (a 1 M Ω carbon thermistor was attached on the top of the cell). There is a relative phase shift between the applied power $P_{ac} \exp(i\omega t)$ and the detected sample temperature oscillations, $\varphi = \Phi + \pi/2$, where Φ is the absolute phase shift, and φ can provide information about the order of the phase transition (Chapter 2).

During these experiments, the heat capacity was probed as a function of temperature. The oscillation frequency for this experimental part was set at 40 MHz and the applied voltage had the amplitude $V_0 = 0.3$ V. The induced temperature oscillations of the sample resulted $T_{ac} = 0.08$ K. The samples were first loaded at room temperature, and after the thermal equilibrium was reached, were first heated and then cooled at a scan rate of ± 0.017 K/min. There were done about 10 scans for each concentration and all of them have shown reproducibility unless the cell leakage was present. All the cooling DNA thermal profiles overlaid well with the heating ones, showing this way a reproducibility of the experimental results.

The excess heat capacity ΔC associated with a phase transition can be determined by subtracting an appropriate background C^{BG} from the total heat capacity C over a wide temperature range:

$$\Delta C = C - C^{BG} \quad (3.3)$$

The enthalpy change associated with a phase transition is given by

$$\delta H = \int \Delta C dT \quad (3.4)$$

As a result of Equation (3.4), the integration of the imaginary part of the heat capacity will give a measure of the dispersion energy of the sample. In AC-calorimetry technique the uncertainty determining the enthalpy is approximately 10% due to the uncertainty in the background subtraction. The absolute accuracy of the measured heat capacity is about 1 – 10%,

3.2.3 Modulated differential scanning calorimetry (MDSC)

Differential scanning calorimetry (DSC) involves heating and cooling the sample of interest at a constant rate. The MDSC measurements were done using a TA Instruments Q200. This calorimeter is a thermal analysis instrument that determines the temperature and heat flow associated with material transitions as a function of time and temperature. When used in the MDSC mode, a constant heating rate, similar to the one used in conventional DSC mode, is modulated by superimposing upon it a periodic temperature modulation of certain amplitude. This result in a simultaneous introduction of two different time scales in the experiment: a long time scale corresponding to the underlying heating rate, and a shorter time scale corresponding to the period of the modulation [21, 22]. More details of the instrument and the parameters used during our experimental procedures are also given in Chapter 2.

After preparing the sample using the steps given in 3.2.1 section, we place it inside of the hermetic DSC aluminum pan. Hermetic pans are normally used for applications like studies of volatile liquids including specific heat or studies of aqueous solutions above 100 °C. The mass of the sample was usually between 1-20 mg, which must be determined prior to the start of

the experiment. Care was taken to ensure no sample leakage occurred prior to loading into the instrument. Pans are then crimped closed using Blue DSC sample press from TA Instruments [22]. Temperature scans were done for different samples by changing on of the parameters, either the temperature scan rate or the protein concentration of the sample. For each of them were performed at least 5 experimental runs. The experimental steps (heating/cooling run) on DSC or MDSC mode can be edited in the procedure list provided by the company software and most of these steps are done automatically. In order to perform the necessary data analysis we have used TA Analysis software.

Special software is normally used to calculate the C_p . In a MDSC experiment, modulation of the sample temperature permits the heat flow to be split into two components, one of which is dependent upon sample C_p and changes in C_p . With a properly calibrated system, the measurement of C_p by MDSC is more accurate than the three run method, with values of 2-3 % being easily obtained [22].

3.2.4 AC- capacitive dielectric spectrometry

The dielectric constant measurements, as a function of frequency, were performed using an ac-capacitance bridge technique [23, 24, 25]. Capacitance measurement is one way to get dielectric constant. The experiment begins by balancing the ac-bridge at a reference frequency of 0.01 kHz. A frequency scan is then performed from this point recording the off-balance 'in-phase' and 'out-of-phase' signals acquired by a digital lock-in amplifier (*Stanford Research Systems SR830 DSP*). An empty and filled cell capacitance are measured to determine the dielectric constant ϵ . The experimental results

show real $\epsilon'(\omega)$ and imaginary $\epsilon''(\omega)$ part of the complex dielectric constant as a function of frequency (0.01–100 kHz) at room temperature. The actual magnitude of the applied electric field across the sample is not precisely known, but the driving voltage can be controlled. For this set of experiments the voltage value was fixed at a low $V = 0.03$ V in order to not induce any polarization effects. (See Chapter 2). To avoid water evaporation of the sample, the experiment was performed immediately after the sample was introduced into the cell and it lasted for no more than 15 minutes at room temperature. There were done about 5 scans for each concentration and all of them have shown reproducibility. Baseline dielectric values taken repeatedly throughout the experiment indicate that the measurements were stable and reproducible. Since, the dielectric constant is calculated from the lock-in amplifier readings directly, the dielectric constant has a 5% error (the same as the manufacturer has provided for the apparatus). There might be a negligible error added from the cell thickness as well.

3.3 Results

A sample having ($\varphi_w = 0.3$) was used for the ACC experiments and was prepared and treated the same way as it is given in section 3.2.1. Often the cell leaked during the experiment and so, a fresh new cell+sample reloaded and the experiment was repeated from the beginning until a complete scan was obtained. **Figure 3.4** shows a reproducible heat/cool temperature scan (± 0.017 K/min) at an oscillation frequency with 40 mHz and an estimated

$T_{AC} \cong 0.08$ K. The complex heat capacity profile, shown here, does reveal any features connected to mesophase ordering or melting temperature. However, the scans what appear to be small “wings” or strong temperature dependence suggesting that some feature below 300 and above 356 K exists.

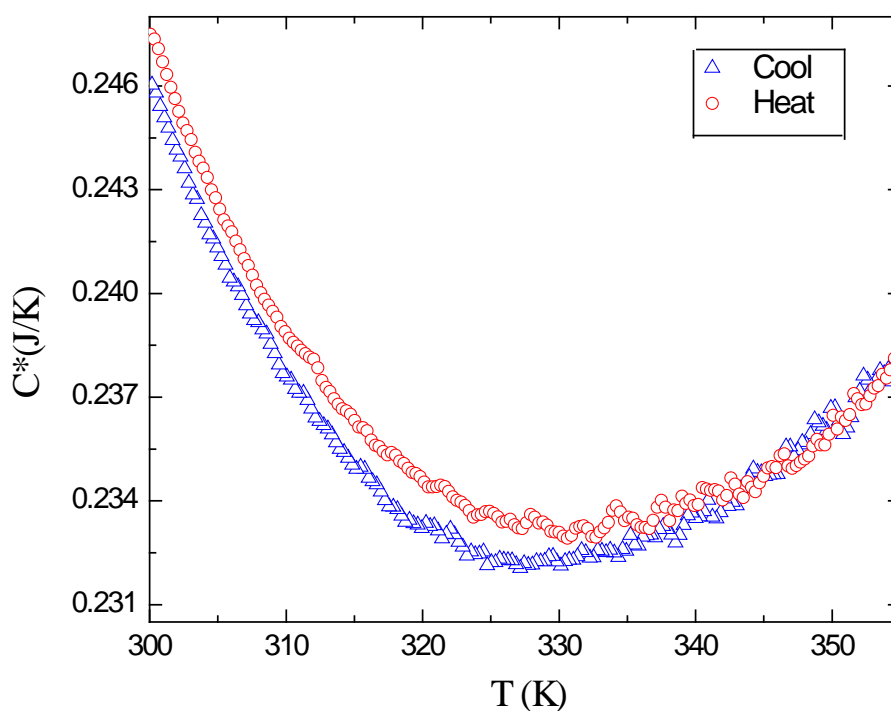


Figure 3.4. Wide-temperature scans at ± 0.017 K/min of the heat capacity amplitude on heating (circles) and cooling (triangles) of a fresh DNA sample ($\phi_w = 0.3$), show a reproducible heat/cool thermal behavior at an oscillation frequency with 40 mHz and an estimated $T_{AC} \cong 0.08$ K.

The fact that both heating (circles) and cooling (triangles) graphs overlay each other demonstrates that no sample leakage occurred. This is a very important observation, because leakage would have caused the evaporation of water and will cause the total mass to decrease (and so C^*) as well as φ_w to increase. The fact that increasing the DNA concentration in the solution will self-organize the DNA fragments into LC like phases, motivate us to take further steps for studying these transitions. We continued to increase φ_w to 0.6 and let the calorimeter run to higher temperatures as it is shown in **Figure 3.5**. The nature of the wing of ΔC does not change below 320 K, but structural mesophases and disassociations of the base pairs are probed on the 325 – 355 K range. The heat capacity (real and imaginary) features are shifted further to higher temperatures as the result of the high DNA concentration φ_w and very slow heating rate. The most evident feature is the small peak at 349 K.

Based on these experimental results we cannot determine the “melting” temperature T_m of the DNA associated bases. The graph has more than one transition step and none of those is similar to the traditional “melting” peak that the DSC data will show further on this paragraph. There exist no cooling data (we have not performed a cooling run) for making sure that no leakage was present, especially below 320 K, where a sharp drop is present in C' and C'' .

Because of the long experiment scans and large parameter space to be explored, faster scans were performed using the MDSC technique. The sample preparation and treatment is the same as ACC method. The MDSC mode gives access to the reversible (Real) and nonreversible (Imaginary) part of the heat capacity. **Figure 3.6** shows the evolution of the (real) $RevC_p$ as a

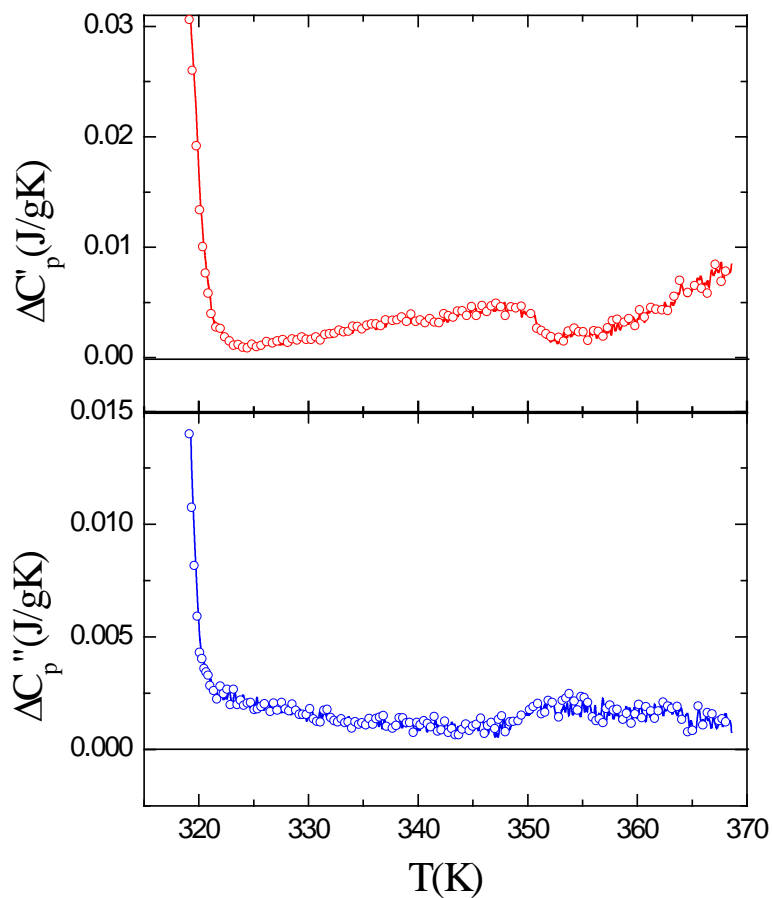


Figure 3.5. *Top panel – Real excess specific heat. Bottom panel – Imaginary specific heat. Temperature scan using AC-calorimetry of 60 wt% ($\phi_w = 0.6$) DNA at 0.017 K/min over the temperature range 320 to 370 K. Structural mesophases and disassociations of the base pairs are probed on the 325 – 355 K range. The most evident feature is the small peak at 349 K.*

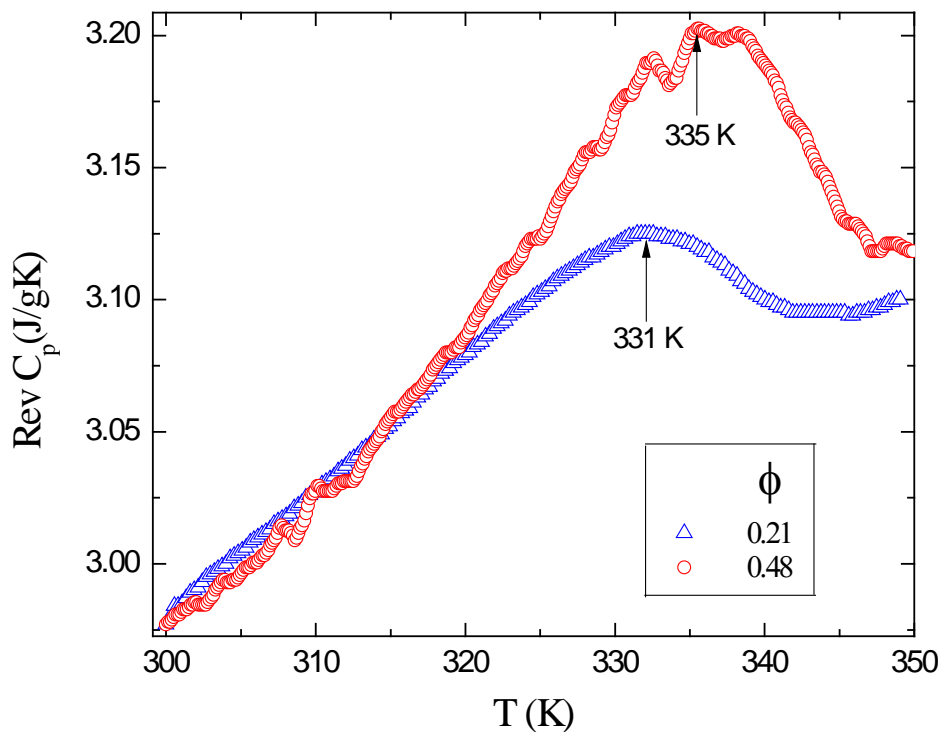


Figure 3.6. Reversible (real) heat capacity as a function of temperature for different concentration (DNA+IDTE) at +1 K/min using the MDSC. Blue triangles are results for the $\phi_w = 0.21$ sample and red circles for the $\phi_w = 0.48$ sample. These small changes of reversible heat capacity values represent the evolution of the energetics of the DNA structural transition mainly for temperatures less than 335 K, before the “melting” (strand separation) takes place. The DNA “melting temperature” (the peak maximum) is shifted ~ 5 K toward the highest temperatures for high ϕ_w .

function of T for two φ_w at +1 K/min, approximately 60 times faster than the scan rate used by ACC.

The experiments in general last only a couple of hours for heating and cooling and this reduces the chance of the cell rupturing due to the buildup of vapor pressure of water. The disadvantage of this method is the fact that most of the phase transitions that exhibit slow kinetics will not be present in our experimental results.

Reversible heat capacity of $\varphi_w = 0.21$ (blue triangles) shows a much smoother line compare to that of $\varphi_w = 0.48$ (red circles) even though the scan rate stays the same, at 1 K/min. Since, φ_w is increased more than twice, some small changes of reversible heat capacity values will be likely present. These changes represent the evolution of the energetics of the DNA structural transition mainly for temperatures less than 335 K. This is evidence that most of the DNA structural orientation and self-organizing happen before the “melting” (strand separation) takes place. The DNA “melting temperature” (the peak maximum) is shifted ~ 5 K toward the highest temperatures for high φ_w . These observations are consistent with literature [26, 27].

Another important study involving the kinetics of phase transitions is shown in **Figure 3.7**. The Reversible heat capacity graphs overlay at 1 K/min (blue triangles) and 2 K/min (green circles) temperature scan rates. The “melting” transition is shifted about 2 degrees lower in temperature. This is seen only at 0.22 K/min (red squares). In addition, a small step, clear evidence of some energy release, is present only on the lowest scan rate thermal profile. This figure support the idea that very low temperature scan rates can probe even the slowest kinetics of phase transition in the structures present in the sample. The enthalpy changes ΔH for these graphs (area under each

peak) are slightly deferent. The differences are within the error made as we try to select the borders for each graph. The calculations then, were done by using the TA Analyses software. The average enthalpy, $\Delta H \sim 115$ J/g was calculated for the graphs found in **Figure 3.7**.

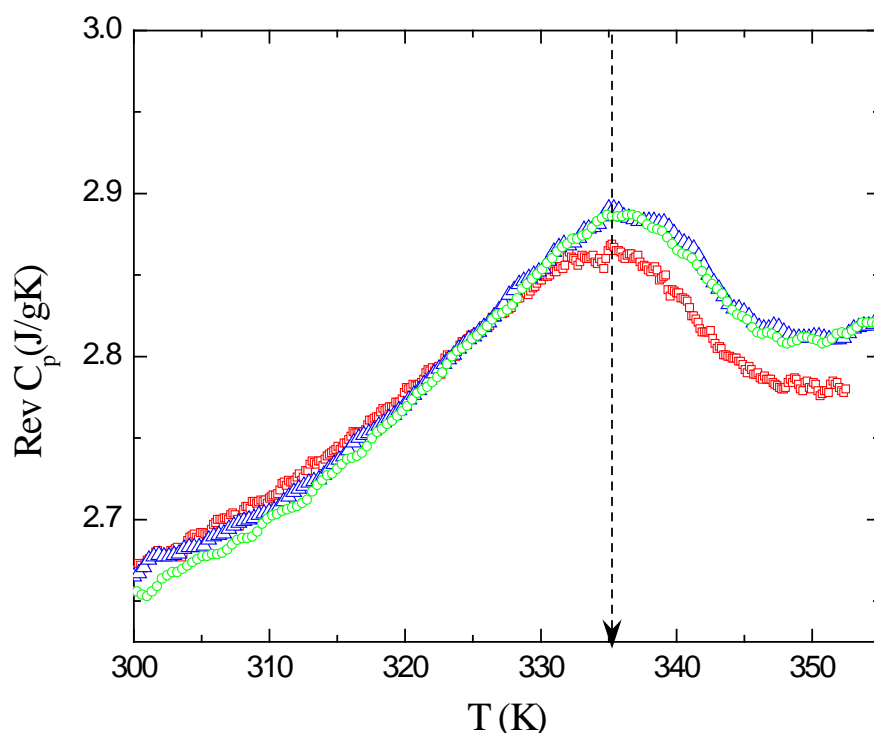


Figure 3.7. Reversible (real) heat capacity as a function of temperature for different temperature scan rates on the same (DNA+IDTE) concentration, $\phi_w = 0.3$. Blue triangles show the MDSC profile for 1 K/min, green circles for 2 K/min and red squares for 0.22 K/min (a small step, clear evidence of some energy release is present only for this heating rate). The vertical dashed arrow indicates the “melting” of the DNA structure at about 335 K.

Further experiments were performed on diluted DNA structures by using AC-capacitive bridge technique as, it is given in section 3.2.4. The dielectric spectra of these diluted structures, with different DNA concentration $\varphi_w = 0.60$ (green squares), $\varphi_w = 0.30$ (blue triangles) and buffer $\varphi_w = 0.00$ (red filled circles) is given in **Figure 3.8**. The buffer solution does not show any orientation mode as it is expected. The dielectric constant of diluted DNA structures exhibits a single, well-defined mode, for all concentrations at low frequencies. This mode is likely due to orientation, polarization of permanent and/or induced dipoles either of the DNA structures themselves or within the multiple DNA structural self-oriented layers. Here, the relaxation frequency increases while the strength (peak height of ε'') decreases as φ_w increases. In addition, for $\varphi_w = 0.3$ another mode with different character is shown at frequencies greater than 3.16 kHz. The fact, that there were present less self-oriented DNA structures (low concentrations), maybe allowed the buildup of space-charges within the sample/cell at high frequencies, up to 10^5 Hz. This second mode is evident at the circled region (**Figure 3.9**) were Cole-Cole plots of $\varepsilon''(\omega)$ versus $\varepsilon'(\omega)$ for both concentrations are shown. It is important to note that the direction of increasing frequency is toward the 0 of $\varepsilon''(\omega)$ axis. These graphs are another evidence of the DNA modes involved in self-orienting/self-organizing under the applied electric field.

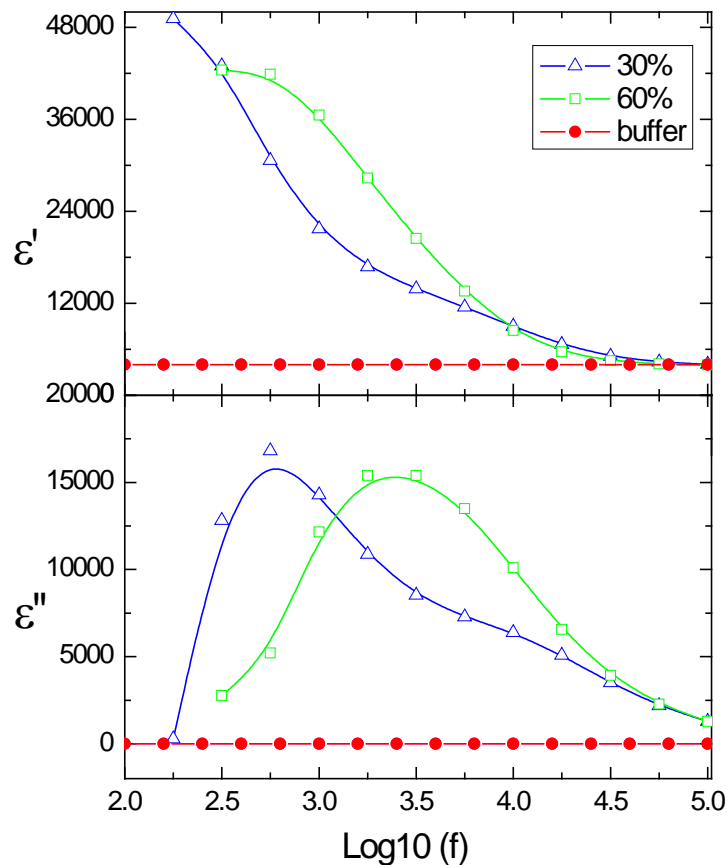


Figure 3.8. Dielectric constant by AC-capacitive bridge technique. Frequency scans of DNA+IDTE for different DNA concentrations $\varphi = 0.6$ (green squares), $\varphi = 0.6$ (blue triangles) and buffer (red filled circles). Top panel – Real part and Bottom panel – Imaginary part. Here, the relaxation frequency increases while the strength (peak height of ϵ'') decreases as φ_w increases. In addition to the first mode, for $\varphi_w = 0.3$, another mode with different character is shown at frequencies greater than 3.16 kHz.

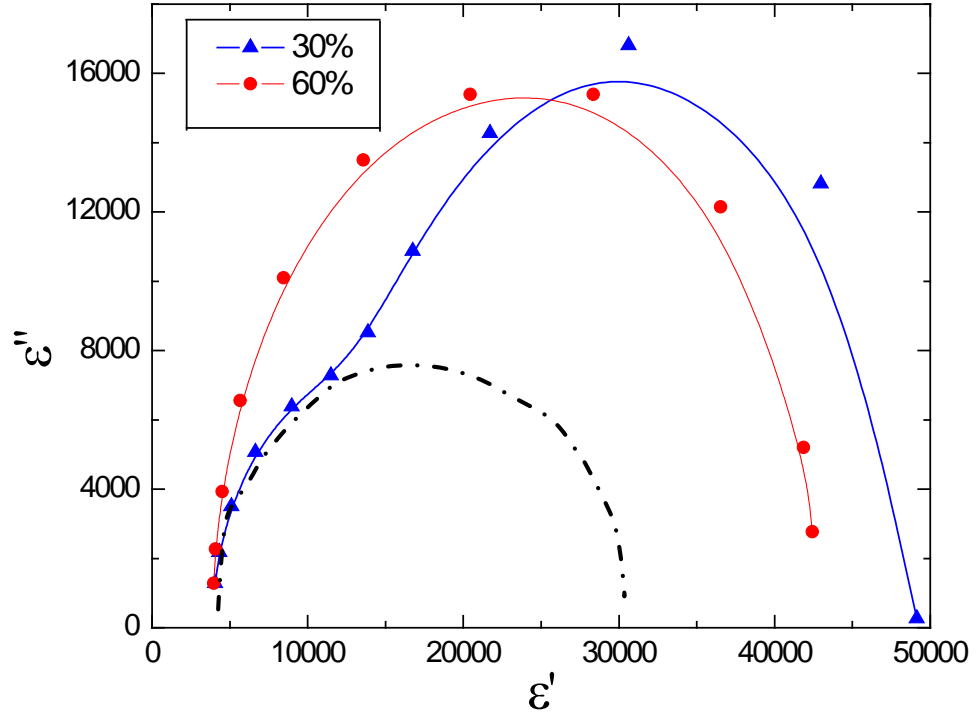


Figure 3.9. Cole-Cole plots of imaginary part $\epsilon''(\omega)$ versus real part $\epsilon'(\omega)$ for different DNA concentrations, $\varphi_w = 0.3$ (blue filled triangles) and $\varphi_w = 0.6$ (red filled circles). Note that the direction of increasing frequency is toward the 0 of $\epsilon'(\omega)$ axis. The dash-dot line indicates the expected Cole-Cole behavior for one of the modes.

3.4 Discussion and Conclusions

We have performed a full analysis of the kinetics and dynamics involved on self-organized DNA structures found in aqueous environment. Through these experimental results, we are trying to highlight the existing models about self-assembling/self-orientation of macromolecules. Some of the existing models are based on a mean field theory of the phase behavior of rigid rod-shaped polymers (mixed solutions rigid rod-shaped polymers). It was found $N-I$ phase coexistence of the rigid like molecules into the N and the flexible ones preferably into the I phase [20, 10, 13, 28]. These intermediate states, predicted to be short lived, were also unobservable at the available temporal resolution (DSC). High resolution AC-calorimetry used here makes possible to observe very small energy excitations of the system. Moreover, our data show how a very low temperature scan rate can add more transition features to the heat capacity profile of the system. This macromolecular segregation was known to complete in the high concentration range applicable to our nDNA solutions. Our further calorimetric study concludes that DNA+IDTE thermal profiles reveal mostly a single feature at ~ 335 K for high temperature scan rates which is believed to be the melting temperature of the system T_m . In addition, T_m it is not dependent of the modulation frequency used for MDSC mode. Cooling temperature scans of all ranges, performed immediately after the heating on the same sample (DNA+buffer) yields reproducible results. There was shown no modulation frequency dependence of T_m .

Knowing the fact, that DNA condensation could have multiple stages very sensitive to the structure concentration and DNA liquid crystalline phas-

es are also dependent on polymer concentration [19, 20, 29], we have performed a series of experiments involving this important physical factor. These experimental results show simultaneously how the concentration and temperature effect the mesophases/ T_m . Lower- T features maybe related to intermediate phases (i. e structural dissociations, hairpin straightening) and as the temperature continuing to increase, the sDNA duplexes may cluster and associate together creating LC like phases right before reaching the melting temperature. The energy given further to the system (buffer + DNA) will help the structural/nucleotide dissociation. No more LC-phases have been observed beyond this point. This statement has been supported by earlier studies using other techniques as well (i.e. polarizing microscopy, X-ray diffraction) [29, 15].

To further understand the conformation changes of this macromolecular system under the electric field, the dielectric spectra have been shown. The frequency regime (greater than 100 kHz) used by far has been a power experimental method to understand the motion on molecular/atomic level. The low frequency regime (0.1-100 kHz) here is used mainly to probe the large-scale molecular motion and structural aggregation. We were able to detect a well-defined mode at low frequencies which can be an evidence of elongated structural dipole orientation. The driving mechanism for these elongated structures is believed to be the result of the stacking interactions between the paired terminal bases of the blunt-ended duplexes and furthermore these anisotropic assemblies can orientationally and positionally order [15].

Considering the fact that the DNA structures have relatively high concentration and enough time to self-organize in layers, the lower frequency

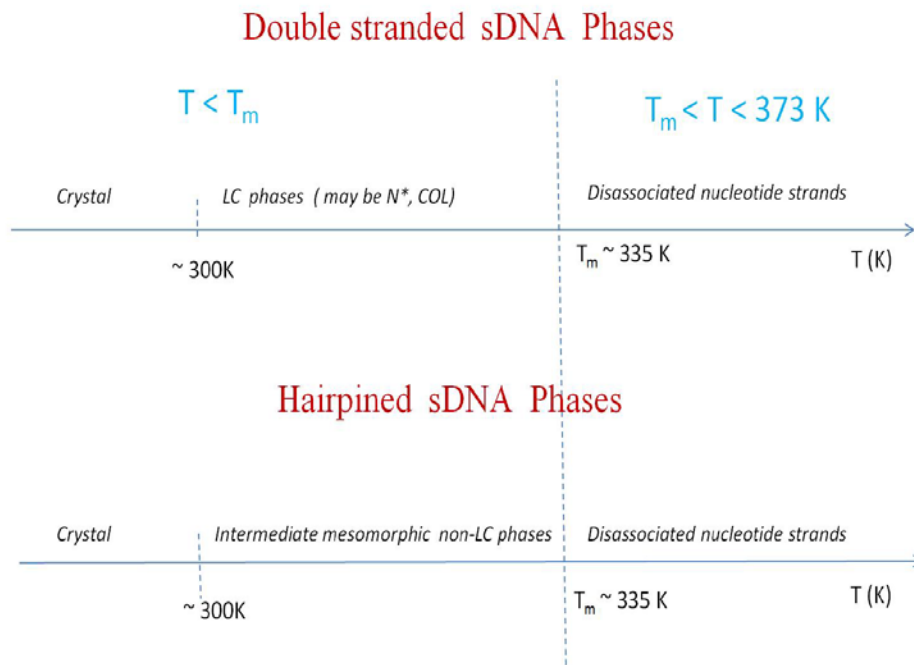


Figure 3.10. Phase diagram of structure evolution as a function of temperature in highly packed DNA environment showing both, main structural groups (hairpins and double strands) through intermediate phases between 300 and 335 K. The structures may form crystal like phases below 300 K, but for high temperatures, greater than the melting temperature T_m , only the disassociated nucleotide strands can still exist.

mode may be present because of the induced dipoles within the multiple DNA structural self-oriented layers. In order to conclude all our experimental results we propose a new phase diagram that supports the DNA structural organization/ packing under the effect of physical factors as it is described above (**Figure 3.10**).

Knowing the importance of these microbiological systems and in order to understand better their phase behavior, our future work involves temperature dependent dielectric studies for different DNA concentrations in aqueous environment for both low and high frequency regime.

3.5 References

- [1] P. G. de Gennes and J. Prost, *The Physics of Liquid Crystals.*, Oxford University Press, (1993).
- [2] L. Ann Onsager, *NY Acad. Sci.*, **51**, 627 (1949).
- [3] R. Zandi, D. Reguera, R.F. Bruinsma, W.M Gelbart, J. Rudnick, *Proc. Nat. Acad. Sci. USA*, **101**, 15556 (2004).
- [4] N. Seeman , *Nature*, **421**, 427 (2003).
- [5] G. Zanchetta, M. Nakata, M. Buscaglia, T. Bellini and N. A. Clark, *Proc. Nat. Acad. Sci. USA*, **105**, 1111 (2008).
- [6] Zhang Lin, Chen Wang, Xizeng Feng, Maozi Liu, Jianwei Li and Chunli Bai, *Nucleic Acids Research*, **26**, 3228 (1998).
- [7] F. Livolant , *Eur J Cell Bio*, **33**, 300 (1984).
- [8] M. H. F. Wilkins, *Nature*, **171**, 738 (1953).
- [9] A. Leforestier and F. Livolant, *Biophys. J.*, **65**, 56 (1993).
- [10] R. L. Rill, T. E. Strzelecka, M. W. Davidson, and D. H. Van Winkle. *Physica A*. **176**, 87 (1991).
- [11] A. M. Levelut, J. Doucet, J. P. Benoit, *Nature*, **339**, 724 (1989).
- [12] R. L. Rill, T. E. Strzelecka, M. W. Davidson, D. H. Van Winkle, *Physica A*, **176**, 87 (1991).
- [13] K. Merchant, R. L. Rill, *Biophys. J.*, **73**, 3154 (1997).
- [14] P. J. Hagerman, *Annu. Rev. Biophys. Chem.*, **17**, 265 (1988).
- [15] M. Nakata, G. Zanchetta, Brandon D. Chapman, Christopher D. Jones, J. O. Cross, R. Pindak, T. Bellini, N. A. Clark, *Science*, **318**, 1276 (2007).
- [16] R. Wing , *Nature*, **287**, 755 (1980).

- [17] M. R. Redinbo, L. Stewart, P. Kuhn, J. J. Champoux, W. G. J. Hol, *Science* , **279**, 1504 (1998).
- [18] C. A. Davey, D. F. Sargent, K. Luger, A. W. Maeder, T. J. Richmond, *J. Mol. Biol.*, **319**, 1097 (2002).
- [19] L. Li, S. A. Pabit, J. S. Lamb, H. Yoon Park, and L. Pollacka , *Appl. Phys. Lett.* **92**, 223 (2008).
- [20] Ch. Maffeo, B. Luan and A. Aksimentiev, *Nucleic Acids Research*, **40**, 3812 (2012).
- [21] H. Gobrecht, K Hamann, and G. Willers, *J. of Phys. E-Scientific Instruments*, **4**, 21 (1971).
- [22] <http://www.tainstruments.com>
- [23] S. Pilla, J. A. Hamida, and N. S. Sullivan, *Rev. of Sci. Instrum.*, **70**, 4055, (1999).
- [24] S. C. Bera, S. Chattopadhyay, *Measurement* , **33**, 3 (2003).
- [25] M. C. Foote and A. C Anderson, *Rev. of Sci. Instrum.* , **58**, 130 (1987).
- [26] I. Rouzina and V. Bloomfield, *Biophys. J.*, **77**, 3242 (1999).
- [27] R. Owczarzy, I. Dunietz, M. A. Behike, and I. M. Klotz, *Proc. Nat. Acad. Sci. USA*, **100**, 14840 (2003).
- [28] C. Richard and A. J. Guttmann, *J. of Stat. Phys.*, **115**, 925 (2004).
- [29] G. Zanchetta, *Liquid Crystals Today*, **18**, 40 (2009).
- [30] A. D. Rey, *Soft Matter*, **6**, 3402 (2010)
- [31] J. L. Sirakov, J. Pelta and F. Livolant, *Biophys. J.*, **67**, 1387 (1994).

CHAPTER 4

UNDERSTANDING LYSOZYME CONFORMATION IN AQUEOUS SOLUTIONS BY THERMAL STUDIES OF LOW-FREQUENCY DIELECTRIC SPECTRA AND CALORIMETRY.

Abstract

The origin of a wide variety of pathological conditions is the failure of proteins to fold correctly or to remain correctly folded. Previous studies show that conformational stability is a result of effects involving hydrophobicity and hydrogen bonding. The driving force for denaturing by temperature is the increase in entropy that helps the transition of a single protein conformation into an ensemble of random ones. Thermodynamic studies of pro-

teins used differential scanning calorimetry (DSC) at relatively high scan rate (10-20 K/min). The denaturation of proteins studied this way cannot probe all the transformations, and may suppress the aggregation to gels. The experimental results presented here, show the thermal denaturing of the diluted lysozyme, which occurs gradually over a broad temperature range as a series of transformations, some of which are reversible. Also, the aggregation of the protein to gel is probed as a result of a very low heating scan rate (0.017 to 5 K/min) by both methods AC-calorimetry and modulated DSC. In addition, we have analyzed the low frequency (1-100 kHz) dielectric spectra of the protein-solvent system and explained to our knowledge the relaxation process of the diluted lysozyme. Until recently, the literature contained no data concerning the dielectric behavior under certain physical conditions that we have performed our measurements.

4.1 INTRODUCTION

Proteins are important units in governing the functions of living systems. The biological activity of proteins depends on their three-dimensional native structure in solution and slow fluctuating modes. Folding and unfolding of all or parts of a protein's structure are crucial ways of regulating biological activity and targeting proteins to different cellular locations. The origin of a wide variety of pathological conditions is the failure of proteins to fold correctly or to remain correctly folded [1].

Most studies show that conformational stability is a result of effects involving hydrophobicity and hydrogen bonding. Early research on protein stability attempted to explain the structural changes of proteins as a result of

changes in physical, chemical or biological properties [2]. These are configuration changes of the protein's folded structure and are demonstrated mainly in the polypeptide chain. In principle, molecular changes should be quantitatively compared with the native state. In practice, the state of the molecules prepared by the mildest extraction method is conventionally *assumed* to be the protein's native state. The denaturation process can be defined as any structure modification of the protein molecule, but excluding any breaking of covalent bond [3].

Previous investigations carried out by Raman spectroscopy and differential scanning calorimetry (DSC) have shown that the thermal denaturation process of most proteins can be described by two stages. During the first stage, the tertiary structure unfolds, exposing the secondary structure to the solvent environment. The increased solvent penetration into the interior of the protein is thought responsible for the destabilization of the entire molecular conformation [6]. The first transformation step is characterized by breaking the imbalance between hydrophobic and hydrophilic interactions. The water penetration will favor the hydrophobic interactions in the protein interior. As a result the second stage of the thermal denaturation will be the unfolding process of the secondary structure [4].

Some of the denaturing processes are: temperature, changing pH of the solution, denaturants (inorganic salts, organic solvents and detergents), ultrasonic homogenization, and high pressure. Many studies have investigated the influence of additives on the stability of the protein aqueous solutions. In particular, some sugars are known to enhance the stability of proteins [5]. The temperatures at which the proteins unfold vary widely. Most proteins unfold at high temperatures (70-90 °C) but structural alterations

have been seen even at low temperatures (-30- -10 °C) for some proteins. The driving force for denaturing by temperature is the increase in entropy that helps the transition of a single protein conformation into an ensemble of random ones. The entropy contribution increases as the temperature increases and at some temperature, overcomes the interactions responsible for its structure. At this point, the protein is heat denatured and the buried non-polar amino acid residues are exposed. The intermolecular clustering may lead to aggregation of the denatured protein. Furthermore, protein interactions under certain circumstances can lead to gelation, a very important process in the food industry [6, 7]. Here, specific interactions such as in clotting of fibrin and antibody-antigen interactions may be responsible for the formation of gel-like aggregates [8, 9]. Gels can be well-ordered lamellar structures (phospholipids) or completely disordered with structural units covalently linked to one another (condensation polymers). Some types of gels are primary macromolecules bound together via multi-stranded helices where the network is caused by physical aggregation of chains, previously disordered, but now with regions of local order. Globular protein network gels morphologically are classified as lattice gels. Aqueous solutions with high concentrations of these proteins can be converted to gels by slowly heating the unfolded (denatured) proteins [10, 11]. The first thermodynamic studies in the 1970s of protein denaturation used differential scanning calorimetry (DSC) at relatively high scan rate (10-20 K/min). The heat capacity $C_p(T)$ typically exhibits a broad endothermic peak where the area has been interpreted as being equal to the total enthalpy of transformation of proteins. Because of the very fast scan rates, it is uncertain as to whether the denaturation of proteins can be seen as entirely a fast thermodynamic irreversible transition or wheth-

er it occurs gradually over a broad temperature range as a series of transformations, some of which may be reversible. Also, heating the protein very fast will suppress the aggregation to gels, a very important step of protein transformations. The recent studies using MDSC have attempted to probe reversible and nonreversible components of the protein transformation but this question remains largely open [12, 13].

It is well established that the function of a protein is related to the surrounding water. Proteins should have a certain hydration level in order to have the full flexibility and motion necessary for their full biological function. See Chapter 1. Several experimental studies have tried to answer the question how the dynamics of a protein (and so its function) is related to the surrounding solution environment. Dielectric spectroscopy has been widely used and the dielectric loss spectra have been analyzed to understand the relaxation processes present in the protein–solvent system. It is believed that the low frequency modes (for temperatures below 300 K) belong to the reorientation of the bound water and the unfolded protein molecules [14, 15]. The collective vibrational modes associated with protein tertiary structure lay mostly in the terahertz frequency range. The dielectric response of this range is currently being considered as a possible bio-sensing technique. Measurements of these modes can be accomplished also by Raman spectroscopy, neutron inelastic scattering, and far infrared dielectric response [16].

Until recently, the literature contained no data concerning the dielectric behavior of proteins at room temperature in aqueous solutions and low frequencies. This is the gap that we fill by applying calorimetry (both AC and MDSC) as well as low frequency (0.1 to 100 kHz) dielectric spectroscopy on a diluted protein solution. All measurements have been performed on hen

egg-white lysozyme dissolved in PBS (pH 7.4 and protein weight fraction φ_w 0.7, 0.19 and 0.32) from 20 to 100 °C. From the heat capacity profile, the temperatures and a related enthalpy change of the protein denaturing is probed. The heat capacity peak broadens and new features are revealed as the temperature scan rate is lowered to +0.017 K/min using AC calorimetry method. Significant differences are observed using the MDSC technique at scan rates of from 0.22 to 5 K/min. The temperature dependence of the permittivity, ϵ' , and the loss factor, ϵ'' , at 100 kHz of the diluted protein show features associated with those seen in the heat capacity (AC and MDSC). All results are interpreted in terms of protein denaturing then subsequent gelation that depend on protein sample concentration, which is supported by the frequency dependence of the permittivity at room temperature after thermally cycling.

4.2 Experimental

4.2.1 Materials and sample preparation

The lysozyme used for this experiment is extracted from hen egg-white **Figure 4.1** gives a schematic of the molecular structure (primary) of lysozyme. It was purchased from Alpha Aldrich in crystallized form, was used without further purification, and was kept continuously in a freezer (−20 °C) until used. The proper amount of protein and PBS (buffer solution pH = 7.5, purchased from the same company) were mixed in a vial. The mixture was then mechanically mixed further in a touch mixture for about 5 minutes.

Different samples having $\varphi_w = 0.07, 0.19,$ and 0.32 were prepared using the same procedure. Here, $\varphi_w = m_{LYS} / (m_{LYS} + m_{PBS})$ is the weight fraction of lysozyme and m_{LYS} and m_{PBS} are the weight of lysozyme and buffer solution respectively. After the sample was ready, it was introduced into a cup + lid type silver cell of dimensions $3.14 \times 7^2 \times 1.5\text{mm}^3$ and $3.14 \times 3^2 \times 2\text{mm}^3$ for the AC- calorimetry and MDSC methods, respectively. The sample was prepared at the same way for the dielectric spectroscopic studies, but used an Instec electro optical-cell as the capacitive sample holder. See Chapter 2.

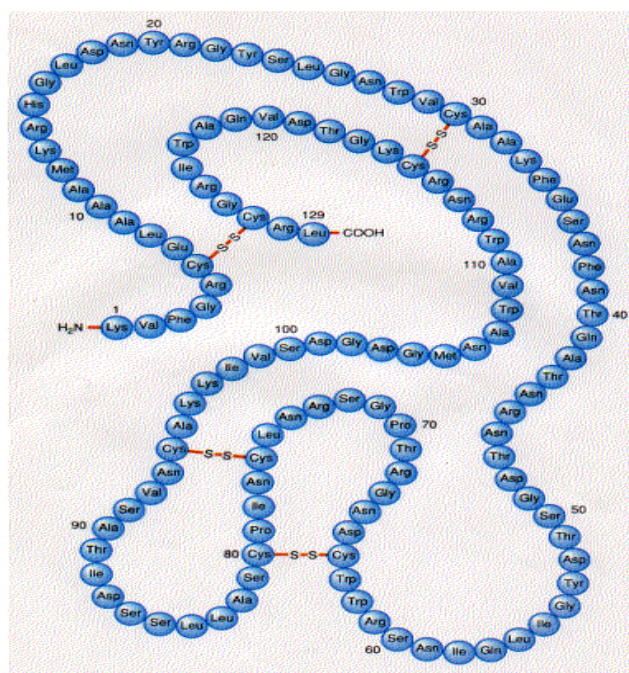


Figure 4.1. *Primary structure of lysozyme. Peptide Chain made out of 129 aminoacids and disulfite bridges, connected by covalent bonds (red lines) [21].*

The amount of sample used on each experiment was $(m_{Lys} + m_{PBS}) \approx 5$ mg. The experiment was performed immediately after the cell+ sample were mounted into the instruments.

4.2.2 Results

The first group of data is taken using calorimetric methods by starting with AC- calorimetry and then MDSC mode, making possible direct calorimetric measurements. In order to have a complete study and be able to understand any macromolecular transformation for high temperatures (beyond 90 °C), we have studied both the diluted lysozyme and crystalized powder (though not vacuumed). The data shown in **Figure 4.2** and **Figure 4.3** are an overlay of calorimetry and dielectric spectroscopy results. The sample is heated at +0.22 K/min over a temperature range from 40 to 150 °C . The activities presented on both figures are a clear evidence of the glass transition, a well-studied characteristic of protein transformation for very low temperatures [15]. The heat capacity (both the reversible and nonreversible) show only a glass transition-like feature that starts at around 120 °C. This transition is evident at the dielectric loss behavior as well. More molecular orientation activity is shown at around 90°C at the dielectric storage as well. It is believed, that the bounded water layer over the protein molecules plays the main role on the present electric field changes (See Section 1.4). Further work is done on lysozyme in solution. Our AC-calorimetry results on diluted protein ($\phi_w \approx 0.30$, rate = 0.017 K/min) show a series of transition steps on complex heat capacity C^* (circles) and phase shift (stars) graph as a function of temperature T and an overall broader peak (**Figure 4.4**).

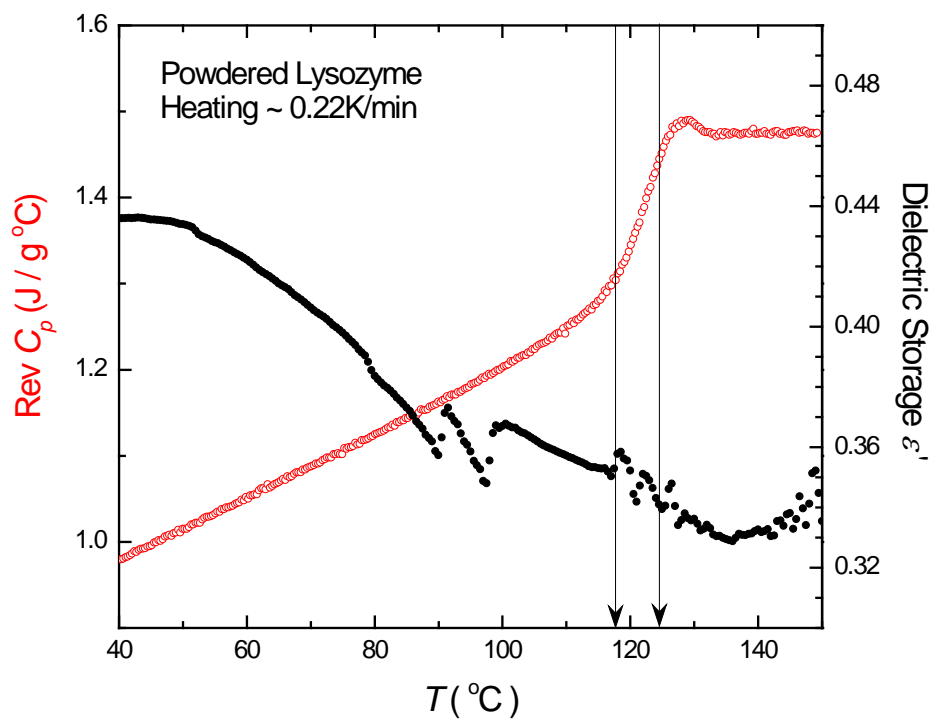


Figure 4.2. Real part of the specific heat, $\text{Rev } C_p$ (open circles) and dielectric storage, ϵ' (filled circles) at 100 kHz on powder lysozyme, as function of temperature (heating rate $+0.22\text{K/min}$). A glass transition is evident at $\sim 120^{\circ}\text{C}$ on both graphs.

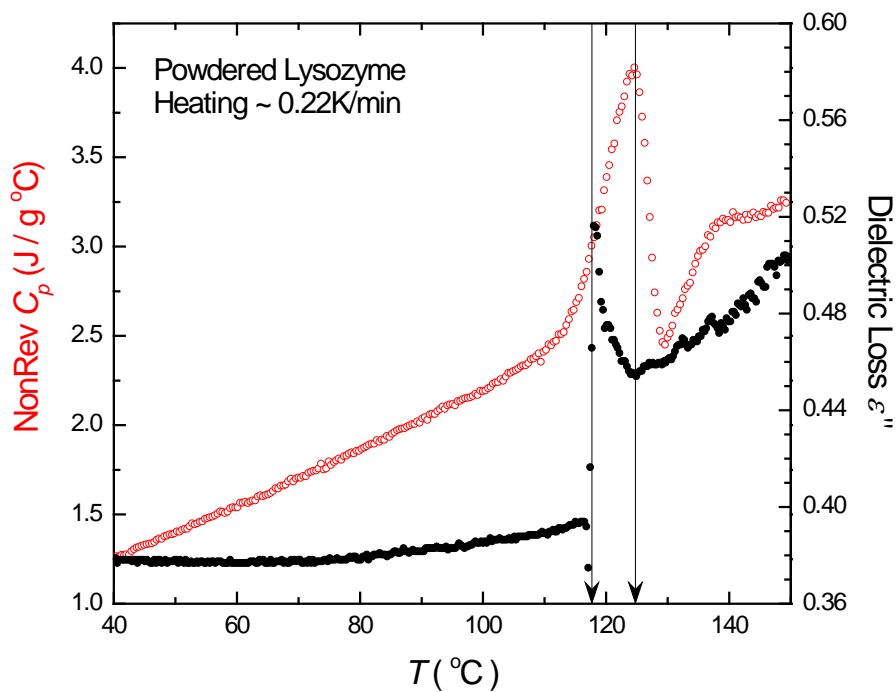


Figure 4.3. *Imaginary part of the specific heat, NonRev C_p (open circles) and dielectric loss ϵ'' (filled circles) at 100 kHz on powder lysozyme, as a function of temperature (heating rate +0.22 K/min). A glass transition is evident at $\sim 120^\circ\text{C}$ on both graphs.*

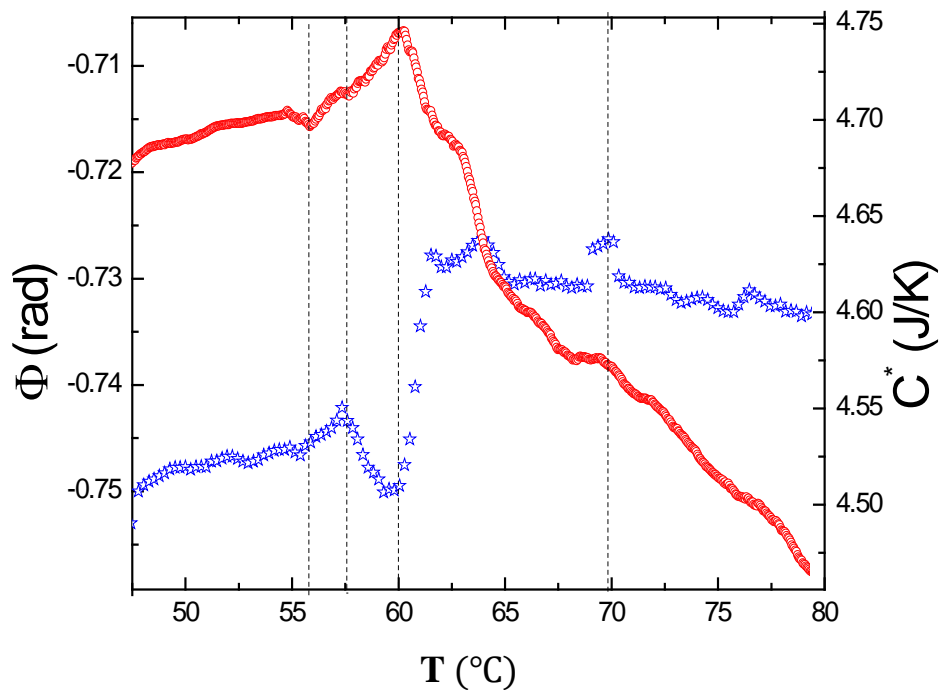


Figure 4.4. AC-calorimetry on diluted lysozyme. Effective heat capacity C^* and phase shift Φ as a function of temperature at $+0.017$ K/min on lysozyme concentration $\varphi = 0.30$. The dash-dot lines indicate the transition temperatures respectively. The first two (at 51 and 55 °C) may belong to untangling of α -helixes, β -sheets ($\alpha\beta$ -intermediate) and to further straightening of β -sheets (α -intermediate).

These small C^* changes are believed to be the small energy contributions coming from intermediate protein unfolding stages, which are supported by phase shift Φ features as well. The first two (at 51 and 55 °C) may belong to untangling of α -helices, β -sheets ($\alpha\beta$ -intermediate) and to further straightening of β -sheets (α -intermediate). Earlier studies on lysozyme have found that unfolding of α -helices has a greater energy contribution compared to that of β -sheets (See Chapter 1). Based on this, we believe that the peak at around 60 °C shows mostly the energy outcome of the transition from α -intermediate to a tangled polypeptide of primary structure. After 65 °C, heat capacity baseline decreases drastically because of sample mass loss due to cell leakage. In fact, several different cell designs were attempted, but were not successful, because above 50 °C the vapor pressure of water likely causes seal failure for the AC custom-made cells. High temperature calorimetric measurements are important for protein gelatin studies. For this purpose is chosen DSC/MDSC method. The cell+bath system of Q200 can reach 100°C, but the sample does not evaporate or leak. **Figure 4.5** shows a full cycle of heat + cool + heat of protein sample having still $\phi_w \approx 0.30$ and a relatively very low heating rate 0.22 K/min.

There is some interesting information provided over this broad temperature range (45 - 85 °C). During the first heating scan, the thermal profile shows two transformation peaks. The first one, at around 67 °C, is believed to represent the protein unfolding. The second transformation involves less energy than the previous one and takes place at around 84 °C. High concentration and a slow heating rate have helped the aggregation/ gelation process [19, 20]. The second feature is the evidence of this important transformation. Also, it is interesting that during cooling this peak will be flat, but will be

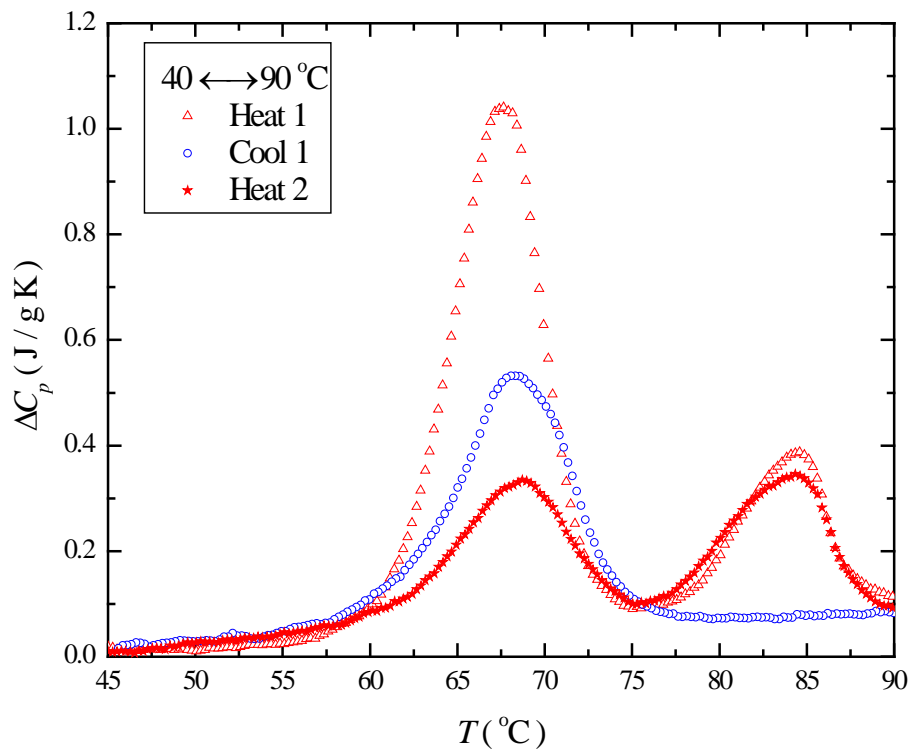


Figure 4.5. Thermal cycling on diluted lysozyme $\phi_w = 0.32$ showing the excess specific heat ΔC_p , as a function of temperature at ± 0.22 K/min. Both heating profiles (red triangles-first heat and red stars-second heat) show the thermal signatures at 67 and 84 °C. The 84 °C peak is not present on cooling (blue circles) that was intermediate between the two heating scans.

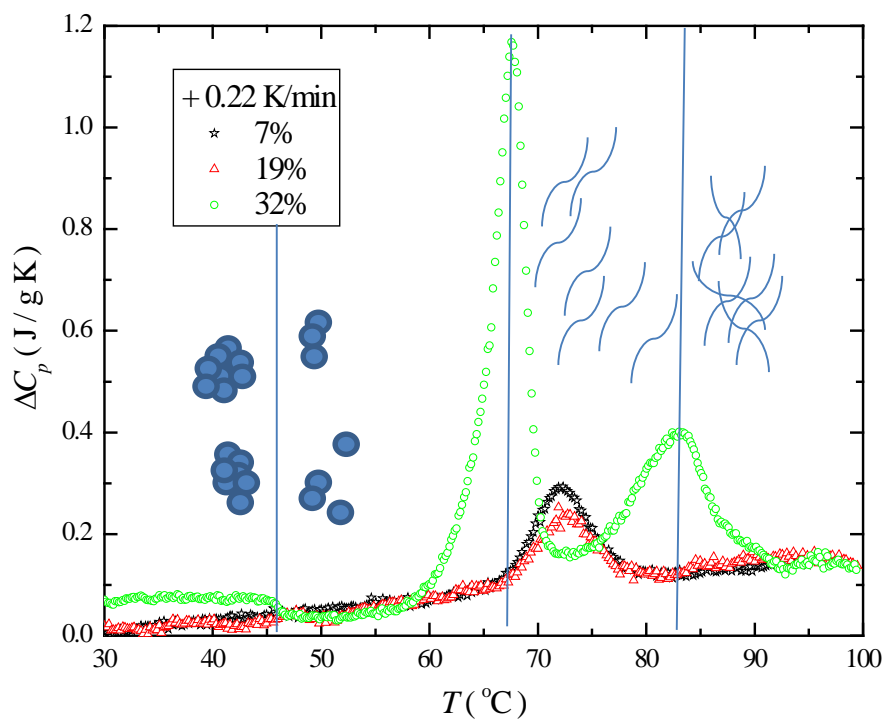


Figure 4.6. Concentration effect on the excess specific heat ΔC_p over a wide temperature range on Lysozyme+PBS at a fixed heating rate +0.22 K/min. For the highest concentration $\phi \approx 0.32$ (green circles), two peaks are shown compared to other thermal profiles for $\phi \approx 0.19$ (red triangles) and $\phi \approx 0.07$ (black stars), where only one peak is present. The 84 °C peak for $\phi \approx 0.32$ present the protein gelation peak. The blue circles are an illustration of the native molecule structures that will unfold and tangle (arcs) for high temperatures.

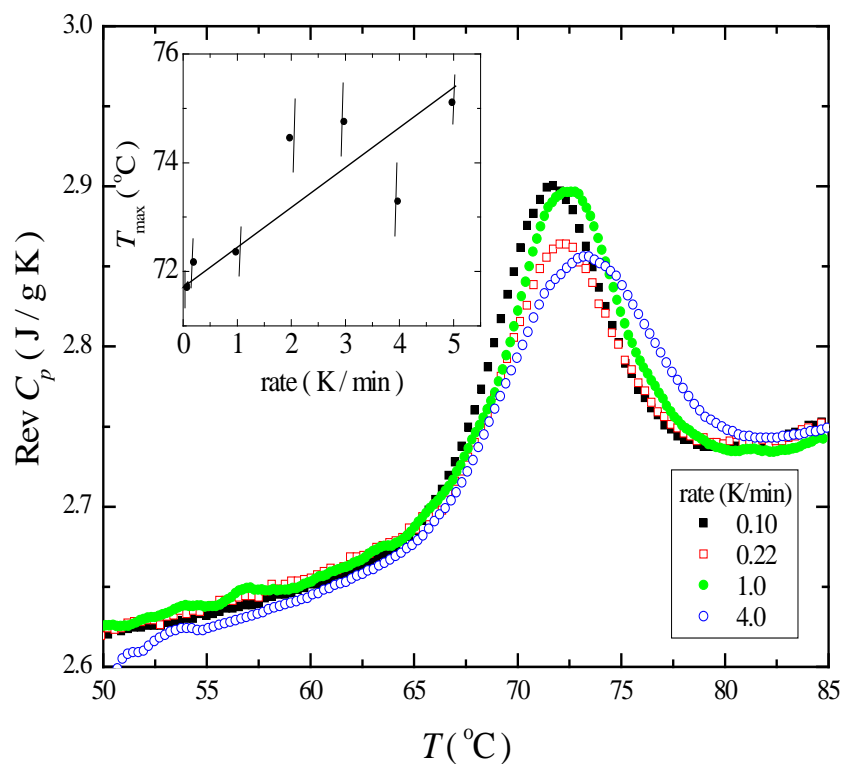


Figure 4.7. *Temperature scan rate effect on lysozyme+PBS for the same concentration ($\phi_w \approx 0.07$) on the excess specific heat. Real part of specific heat $\text{Rev } C_p$ as a function of temperature T shows the dependence of the unfolding peak displaced by ~ 5 K toward higher temperatures as the scanning rate increases from 0.10 K/min (black filled squares) to 4 K/min (blue opened circles). The small figure inside shows the dependence of the peak maximum temperature T_{\max} as a function of scan rate. Error bars come from reproducibility, not just instrumentation.*

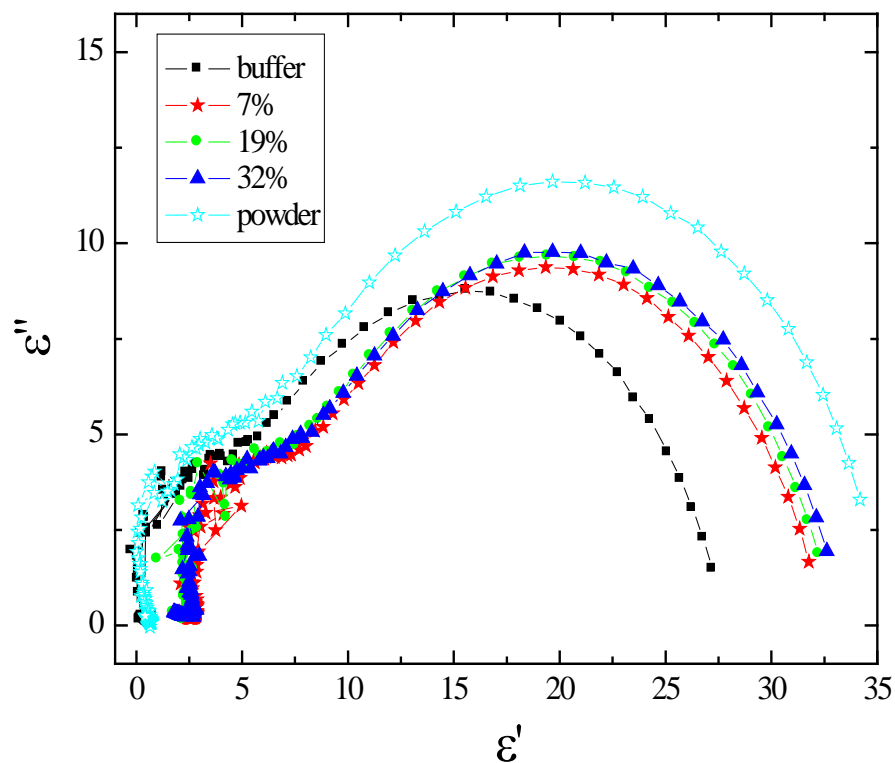


Figure 4. 8. Cole-Cole plots of imaginary part $\epsilon''(\omega)$ versus real part $\epsilon'(\omega)$ for different protein concentrations and at a constant voltage $V = 5 \text{ V}$. Note that the direction of increasing frequency is toward the 0 of $\epsilon'(\omega)$ axis. The first mode is not evident on all the graphs because of the noise present due to loss of sensitivity of the instruments. The second mode appears on two different frequencies for different protein solutions ($f = 7.5 \text{ Hz}$) and buffer ($f = 8 \text{ Hz}$).

fully reproducible during the next heating. The fact that the unfolding peak cannot repeat itself as the sample is heated for the second time, shows that the protein unfolding in this case is partially reproducible.

Further MDSC measurements (**Figure 4.6**), show how the protein transformation is affected as φ_w is decreased. For low weight fraction $\varphi_w \approx 0.07$ and $\varphi_w \approx 0.19$, all the transformations are represented by a single heat capacity peak and less energy released (area under the smaller peak). **Figure 4.7** explains further how this single feature is affected by increasing the temperature scan rate for the same $\varphi_w \approx 0.07$. The transition temperature is displaced about 5 K towards higher temperatures as the temperature rate increases from 0.10 to 4 K/min. The relative error related to the sample treatment and history is presented by error bars.

The dielectric spectroscopy data are given in **Figure 4.8**. The Cole-Cole analysis for frequency regime (0.1 to 100Hz) show the modes involved during the reorientation of the protein molecules and bounded buffer molecules. There are present two frequency modes for all the protein solutions ($\varphi_w \approx 0.07$, 0.19, and 0.32), including buffer and protein powder. The first mode is not evident on all the graphs because of the noise present due to loss of sensitivity of the instruments. The second mode appears on two different frequencies for different protein solutions ($f = 7.5 \text{ Hz}$) and buffer ($f = 8 \text{ Hz}$).

Each of the figures shown here represent the best of the data set. There have been at least 5 experimental trials for each of the graphs shown above. In-

formation related to the absolute error (instrumentation error) for each of the methods used above can be found on section 3.2.2 & 3.2.3.

4.3 Discussion and Conclusions

The thermal unfolding of lysozyme in PBS shows similar features as all other globular proteins. An overall heat capacity increment is almost the universal characteristic of the unfolding transition and all our calorimetric measurements have this C_p behavior. Similar changes in C_p are seen in measurements of protein-protein interactions, protein-ligand binding and other macromolecular processes. It is believed that these changes are mostly the result of energy contribution from non-covalent bond breakings [12, 13, 17]. It is believed that the thermal unfolding of lysozyme happens through more than 1 step. The energy given to the system will increase the molecular kinetics, the molecular breakage that follows will help the tertiary structure to unfold and expose the inner protein parts to the polar solvent molecules. If the system energy continues to increase as the temperature goes up, the secondary structure will start the transition as the α -helixes and β -sheets start unfolding. The unfolded lysozyme will stay as a primary structure peptide as far as there are no chemical factors to disrupt the disulfide bridges [3, 5, 12, 13]. These intermediate transformation stages are illustrated on **Figure 4.9**. There does not exist any DSC/MDSC thermal profile (literature supported), that shows the transition temperature for each step or to support experimentally the energy needed for each intermediate transformation to occur.

Based on our experimental results and literature references discussed earlier on this chapter, we support the fact that the driving force for

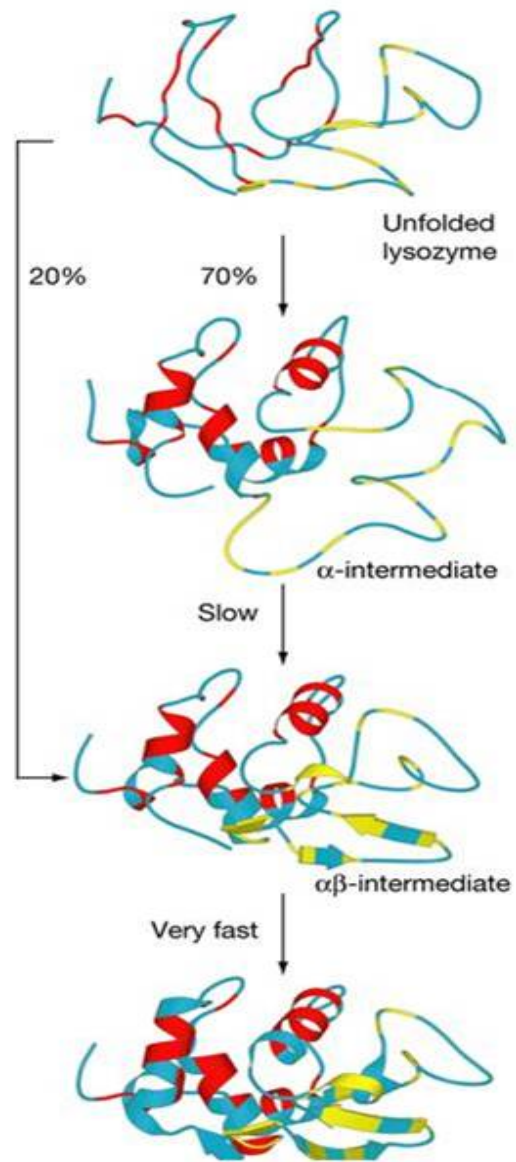


Figure 4.9. Folding/unfolding schematic of lysozyme. The α -helixes are in red and blue, β -sheets are in yellow and blue [22].

denaturation is the increase in entropy of the system. This will help the transition of a single conformation into an ensemble of single ones. We can probe and affect this transition by controlling the physical parameters (i.e. temperature rate, oscillation frequency). The midpoints of the transitions are scanning rate dependent, indicating that the denaturation process is kinetically controlled. Very low scan rates (**Figure 4.3**) and high sample concentration favor the intermediate transition steps, considered as a prerequisite for further clustering and protein gelation [18]. The lysozyme + PBS thermal profiles reveal a single feature at ~ 72 °C for $\phi_w < 0.32$ but two features for $\phi_w = 0.32$ at 66 and 84 °C and all “reversible”. This lower temperature process may be related to protein unfolding, leading to large structures while the higher temperature feature may be related to non-independent monomers (perhaps random associations of α helices and β sheets).

NMR spin relaxation experiments have demonstrated that a chemical denaturant increases the fluctuations of the protein that eventually leads to its unfolding [9]. There have been suggestions that the flexibility of proteins is related to the structural stability, but still this is not a clear mechanism yet. In this work, we tried also to control the protein motion and orientation by using dielectric spectroscopy.

The low frequency dynamics of the lysozyme+PBS, likely involving the reorientation or redistribution of the bound water and the protein, are different than that in powder lysozyme and are due to the aqueous environment (Swelling and self-assembly? Still an open question). Powder (but not dry) lysozyme exhibits a glass-like *melting/denaturing* at high- T (~ 120 °C), supported by dielectric spectroscopy as well, is consistent with literature [19, 20].

4.4 References

- [1] C. M. Dobson, *Nature*, **426**, 884 (2003).
- [2] I. Langmuir , V. J. Schaefer, *J. Am. Chem. Soc.*, **60** (6), 1351 (1938).
- [3] M. Joly, “A *Physico-Chemical Approach to The Denaturation of Proteins*”, Academic Press (*London and New York*), (1965).
- [4] M. Descamps, *J. Phys. Chem. B*, **110**, 22886 (2006).
- [5] E. Hashimoto, Y. Aoki, Y. Seshimo, K. Sasanuma, Y. Ike, and S. Kojima, *Jpn. J. Appl. Phys.*, **47**, 3843 (2008).
- [6] C. Tanford , *Adv. Prot. Chem.*, **23**, 121 (1968).
- [7] J. W. Nelson , T. E. Creighton, *Biochem. J.*, **33**, 5974 (1994).
- [8] R. H. Schmidt and B. L. Illingworth, *Food Product Development*, **12** (10), 60 (1978).
- [9] G. E. Schulz and R. H. Schirmer, “*Principles of Protein Structure*”. In *'Springer Advanced Texts in Chemistry'*, Springer-Verlag, New York (1990).
- [10] A. J. Mandell, P. V. Russo, B. W. Blomgren, *Ann. NY Acad. Sci.*, **504**, 88 (1987).
- [11] K. Almdal, J. Dyre, S. Hvidt , O. Kramer, *Polymer Gels and Networks*, **202**, 15 (1993).
- [12] S. Presto, E. Tombari, G. Salvetti, and G. P. Johari, *Phys. Chem. Chem. Phys.* **4**, 341 (2002).
- [13] H. Yan, A. Saiani, A. F. Miller, *Macromolecular Symposia*, **251**(1), 112 (2007).
- [14] H. Bysell, R. Månsson and M. Malmsten, *Colloids and Surfaces. Physicochemical and Engineering Aspects*, **62**, 391 (2011).

- [15] P. W. Fenimore, Hans Frauenfelder, B. H. McMahon, and R. D. Young, *PNAS*, **101**(40), 14408 (2004).
- [16] T. Q. Luong, P. K. Verma, R. K. Mitra, and M. Havenith, *Biophysical Journal*, **101**(4), 925 (2011).
- [17] A. Cooper, *Biophysical Chemistry*, **85**(1), 25 (2000).
- [18] C. Tanford, *Adv. Prot. Chem.*, **23**, 121 (1968).
- [19] T. J. Kamerzell and C. R. Middaugh, *J. Pharm. Sci.*, **97**, 3494 (2008).
- [20] V. Doan-Nguyen and J. P. Loria, *Protein Sci.*, **16**, 20 (2007).
- [21] <http://users.rcn.com/jkimball.ma.ultranet/BiologyPages/L/Lysozyme.html>
accessed 01/28/2013.
- [22] P. C. Stirling, V. F. Lundin, and M. R. Leroux, *EMBO Reports*, **4**, 565 (2003).

CHAPTER 5

PSEUDO-PHASE DIAGRAM OF MICROSTRUCTURES IN CHEMICALLY- DEFINED LIPID CONCENTRATES BY OPTICAL MICROSCOPY AND HIGH- RESOLUTION CALORIMETRY

Abstract

Chemically Defined Lipid Concentrate (CDLC) is a model bile composed of a cholesterol, large non-ionic surfactant/emulsifier as well as a tri-block copolymer (bilayer-forming amphiphiles), fatty acids (micelle-forming amphiphiles), and water. This system is characterized by self-assembly of a variety of microstructures ranging from filaments to helical ribbons to tubules to crystals. Several competing theoretical models have been proposed, and

experimental methods have been applied to explain the formation of microstructures as well as physico-chemical properties of them. To date no one single theoretical approach accounts for all of the unique features associated with quaternary sterol systems, CDLC being one of them. These self-assemblies lend themselves to thermodynamic measurements; however, the literature on the topic is limited. To understand the kinetic evolution of the metastable intermediates toward ChM crystal, this Chapter describes an optical microscopy, modulation and differential scanning calorimetry study of CDLC as a function of temperature, temperature scan rate, and dilution. A free energy landscape for microstructure temporal evolution towards full ChM state as well as pseudo phase diagram are proposed to describe this unique system and its structural components. The main features of it are the two solid curves representing the high-temperature boundary with the melting of ChM into an isotropic melt and the low-temperature boundary where the CDLC microstructures evolve at such a slow rate that they can be considered "frozen", and since these are meta-stable structures, this region has many features in common with glasses.

5.1 Introduction

Complex fluids present a myriad of interesting and important phenomena. One in particular that has attracted considerable research is the self-assembly of filamentous, helical ribbon, tubular, and crystal microstructures in quaternary sterol systems [1]. Involving a number of important open questions regarding the kinetic evolution and properties of the microstructures formed,

these systems remain inadequately understood. Originally discovered in native gallbladder bile, these microstructures were thought to be the result of the cholesterol crystallization process in a system supersaturated with cholesterol [2].

To understand formation of the microstructures, the native bile was modeled as a quaternary sterol system (or a “model bile system”) composed of cholesterol, bile salts, and phospholipids [2–4]. Similar structures were later found in a large variety of analogous systems each comprised of a sterol (cholesterol analog), bilayer-forming surfactant(s), and micelle-forming amphiphile(s) [1]. One of the more interesting features of all of these systems is formation of helical ribbons, spring-like structures with diameters and axial lengths ranging from 5 to 100 μm and 5 to 300 μm , respectively. Despite large differences in dimensions, all of the helical ribbons form in one of the two types of pitch angles, either 11° or 54° . Moreover, the helical ribbons are predominantly right-handed regardless of the chirality of the molecules comprising quaternary sterol systems studied [1]. These unique features of the quaternary sterol systems continue to be a subject of ongoing research [5].

A useful complex fluid model that has provided insight into many physical phenomena in quaternary sterol systems is a Chemically Defined Lipid Concentrate (CDLC). CDLC is composed of a cholesterol, large non-ionic surfactant/emulsifier as well as a tri-block co-polymer (bilayer-forming amphiphiles), fatty acids (micelle-forming amphiphiles), and water. Similarly to native and model biles, this system is characterized by self-assembly of a variety of microstructures ranging from filaments to helical ribbons to tubules to crystals (**Figure 5.1**). Understanding the physics involved in formation and temporary evolution of these structures including

their physico-chemical properties may lead to a bio-inspired design of these microstructures for a range of useful technical applications, e.g., microscale force transducers [1, 6, 7].

Several competing theoretical models have been proposed to explain the formation of microstructures as well as physico-chemical properties of helical ribbons [6, 8–18]. Because of the chiral nature of the helical ribbons and the chirality of its molecular constituents, the initial theories attempted to describe these microsprints as fluid bilayers by employing a curvature elasticity approach [19]. This initial methodology has been subsequently expanded to account for the helix geometric and elastic properties by employing boundary (edge) effects [20], topological defects within the ribbon [21], and molecular tilt [22]. A separate theoretical approach employed an explicit analogy to chiral liquid crystals [7, 15, 16, 23–26]. A more recent phenomenological theory attempting to explain helix elastic properties is based on the hypothesis that helical ribbons are crystal rather than liquid crystalline in nature. This theory utilizes the spontaneous curvature of a flat crystal strip as a driving force for helix formation [17, 18]. To date no one single theoretical approach accounts for all of the unique features associated with quaternary sterol systems, CDLC being one of them. For helical microstructures, this is due to the ubiquitous binary helix pitch angles, the large ribbon thicknesses (1 to 2 orders of magnitude larger than those of lipid bilayers), unique helical ribbon handedness independent of the constituent molecular chirality, the chemical structure of the sterol molecules, and other factors [1, 3, 17].

An important experimental finding relevant to this work is that the nature of the cholesterol organization within helical ribbons is crystal rather than liquid crystalline [2, 4, 5, 15, 27]. This organization is similar to cholest-

terol monohydrate (ChM) except that the unit cell length perpendicular to the cholesterol layer is increased three times compared to that of ChM [5]. The underlying organizations of other microstructures present in quaternary sterol systems (filaments, tubules, and crystals) have been proposed to be anhydrous cholesterol (ACh), admixture of ACh and ChM, and pure ChM crystals, the latter being an equilibrium form of cholesterol.

The recent x-ray and electron diffraction findings related to helices [5, 27] along with observations of the kinetic evolution of other structures present in quaternary sterol systems [1, 2, 4, 15, 17] reinforce that filament, helix, and tubule microstructures all appear to be metastable intermediates co-existing with ChM crystals. Due to their unique properties, including a number of intriguing transformations and co-existences, these self-assemblies lend themselves to thermodynamic measurements; however, the literature on the topic is limited. Early studies of the melting of pure ACh, ACh+ChM mixtures, and pure ChM crystals [28, 29] as well as more recent efforts on gallstones [30, 31] have been mainly studied by differential scanning calorimetry (DSC). Studies have been plagued by weak thermal signatures as well as difficult sample handling [32, 33], but have revealed important clues as to their thermal behavior. Related self-assembled systems of lipid-based unilamellar vesicles in aqueous solutions and low concentrations have employed both DSC and modulation (AC) calorimetry [34–37]. Here also, sample handling difficulties due to the sample aqueous nature and complex structural behavior have restricted the use of calorimetry. Results could only probe the melting into an isotropic liquid of highly concentrated Ch samples. Despite this limitation, calorimetry has yielded important information. Clearly, re-

newed efforts to more systematically utilize calorimetry in conjunction with complementary techniques are needed, especially for helical forming Ch-based structures where very little experimental information is available.

To understand the kinetic evolution of the metastable intermediates toward ChM crystal, this Chapter describes an optical microscopy, modulation and differential scanning calorimetry study of CDLC as a function of temperature, temperature scan rate, and dilution. The calorimetry temperature scan rate was varied from 0.017 to 1C/min on samples ranging from the original CDLC composition (denoted 1:1 stock solution:total volume) to those diluted with water to a 1:10 concentration. Microscopy confirms the presence of the three types of metastable microstructures in all samples studied. Furthermore, samples incubated at various temperatures exhibit additional clustering and/or alignment of the microstructures. Calorimetric thermal profiles are strongly dependent on scan rate, sample concentration, and thermal history, revealing numerous features with increasing temperature. Since the kinetics of CDLC increases with increasing temperature, this system cannot uniformly condense into ChM equilibrium state due to local concentration fluctuations; rather, it forms a set of intermediate slowly-evolving structures. These structures, filamentous, helical ribbon, and tubules, co-existing with each other and the environment from which they grow, evolve through a broad region of metastable chemical and structural equilibrium. A free energy landscape for microstructure temporal evolution towards full ChM state as well as pseudo phase diagram are proposed to describe this unique system and its structural components.

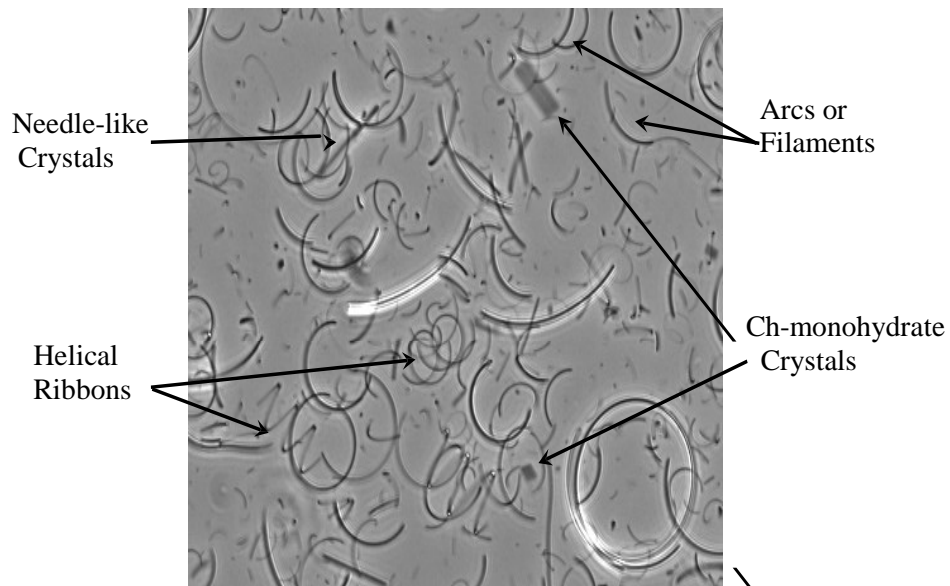


Figure 5.1. *CDLC Microstructures. Phase contrast optical microscopy of a CDLC sample at room temperature illustrating the typical coexisting microstructures present. The micrograph width represents 20 μm .*

BCO
 opti-
 lipid
 it is
 composed of three groups of components in water, i.e., a mixture of non-ionic surfactants (TweenTM 80 and Pluronic[®] F-68), fatty acids (micelle-forming amphiphiles), and cholesterol in 94.2:1.9:3.9 percent molar ratio. To

obtain a uniform suspension of microstructures in stock solution bulk, CDLC was micro-centrifuged prior to every sampling. A dilution series was then performed on the stock solution using de-ionized water, dH₂O, to prepare six 500- μ l samples with the following ratios of original CDLC solution to total volume: 1:1, 1:2, 1:4, 1:6, 1:8, and 1:10. Prior to use these samples were stored at 4°C in sealed borosilicate glass tubes (Fisher Scientific Inc.) For the optical experiments, each glass tube was micro-centrifuged and 7- μ l aliquotes (eight from each glass tube) were placed on glass slides (VWR International Inc.). The slides were then sealed using clear nail enamel (N.Y.C.) to reduce evaporation effects. Each glass slide was then incubated at various temperatures (31, 34, 40, 52, 60, 68, 72, or 80 °C) and removed for observations hourly for five hours. Observations were performed using phase contrast microscopy technique (Olympus, IX70) at room temperature. Images were obtained with a camera (QImaging Retiga 2000R) and further processed with QCapture Pro6.0 software. For $t = 0$, observations were made immediately after the sample preparation. This procedure for direct visual observations mimics conditions of the thermodynamic measurements described below.

5.2.2 Calorimetry

Calorimetry temperature scans were performed on a home-built modulation (AC) calorimeter [38, 39] and on a model Q100 TA Instruments DSC [40]. In the modulation calorimeter, the temperature amplitude T_{ac} and the phase shift φ between the applied sinusoidal heating power $P(t) = P_0 \exp(i\omega t)$ and the resulting temperature oscillations yield a direct measure of the heat capacity as $C^* = P_0/(\omega T_{ac})$ [41, 42].

Temperature scans were performed at a rate of 0.017 to 1°C/min with the initial heating followed immediately by a cooling scan at the same rate. The modulation frequency used throughout was $f = 30$ mHz ($\omega = 2\pi f = 0.1885$ rad/sec). These components yield information about the static and dynamic character of C but only reveal qualitative insight into the enthalpy. In particular, for small values of the phase shift and a single homogeneous state of the sample, φ should be inversely proportional to C (at fixed below the internal thermal relaxation rate) as $\tan \varphi \sim 1/R_e C$ where R_e is the external thermal resistance [39, 43]. Deviations from this behavior unambiguously indicate the presence (but not magnitude) of dispersion such as latent heat or sample rearrangement [44]. In the DSC experiments, direct measurements of the sample enthalpy (heat flow) were performed on heating at 1°C/min [45]. The recorded time (t), temperature (T), and heat flow (dH/dt) can be used to extract the specific heat as $C_p = [(dH/dt)/(dT/dt)]/m$, where m is the mass of the sample. The excess specific heat due to changes from the baseline of the sample is defined as $\Delta C_p = C_p - C_{base}$ [46, 47].

Both DSC and modulation calorimetric techniques employed hermetic DSC pans designed for volatile liquids, aqueous solutions above 100°C, and other special applications [40]. Nevertheless, these pans did not prevent water evaporation, a particularly difficult problem for the modulation technique that required long measurement times at elevated temperatures. Therefore, specially re-enforced pans were designed for use with AC-calorimeters (AC-cells). Sealed with super glue, this custom made pan allowed for a hermetic encapsulation of an aqueous sample up to $\sim 74^\circ\text{C}$ at which temperature the pan abruptly ruptured.

The prepared stock and diluted samples were stored at 4°C until used. The CDLC sample was shaken vigorously to obtain a uniform structure distribution within the sample bulk before being sealed into the DSC pans or AC-cells. All pans were thoroughly cleaned before the sample was introduced. Sample mass ranged from ~ 10 mg for the DSC pans up to 40 – 60 mg for the AC-cells.

5.3 RESULTS

5.3.1 Optical microscopy

Optical observations of the intermediate metastable structures formed in CDLC reveal two distinct phenomena corresponding to the evolution of a single structure and two collective phenomena representing temporal evolution of a large number of structures. Single structure phenomena include: (1) growth of a single straight or curved structure (thickening as well as lateral and axial elongation) and (2) straightening of a single curved structure. Collective phenomena are represented by: (1) alignment and (2) clustering of straight and curved structures. Figure 5.2 illustrates typical observations of diluted (stock:water at 1:10 in columns A1 and A2) and stock CDLC (stock:water at 1:1 in columns B1 and B2) as a function of temperature. At low concentrations and low temperatures, e.g., 30°C (column A1), the individual intermediate metastables undergo straightening and elongation followed by a cooperative alignment. In comparison, low concentrations and high temperatures, e.g., 60°C, (column A2), result in similar straightening transitions, however structures's growth is represented by their thickening

rather than elongation; these two processes are then followed by a cooperative alignment, similar to that occurring at low temperatures. To contrast, the main characteristic of concentrated CDLC is clustering of metastables early in their temporal evolution at all temperatures. As an example, columns B1 and B2 of **Figure 5.2** illustrate evolution of stock CDLC at 31°C and 60°C, respectively. At this concentration, metastable's progression at the lower temperature is represented by structures straightening and elongating. At higher temperatures, however, in addition to straightening the structures thicken rather than elongate.

Generally, alignment is found to be characteristic of samples at low concentrations, while clustering occurs in concentrated samples. However, rates and extent to which these phenomena occur seem to be temperature-dependent. Additionally, structure straightening and growth at all concentrations appear to be temperature-dependent phenomena. The highest degree of straightening is found to occur at higher temperatures. This is expected since such structural reorganization is likely to require relatively higher energies and the need for faster kinetics. Notably, growth at higher temperatures is represented mainly by structures thickening, as visualized by the darkest shades, to produce thick but short precursors to ChM crystals. At lower temperatures, on the other hand, structure growth mostly occurs via elongation producing extended but thinner metastables that also lead to the final state of ChM. Notwithstanding the initial conditions, the most stable temperatures is represented mainly by structures thickening, as visualized by the darkest shades, to produce thick but short precursors to ChM crystals.

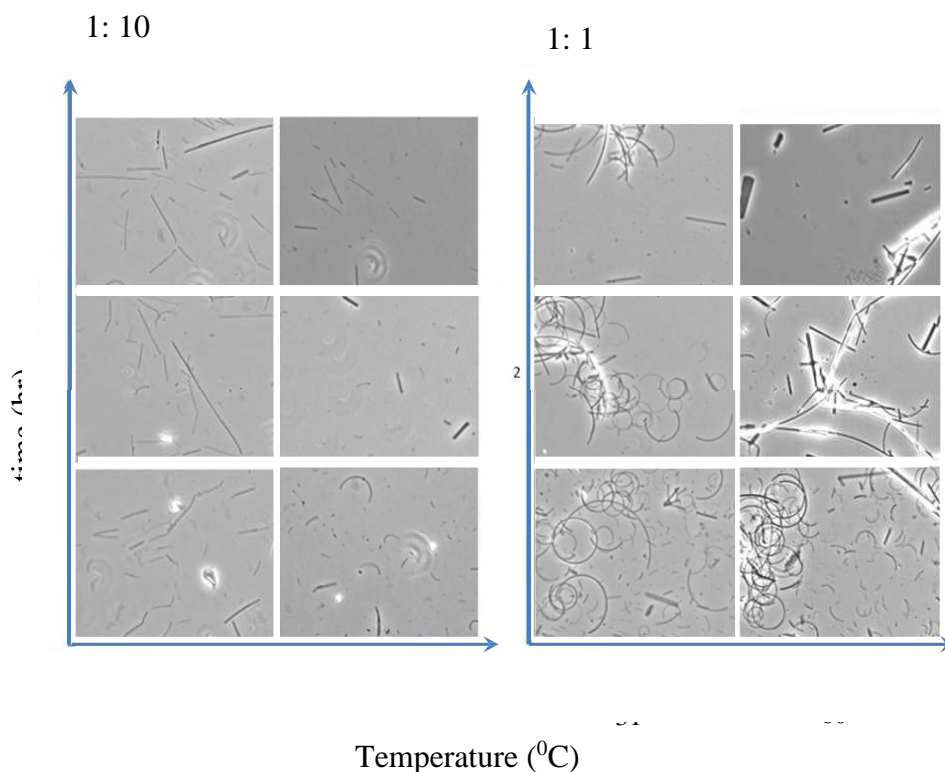


Figure 5.2. Temporal evolution of structures as a function of temperature and concentration. Left panel shows phase-contrast micrographs of microstructures at 1:10 CDLC concentration (stock:additional water) at 31 °C (column A1) and 60 °C (column A2). Right panel shows phase contrast micro-graphs of microstructures at 1:1 CDLC concentration at 31°C (column B1) and 60°C (column B2). Each micrograph width represents 14 μm . For the 1:10 sample at 31°C (low temperature, low concentration, A1), the coexisting structures generally exhibit straightening, elongation, and alignment over time. For the 1:1 sample at 31°C (low temperature, high concentration, B1), the structures progress through straightening, elongation, and clustering. For the 1:10 sample at 60°C (high temperature, low concentration, A2), the structures exhibit straightening, thickening, and alignment. For the 1:1 sample at 60°C (high temperature, high concentration, B2), the structures progress through straightening, thickening, and clustering.

5.3.2 Calorimetry

Figure 5.3 illustrates the heat capacity, C , on the top panel and phase shift, φ , on the bottom panel for heating and cooling measured with the AC-technique on a 1:1 CDLC sample. These scans were performed at a rate of ± 0.017 °C/min from 26 to 84 °C. As with most samples studied, both the DSC and AC cells suffered from water evaporation (leaking). The sample mass loss on heating is represented on **Figure 5.3** by a negative sloping background (open circles). The subsequent cooling scan (solid circles), however, demonstrates gradual saturation as all the water escapes from the sample cell. On heating, a step up feature in C with the complimentary step down feature in φ is observed at ~ 33 °C. Between 33 and ~ 64 °C, both C and φ evolve as the inverse of each other with indications of ‘dips’ characteristic of sample rearrangement within the cell. Interestingly, between 64 and ~ 77 °C, a series of step down features in both C and φ are observed. The violation of the inverse behavior between C and φ strongly indicates the presence of dispersion mechanisms such as latent heat over this ~ 13 °C range. In the upper region of temperatures studied, i.e., between 77 to 84°C,

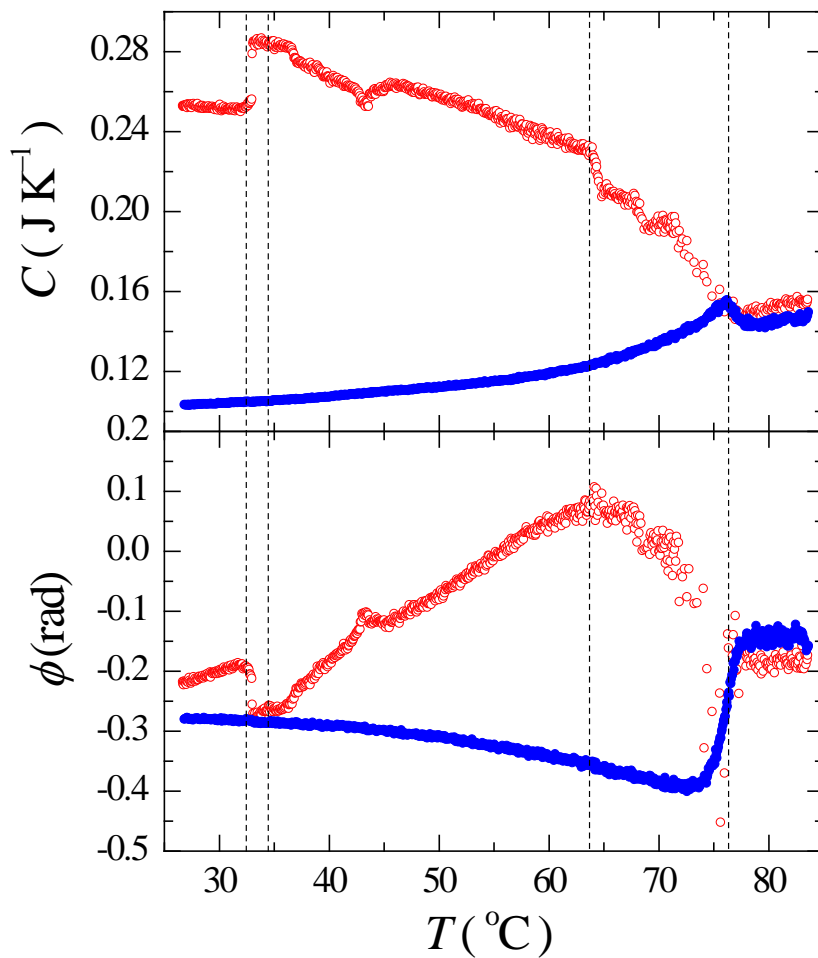


Figure 5.3. Heat capacity and phase by modulation calorimetry. Wide-temperature scans at $\pm 0.01^\circ\text{C}/\text{min}$ of the heat capacity amplitude C (top panel) and phase shift ϕ (bottom panel) on heating (open circles) and cooling (solid circles) of a fresh 1:1 concentration CDLC sample. Note that the decreasing baseline in the top panel reflects the slow evaporation of water from the cell.

the heat capacity on heating essentially overlays the one on cooling. Notably, upon returning to about 77°C, a peak in C coincident with a large shift in φ is observed, a feature consistent with a first-order transition. Below 77°C on cooling, both C and φ vary smoothly and as expected reveal no features potentially due to the entire bulk of CDLC being crystallized. Such smooth variation of the heat capacity upon cooling is in stark contrast with the preceding heating run that reveals multiple features indicating the nonreversible nature of any transformations. Overall, the hysteresis in heat capacity between heating and cooling is consistent with the slow evaporation of water on heating with ensuing increase in CDLC concentration.

To reduce the problem of water evaporation AC-cells were employed. **Figure 5.4** displays a heating scan of a stock solution of CDLC (1:1) performed with such a cell. Some features observed for both C (open circles) and φ (solid circles) on this scan appear to be consistent with those displayed in **Figure 5.3**, e.g., the single step feature at $\sim 33^\circ\text{C}$ and a series of step features with an increasing baseline above $\sim 53^\circ\text{C}$ until cell rupture. On the other hand, the behavior of φ relative to C in this temperature range does not follow the expected inverse relationship indicating a significant release of excess heat.

The excess specific heat release was probed through a series of DSC measurements. **Figure 5.5** illustrates the extracted excess specific heat, ΔC_p , for a heating scan of 1:1 CDLC sample at $+1^\circ\text{C}/\text{min}$, a scan rate that is about two orders of magnitude faster than the one in the modulation technique. A sequence of ΔC_p peaks in this figure is consistent with the features observed in modulation calorimetry scans. However, the step-up feature at $\sim 33^\circ\text{C}$ observed in both **Figure 5.3** and **Figure 5.4** is now shifted upward to $\sim 43^\circ\text{C}$.

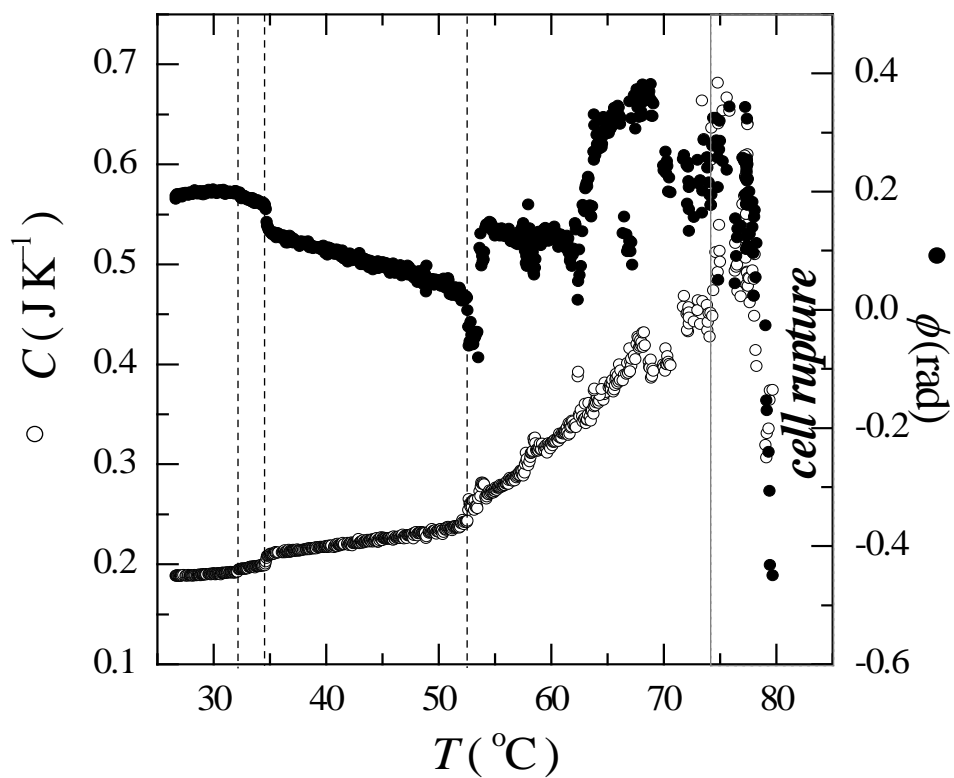


Figure 5.4. Heat capacity by modulation calorimetry. The heat capacity C (open circles) and phase shift ϕ (solid circles) of a hermetically sealed cell containing a 1:1 concentration CDLC sample on heating at $+0.017^{\circ}\text{C}/\text{min}$. The cell catastrophically ruptures at about 74°C .

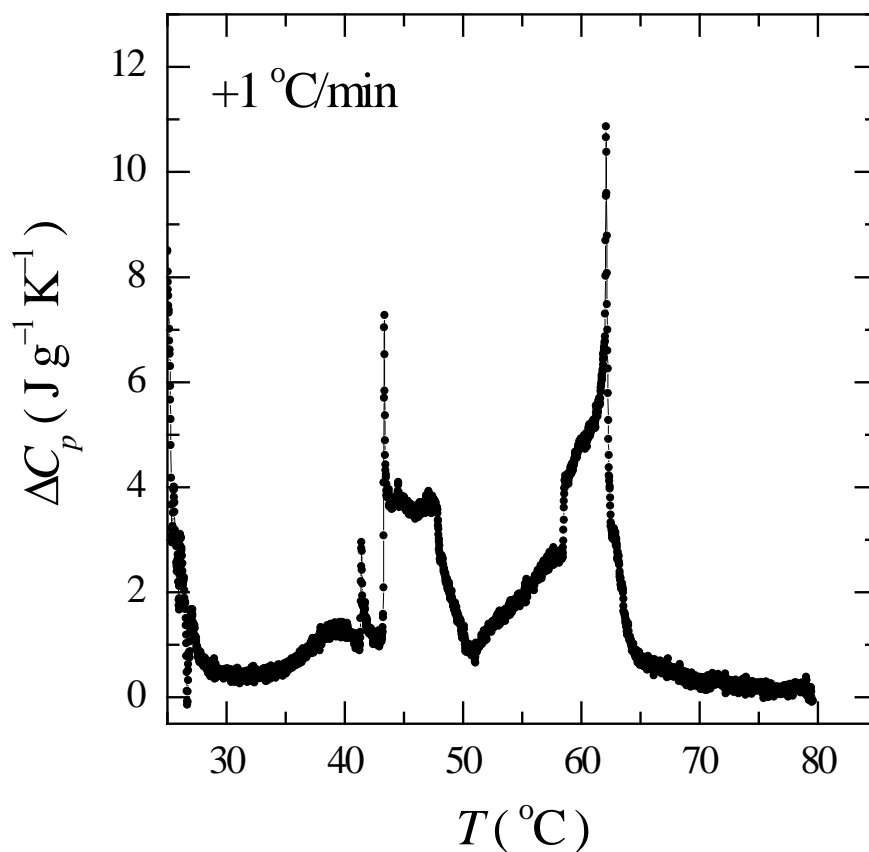


Figure 5.5. *Excess specific heat by DSC. Extracted excess specific heat ΔC_p on heating at $+1^{\circ}\text{C}/\text{min}$ scan rate of a 1:1 concentration CDLC sample. The initial rapid decrease of ΔC_p from 23 to $\sim 28^{\circ}\text{C}$ is due to the typical transient at the start of the DSC heating scan.*

Similarly to the modulation calorimetry scan performed with AC-cells **Figure 5.4**, the step-down features at higher temperatures in **Figure 5.5** initiate at $\sim 57^\circ\text{C}$. This, however, is $\sim 5^\circ\text{C}$ lower in temperature than the feature in **Figure 5.3** for the evaporating cell. These features represent a series of temperature dependent first-order transformations and sample rearrangements. On further heating and ensuing melting of all metastables, CDLC is converted into an isotropic melt. Sample cooling from this isotropic melt reveals only a single transition feature typical of concentrated cholesterol crystallization [28, 29].

5.4 Discussion and Conclusions

The results of the optical and calorimetric studies present a wide range of observations as a function of temperature and time. Generally, these results support the view that all microstructures in CDLC are long-lived intermediate metastables enroute towards final cholesterol monohydrate (ChM) crystals. The kinetics of the intermediate microstructures transformations is essentially frozen well below $\sim 30^\circ\text{C}$ and becomes progressively faster with increasing temperature. The fastest kinetics and evolution of the microstructures towards ChM appears to exist just below the ChM melting temperature at $\sim 70^\circ\text{C}$, thus suggesting that crystallization occurs on heating. In reality, all intermediate self-assembled microstructures coexist in a broad metastability region.

The evolution rate of the various microstructures is driven by temperature and molecular concentration within the solvent medium. The optical

studies revealed a reproducible pattern of structural evolution. As an example, a series of structures at low and high temperatures with low and high transformation kinetic rates, respectively, are shown in **Figure 5.6**. The following classification is introduced in this work; individual microstructures (inter-structures) evolve through *Straightening* of curved filaments and growth by *Elongation* or lateral/axial *Thickening* of filaments. Collectively, groups of microstructures (intra- structures) evolve through *Alignment* and *Clustering*.

For inter-structural evolution, *Straightening* is observed for the curved filaments at all temperatures and concentrations but is most pronounced at higher temperatures near but below ChM melting. Here, straightening of **individual** structures would follow a direct path towards ChM and is consistent with this process being the most energetically intense. Growth by *Elongation* occurs at lower temperatures while growth by lateral or axial *Thickening* occurs at higher temperatures roughly independent of CDLC concentration. These observations are consistent with internal structural evolution through elongation and thickening requiring higher energies, faster kinetics, and that the formation of these structures is endothermic.

For intra-structural evolution or cooperative behavior, *Alignment* of mostly straight structures occur primarily at low CDLC concentration while *Clustering* of straight and curved structures is found at high CDLC concentration. Both collective phenomena appear independent of temperature, which, given the micron sizes of the structures involved, suggests that these effects are not thermally activated. The *Alignment* behavior at low concentrations is understandable since here the microstructures have sufficient free-volume and time to reorient and align, presumably through steric interactions.

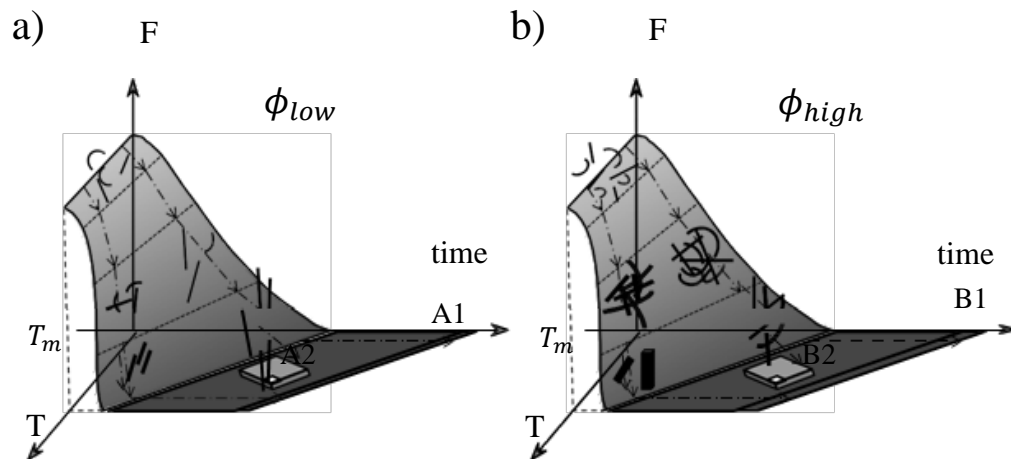


Figure 5.6. *Microstructure evolution. Cartoon depicting the temporal evolution of microstructures through a free-energy landscape towards full crystallization into cholesterol monohydrate (ChM). The free-energy gradient, which is proportional to the rate of evolution kinetics, increases with increasing temperature. Generally, for a) low CDLC concentration, the structures progress from straightening to elongation or thickening to alignment. For b) high CDLC concentration, the structures progress from straightening to elongation or thickening to clustering. The points A1, A2 in a) and B1, B2 in b) correspond to the panels in Fig. 2. The temperature T_m refers to the melting temperature of ChM.*

This interaction among the microstructures would greatly improve the efficiency of finding the proper boundary matching in order to merge.

The *Clustering* behavior at higher CDLC concentrations is understandable as the relatively short distances, thus restricted free-volume, between structures prevent sufficient alignment. Such random clustering of

structures would prevent proper matching of individual boundaries in order for merging or growth to proceed. In essence, clustering at high concentrations causes a proliferation of defects and suggests the importance of the infrastructural distance in determining the path towards ChM. These two observed collective phenomena, following any local concentration fluctuations, would explain the wide variability in sample preparation.

The direct optical in situ observations of the temperature and concentration-dependent evolution of microstructures in CDLC samples approximately match the conditions of the calorimetric studies. Because the two calorimetric techniques employed used vastly different scan rates, the observed thermal signatures could be assigned as fast or slow kinetics. Collectively, thermodynamic and optical data allow a construction of a pseudo-phase diagram for the evolution of microstructures in CDLC, despite the ever-present difficulty of water evaporation from the sample. Recalling that both temperature and concentration drive the rate of kinetics, a kinetics versus concentration diagram is shown in **Figure 5.7**. The main features of this proposed pseudo-phase diagram are the two solid curves representing the high-temperature boundary with the melting of ChM into an isotropic melt and the low-temperature boundary where the CDLC microstructures evolve at such a slow rate that they can be considered "frozen", and since these are metastable structures, this region has many features in common with glasses.

These two solid lines should approach zero rate of kinetics as the CDLC stock concentration approaches zero as the evolution of the microstructures depends strongly on interactions among the structures. The dashed lines between the two solid essentially divide this region into rough quadrants denot-

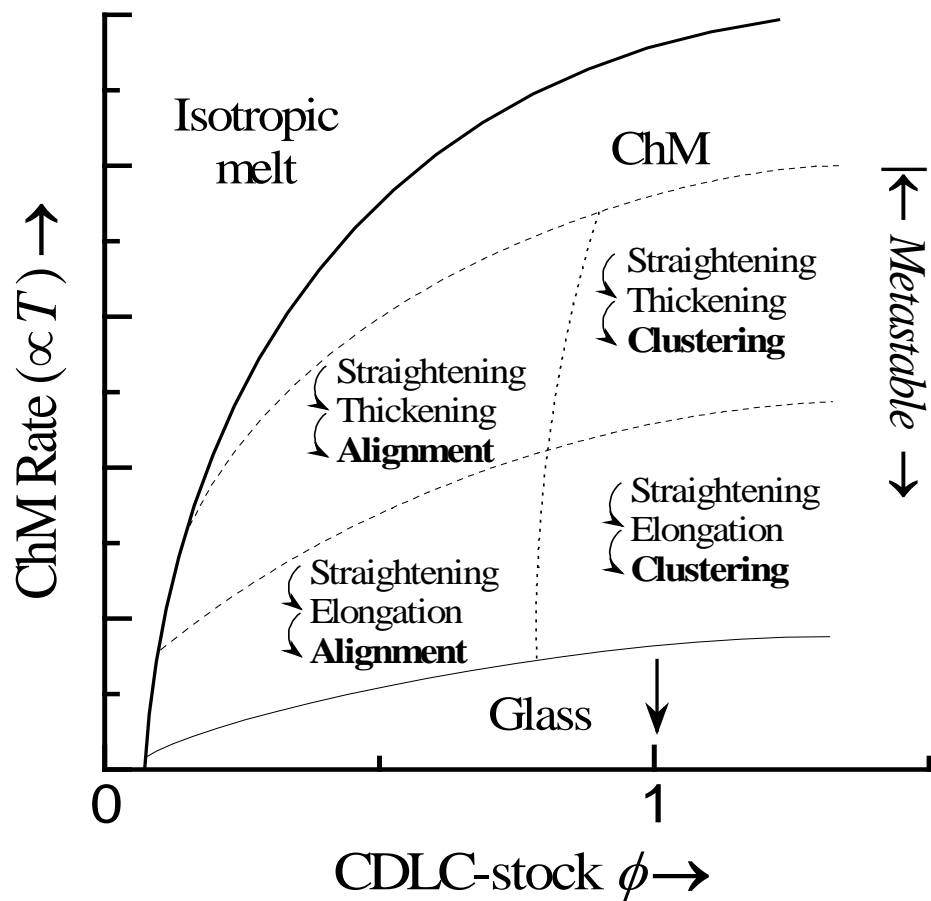


Figure 5.7. Temperature-concentration pseudo-phase diagram for CDLC. Proposed phase diagram for the CDLC system combining the optically observed structures with the temperature of features observed by calorimetry.

ting the evolution characteristics of all coexisting microstructures. This construction represents a new way of visualizing the complex evolution of these unique self-assemblies. While the proposed pseudo-phase diagram is consistent with the range of observations, both optically and calorimetrically, there remain many open questions requiring both theoretical and experimental efforts. Given the recent x-ray result that one particular microstructure in CDLC is actually crystalline (though with a unique super structure) [5], it is tempting to regard all self-assembled microstructures as essentially crystalline in nature but due to the frustration of the initial assemblies (proliferation of defects), there exists significant energy barriers enrooted to the final ChM phase. Theoretical work along these lines would be very useful. Experimentally, the question of how to directly probe the activated kinetics of these structural evolutions remains open. Clearly, what is needed are tags, such as quantum dots, with which to mark a specific microstructure and follow the dynamics of the tag at various concentrations and temperatures. The dynamics of the tag should be related to the structure to which it is attached and so the activation energy might be probed.

5.5 References

- [1] Y. V. Zastavker, N. Asherie, A. Lomakin, J. Pande, J. M. Donovan, J. M. Schnur, and G. B. Benedek, *Proc. Natl. Acad. Sci. USA*, **96**, 7883 (1999).
- [2] F. M. Konikoff, D. S. Chung, J. M. Donovan, D. M. Small, and M. C. Carey, *J. Clin. Invest.*, **90**, 1155 (1992).
- [3] F. M. Konikoff, D. E. Cohen, and M. C. Carey, *Mol. Cryst. Liq. Cryst.*, **248**, 291 (1994).
- [4] D. Wang and M. Carey, *J. Lipid Res.*, **37**, 606 (1996).
- [5] B. Khaykovich, C. Hossain, J. J. McManus, A. Lomakin, D. E. Moncton, and G. B. Benedek, *Proc. Natl. Acad. Sci. USA*, **104**, 9656 (2007).
- [6] J. M. Schnur, *Science*, **262**, 1669 (1993).
- [7] J. V. Selinger and J. M. Schnur, *Phys. Rev. Lett.*, **71**, 4091 (1993).
- [8] P. Yager and P. E. Schoen, *Mol. Cryst. Liq. Cryst.*, **106**, 371 (1984).
- [9] N. Nakashima, S. Asakuma, and T. Kunitake, *J. Am. Chem. Soc.*, **107**, 509 (1985).
- [10] J. H. Georger, A. Singh, R. R. Price, J. M. Schnur, P. Yager, and P. E. Schoen, *J. Am. Chem. Soc.*, **109**, 6169 (1987).
- [11] J. H. Fuhrhop, P. Schnieder, E. Boekema, and W. Helfrich, *J. Am. Chem. Soc.*, **110**, 2861 (1988).
- [12] R. M. Servuss, *Chem. Phys. Lipids*, **46**, 37 (1988).
- [13] B. N. Thomas, R. C. Corcoran, C. L. Cotant, C. M. Lindemann, J. E. Kirsch, and P. J. Persichini, *J. Am. Chem. Soc.* **120**, 12178 (1998).
- [14] B. N. Thomas, C. M. Lindemann, and N. A. Clark, *Phys. Rev. E*, **59**, 3040 (1999).

- [15] D. S. Chung, G. B. Benedek, F. M. Konikoff, and J. M. Donovan, *Proc. Natl. Acad. Sci. USA*, **90**, 11341 (1993).
- [16] J. V. Selinger, E. C. MacKintosh, and J. M. Schnur, *Phys. Rev. E*, **53**, 3804 (1996).
- [17] Y. V. Zastavker, Ph.D. thesis, *Massachusetts Institute of Technology*, (2001).
- [18] B. Smith, Y. V. Zastavker, and G. B. Benedek, *Phys. Rev. Lett.*, **87**, 278 (2001).
- [19] W. Helfrich, *Z. Naturforsch C*, **28**, 693 (1973).
- [20] P. G. de Gennes, *C.R. Acad. Sci. Paris*, **304**, 259 (1987).
- [21] T. C. Lubensky and J. Prost, *J. Phys. II France*, **2**, 371 (1992).
- [22] C. M. Chen, *Phys. Rev. E*, **59**, 6192 (1999).
- [23] W. Helfrich, *J. Chem. Phys.*, **85**, 1085 (1986).
- [24] W. Helfrich and J. Prost, *Phys. Rev. A*, **38**, 3065 (1988).
- [25] Z. C. Ouyang and J. X. Liu, *Phys. Rev. Lett.*, **65**, 1679 (1990).
- [26] J. V. Selinger, M. S. Spector, and J. M. Schnur, *J. Phys. Chem. B*, **105**, 7157 (2001).
- [27] D. Weihs, J. Schmidt, I. Goldiner, D. Danino, M. Rubin, Y. Talmon, and F. M. Konikoff, *J. Lipid Res.*, **46**, 942 (2005).
- [28] S. Mabrey, P. I. Mateo, and J. M. Sturtevant, *Biochem.*, **17**, 2464 (1978).
- [29] C. R. Loomis, G. G. Shipley, and D. M. Small, *J. Lipid Res.*, **20**, 525 (1979).
- [30] J. Kaloustian, A.-M. Pauli, P. L. de la Porte, H. Lafont, and H. Portugal, *J. Thermal Anal. Calor.*, **71**, 341 (2003).

- [31] J. Kaloustian, P. L. D. L. Porte, T. El-Moselhy, H. Lafont, and H. Portugal, *J Thermal Anal. Calor.*, **82**, 331 (2005).
- [32] A. S. Goldstein, A. N. Lukyanov, P. A. Carlson, P. Yager, and M. H. Gelb, *Chem. Phys. Lipids*, **88**, 2136 (1997), calorimetry hard to do - leaking.
- [33] S. Svenson and P. B. Messersmith, *Langmuir*, **15**, 4464 (1999), small dsc signal of lipid nanotubes melting.
- [34] H. Nagano, H. Yao, and K. Ema, *Phys. Rev. E* **51**, 3363 (1995).
- [35] G. Nounesis, B. R. Ratna, S. Shin, R. S. Flugel, S. N. Sprunt, A. Sing, J. D. Litster, R. Shashidhar, and S. Kumar, *Phys. Rev. Lett.* **76**, 3650 (1996).
- [36] K. Uchida, H. Yao, and K. Ema, *Phys. Rev. E*, **56**, 661 (1997).
- [37] M. S. Spector, J. V. Selinger, and J. M. Schnur, *J. Am. Chem. Soc.*, **119**, 8533 (1997).
- [38] D. Sharma, J. C. MacDonald, and G. S. Iannacchione, *J. Phys. Chem. B*, **110**, 16679 (2006).
- [39] H. Yao and C. W. Garland, *Rev. Sci. Instrum.*, **69**, 172 (1998).
- [40] TA Instruments, Inc. (2009), cells.
- [41] P. F. Sullivan and G. Seidel, *Phys. Rev.*, **173**, 679 (1968).
- [42] L. M. Steele, G. S. Iannacchione, and D. Finotello, *Rev. Mex. de Fisica*, **39**, 588 (1993).
- [43] G. S. Iannacchione, C. W. Garland, J. T. Mang, and T. P. Rieker, *Phys. Rev. E*, **58**, 5966 (1998).
- [44] D. Sharma and G. S. Iannacchione, *J. Chem. Phys.*, **126**, 094503 (2007).
- [45] F. Roussel, *J. Therm. Anal.*, **47**, 715 (1996).
- [46] D. Sharma, R. Shukla, A. Singh, A. Nagpal, and A. Kumar, *Adv. Mater. Opt. Electron.*, **10**, 251 (2000).

[47] D. Sharma, S. K. Dwivedi, R. K. Shukla, and A. Kumar, *Mater. Manuf. Processes*, **18**, 93 (2003).

CHAPTER 6

CONCLUSIONS

This work studies the transition and mesophases of biomolecules (short DNA fragments, proteins and cholesterol structures) found in aqueous solutions. All the experimental data have shown the molecular structural and organizational changes under the effect of the physical factors as temperature, sample concentration, time, and electric field frequency. We believe that we have given some contribution to highlight the existing models about self-assembling/self-orientation of macromolecules.

In the DNA+buffer (pH=8.0), our results have shown a full analyses of the dynamics and kinetics involved on self-organizing of DNA. High resolution AC-calorimetry used is able to detect intermediate states, predicted to be short lived and also unobservable at the temporal resolution (DSC). Ex-

cept predicting the melting temperature T_m , a very important physical feature, we were also able to observe other structural and organizational changes. Multiple experimental runs were used to observe any reproducibility of the clustering or any other associations. Mainly, all the mesophases belong to the temperatures lower than T_m and this is consistent with literature as well. Another powerful experimental method is the dielectric spectroscopy. It is known that a low frequency regime (0.1-100 kHz) can be used to probe the large-scale molecular motion and structural aggregation. We believe that the frequency modes detected for high DNA concentration, are present because of the induced dipoles within the multiple DNA structural self-oriented layers. All this project work is concluded on a phase diagram that helps to have a better view for the DNA structural organization/ packing under certain physical conditions. Knowledge gained could help researchers better understand the function of proteins, and identify new targets for drug development.

Further experimental work, continued on other interesting biomolecular systems, has supported that the driving force for molecular denaturation is the increase in entropy of the system. The protein thermal transition and denaturing can be probed by controlling different physical parameters. One of them is the temperature-heating rate, which is responsible for controlling kinetically the protein transitions. This effect is more evident on observing the transition peak. The Lysozyme + PBS thermal profiles reveal a single feature at $\sim 72^\circ\text{C}$ for $\varphi_w < 0.32$, but two features for $\varphi_w = 0.32$ at 66°C and 84°C , all “reversible”. This lower -T process may be related to protein unfolding, leading to large structures while the higher-T feature not independent monomers (perhaps random associations of α helices and

β sheets). Dielectric spectroscopy has been used as well. The low frequency dynamics of the Lysozyme + PBS, likely involving the reorientation or redistribution of the bound water and the protein, are different from that in powder lysozyme and are due to the aqueous environment (swelling and self-assembly is still an open question).

An important part of all this work is related to the intermediate phases and evolution of cholesterol structures found in CDLC. The results of the optical and calorimetric studies present a wide range of observations as a function of temperature and time. The evolution rate of the various microstructures is driven by temperature and molecular concentration within the solvent medium. For inter-structural evolution, Straightening is observed for the curved filaments at all temperatures and concentrations, but is most pronounced at higher temperatures near but below ChM melting. Growth by Elongation occurs at lower temperatures while growth by lateral or axial Thickening occurs at higher temperatures roughly independent of CDLC concentration. These observations are consistent with internal structural evolution through elongation and thickening requiring higher energies, faster kinetics. When it comes to the cooperative behavior, there is some Alignment of straight structures at low concentrations while high concentration favors Clustering of them.

Collectively, thermodynamic, spectroscopic and optical data allow often a construction of a phase diagram for the evolution of macromolecules in aqueous solutions, despite the ever-present difficulty of water evaporation from the sample. Theoretical work along these lines would be very useful.

APPENDIX

PUBLICATIONS

1. *Y. A. Miroshnikova, K. Kashuri, M. Elsenbeck, Guanqing Ou,* and Y. V. Zastavker , and G. S. Iannacchione; “Phase Diagram of Microstructures in Chemically-Defined Lipid Concentrates by Optical Microscopy and High-resolution Calorimetry.”submitted to Physical Review E

2. *K. Kashuri, H. Kashuri, and G.S. Iannachione* ;“Understanding Lysozyme Conformation in Aqueous Solutions by thermal studies of Low-Frequency Dielectric Spectra and Calorimetry.” to be submitted.

3. *K. Kashuri, H. Kashuri, and G.S. Iannachione* ; “ LC-Phase Ordering of Short DNA Fragments In Aqueous Solution.” to be submitted.

CONFERENCES /ABSTRACT PUBLISHED

1. *H. Kashuri, K. Kashuri, and G.S. Iannacchione*, 2012, APS March Meeting (Boston, MA); “Heat Capacity Measurements by Simultaneous Relaxation and AC-Calorimetry.”
2. *K. Kashuri, H. Kashuri, and G.S. Iannacchione*, 2012, APS March Meeting (Boston, MA); “Calorimetric and Low-Frequency Dielectric Studies of Mesoscopic Ordering in Solutions of Engineered DNA Hairpin Fragments.”
3. *K. Kashuri, H. Kashuri, and G.S. Iannacchione*, 2011, APS March Meeting (Dallas, TX) ; ”The Effect of Phosphate Buffered Saline (1xPBS) on Induced Thermal Unfolding and Low Frequency Dielectric Spectra of Lysozyme”. Bull. Am. Phys. Soc. 56 (2), P39.00004.
4. *H. Kashuri, K. Sigdel, K. Kashuri, and G.S. Iannacchione*, 2011, APS March Meeting (Dallas, TX) ; “Measuring the imaginary part of the permittivity using calorimetry”, Bull. Am. Phys. Soc. 56 (2), W21.00014.
5. *Y.A.Miroshnikova, M. Elsenbeck, Guanqing Ou, Y.V. Zastavker, K. Kashuri, and G.S. Iannacchione*, 2009, APS March Meeting (Pittsburgh, Pennsylvania) ; “ Pseudo-phase Diagram of Cholesterol-rich Filamentous, Helical Ribbons and Crystal Microstructures”, Bull. Am. Phys. Soc. 54 (1), H39.00010.

6. *Y. A. Miroshnikova, M. Elsenbeck, **K Kashuri**, G. S. Iannacchione, and Y. V. Zastavker*, 2008, 3rd IUPAP International Conference on Women in Physics, Seoul, Korea, “Optical and calorimetric studies of cholesterol-rich filamentous, helical ribbon, and crystal microstructures”, ICWIP2008.

7. ***K. Kashuri**, G. S. Iannacchione, Y. A. Miroshnikova, and Y. V. Zastavker*, 2008, APS March Meeting (New Orleans, LA) ; “Calorimetric and Optical Studies of Cholesterol-Rich Filamentous, Helical Ribbons and Crystal microstructures”, Bull. Am. Phys. Soc. 53 (2), B17.00014.